Influences of Seaways, Atmospheric CO_2 and Greenland Ice Sheet on the Pliocene Climate in the Kiel Climate Model

Dissertation
in fulfillment of the requirements for the degree "Dr. rer.nat"
of the Falculty of Mathematics and Natural Sciences at
Kiel University

Zhaoyang Song

Sep. 2017

Maritime Meteorology
GEOMAR Helmholtz Centre for Ocean Research Kiel

First Referee: Prof. Dr. Mojib Latif
Second Referee: Prof. Dr. Dirk Nürnberg

Date of Examination: November 23, 2017
Approved for Publication: November 23, 2017

Contents

Zusammenfassung

Diese Doktorarbeit behandelt den Einfluss von Veränderungen in der atmosphärischen CO_2 Konzentration, der ozeanischen Passagen und des Grönlandeisschildes (GrES) auf das Klima des Pliozäns (5,3-2,6 Mio. Jahre vor unserer Zeit). Es werden drei Reihen von Sensitivitätsexperimenten mit einem gekoppelten Klimamodell analysiert und mit verschiedenen Paleoklimarekonstruktionen des Pliozäns verglichen. In der ersten Experimentenreihe wird die Sensitivität der Meeresoberflächentemperatur (SST) und des Ostasiatischen Sommermonsun (OASM) auf Änderungen in der CO_2 Konzentration und der Passagen im Klimamodell untersucht, während in der zweiten Experimentenreihe das El Niño/Southern Oscillation (ENSO) Phänomen und der mittlere Zustand und Jahresgang im tropischen Pazifik analysiert wird. In einer dritten Experimentenreihe wird der Einfluss von Änderungen im GrES auf die atlantische meridionale Umwälzzirkulation (AMOC) bei Änderungen in der Obliquität der Erdachse untersucht.

In der ersten Experimentenreihe wird der Einfluss des Rückganges in der CO_2 Konzentration, die Verengung der Indonesischen Passage und die Schließung der Panama Passage auf das globale Klima und den OASM in vier Sensitivitätsexperimenten untersucht. Der Einfluss der CO_2 Konzentration auf die SST im Klimamodell stimmt mit den Proxydaten gut überein. Dies ist ein Hinweis darauf, dass die Vereisung der Nordhemisphäre im Pliozän durch den Rückgang der CO_2 Konzentration verursacht wurde. Ein Vergleich mit ozeanischen Proxydaten zeigt, dass das Klimamodell die SST Veränderungen im südlichen Ozean und in den Tropen gut reproduzieren kann, aber im Nordatlantik und in der Arktis deutlich unterschätzt. Der Einfluss der Passagenänderungen auf das globale Klima ist klein. Er ist hauptsächlich auf die Tropen beschränkt, da die Veränderungen der Passagen die AMOC nur sehr wenig verändern. Daher kann keine der beiden Passagenänderungen die Abweichungen zwischen Modelldaten und Proxydaten in den höheren Breiten der Nordhemisphäre erklären. Der Einfluss der abnehmenden CO_2 Konzentration auf den OASM ist markanter. Es wird eine signifikante Verstärkung des OASM bei einem Rückgang der CO_2 Konzentration simuliert. Dies wird hauptsächlich durch einen verstärkten Land-See-Kontrast verursacht, während der Niederschlag über der Monsunregion etwas zurückgeht. Der reduzierte Wasserdampfgehalt aufgrund des CO_2 Rückganges trägt signifikant zur Niederschlagsänderung bei. Im Gegensatz dazu schwächen die beiden Änderungen in den Passagen den OASM nur geringfügig und haben kaum Auswirkungen auf den Niederschlag.

Im der zweiten Experimentenreihe wird in acht Sensitivitätsexperimenten der Einfluss der Änderungen in den Passagen und im CO_2 auf das mittlere Klima, den Jahresgang im tropischen Pazifik und ENSO untersucht. Dabei ist der Fokus auf den Auswirkungen der Schließung der Panama Passage und die Verengung der Indonesischen Passage. Es wird gezeigt, dass eine Schließung der Panama Passage die Amplitude von ENSO reduziert, während eine Verengung der Indonesischen Passage die Variabilität von ENSO leicht erhöht. In allen Experimenten

bleibt die Schwingungsdauer von ENSO unverändert. Eine Analyse mit dem Bjerknes Stabilitätsindex deutet an, dass die Stabilität von ENSO durch eine gegenseitige Kompensation von Änderungen in den positiven und den negativen Feedbacks in ENSO verursacht wird. Die Änderungen im Jahresgang fallen stärker aus. Die Schließung der Panama Passage verursacht durch die Verstärkung des meridionalen Windes eine Verstärkung des Jahresganges der SST. Im Gegensatz dazu hat eine Verengung der Indonesischen Passage nur geringe Auswirkungen auf den Jahresgang der SST. Es konnte ein Zusammenhang zwischen der ENSO Amplitude und dem Jahresgang der SST gefunden werden, da sich die Amplitude von ENSO verstärkt wenn sich der Jahresgang der SST abschwächt.

Im Übergang vom Pliozän zum Pleistozän (3,2 – 3,0 bis 2,5 Mio. Jahre vor unserer Zeit) begannen sich die Gletscher der Nordhemisphäre zu bilden und die Klimavariabilität auf Zeitskalen der Obliquität der Erde (41.000 Jahre) zu erhöhen. In einer dritten Experimentenreihe wird der Einfluss der Ausdehnung des GrES und der Änderung in der Obliquität der Erde auf das mittlere Klima untersucht. Dabei ist der Fokus auf der AMOC. In Klimamodellexperimenten konnte gezeigt werden, dass eine Zunahme des GrES den Wärmeverlust des Ozeans an die Atmosphäre im Meer um Grönland-Island-Norwegen reduziert und dadurch die AMOC leicht abschwächt. Eine durch die Zunahme des GrES verursachte Abkühlung der Extratropen verstärkt den Einfluss der Obliquitätsänderung auf die Hadley Zirkulation und die Innertropische Konvergenzzone. Dies wiederum verstärkt den Einfluss der Obliquitätsänderung auf den Export von Süßwasser aus dem tropischen Atlantik und die Veränderungen der AMOC um den Faktor 2. Die verstärkte Veränderung in der AMOC hat Auswirkungen auf die globale Mitteltemperatur. Zusammenfassend kann man sagen, dass die Auswirkungen der Obliquitätsänderung auf die AMOC ein weiteres wichtiges Puzzleteil sind, um die verstärkte Klimavariabilität während des Übergangs vom Pliozän ins Pleistozän zu erklären.

Abstract

This thesis provides an improved understanding of the impacts of changes in the atmospheric CO_2-concentration, oceanic seaways,and Greenland ice sheet (GrIS) on the Pliocene climate (5.3-2.6 million years before present; Ma B.P.). Three sets of sensitivity experiments using a coupled atmosphere–ocean–sea ice model are analyzed and assessed with multiple paleoclimate reconstructions for the Pliocene. In particular, in the first set the model sensitivity of sea surface temperature (SST) and the East Asian summer monsoon (EASM) to changes in CO_2 and oceanic seaway is investigated, while in the second set the mean state, the annual cycle in the tropical Pacific and El Niño/Southern Oscillation (ENSO) is analysed. In the third set, the impact of GrIS changes on the response of the Atlantic meridional overturning circulation (AMOC) and surface climate to obliquity forcing is examined.

More in detail, in the first set the influences of declining atmospheric CO_2-concentration, the narrowing Indonesian Passages, and the closing shallow Panama Seaway on global mean surface climate and EASM is investigated with four sensitivity experiments. The model sensitivity of global mean SST to CO_2-concentration changes agrees well with the range suggested by the proxy data, which further indicates the Northern Hemisphere glaciation is controlled by declining CO_2 in the Pliocene. A pointwise model-data comparison suggests that the model generally reproduces SST changes in the Southern Ocean and the Tropics, but substantially underestimates SST changes in the North Atlantic and Arctic region, in comparison with marine reconstructions. The impacts of seaway changes are minor with respect to global changes. Their influences are largely restricted within the Tropics, as there is only a weak modulation of seaway changes on the meridional ocean circulation. Therefore, neither of aforementioned seaway changes improves the model-data discrepancy in the northern high-latitudes. Impacts of declining CO_2 on the EASM are more prominent. A significant intensification of EASM is simulated in response to the declining CO_2, which is largely attributed to the enhanced land-ocean thermal contrast, while the precipitation over monsoon region slightly decreases. A water vapor budget analysis suggests that the reduced atmospheric moisture content due to decreasing CO_2 significantly contributes to precipitation response. In contrast, both seaway changes weaken the EASM to a lesser extent and barely drive precipitation changes.

In the second set, the influences of seaway and CO_2 changes on the tropical Pacific mean climate, annual cycle and ENSO are investigated in eight sensitivity experiments. Special attention is paid to the closing of deep Panama Seaway and the narrowing Indonesian Passages. It is found that the ENSO amplitude reduces in response to the closing of the Panama Seaway, while the narrowing of the Indonesian Passages slightly enhances ENSO variability. ENSO period is stable in all experiments. The Bjerknes stability analysis further suggests the relatively stable ENSO is attributed to the compensation of positive and negative feedbacks involved in ENSO dynamics. Annual cycle changes are more prominent. A significant intensification of the annual cycle is simulated in response to the closing of the Panama Seaway, which is

largely attributed to the strengthening of meridional wind stress. In contrast, the narrowing of the Indonesian Passages only drives relatively weak changes in the annual cycle. A robust relationship is found such that ENSO amplitude strengthens when the annual cycle amplitude weakens.

Plio-Pleistocene transition (3.2 - 3.0 to 2.5 Ma B.P.) was characterized as the onset of Northern Hemisphere glaciation and enhanced climate variability at the obliquity frequency (41 ka). In the third set, we investigate the influence of the GrIS expansion on the mean surface climate and its response to obliquity forcing. Special attention is paid to the AMOC. A set of climate model simulations suggests that the GrIS expansion reduces oceanic heat loss of the Greenland-Iceland-Norwegian Sea to the atmosphere, thereby weakening the AMOC slightly. Moreover, extratropical cooling induced by the GrIS expansion further amplifies the Hadley circulation and intertropical convergence zone (ITCZ) response to obliquity forcing, which further drives amplified obliquity-forced response of freshwater export from the tropical Atlantic, and in turn responses of the AMOC by a factor of two. The stronger AMOC response to obliquity forcing in turn results in a stronger global-mean near-surface temperature response. We conclude that the AMOC response to obliquity forcing adds one piece to the puzzle of the enhanced climate variability at the obliquity frequency during the Plio-Pleistocene transition.

Chapter 1

Introduction

Since the industrial revolution the earth is experiencing a significant warming in the averaged global temperature with remarkable regional changes. These changes have increased the emergence of worldwide environmental hazards, such as more frequent and severe extreme weather events, tropical cyclones, floods and droughts, and global mean sea level rise (*Bindoff et al.*, 2007; *Easterling et al.*, 2000; *Stocker et al.*, 2013). However, our understanding and predication for future climate and environmental changes remain highly uncertain in many aspects, as instrumental records are short and sparse. Paleoclimate reconstructions and simulations provide scientists the opportunity to extend fundamental knowledge of earth system behaviors and therefore, help to reduce uncertainties on future predictions (*Valdes*, 2011).

1.1 Pliocene climate inferred from proxy data

The Pliocene Epoch, which was from 5.3 to 2.6 Ma B.P. (million years before present), is of particular interest with respect to future climate change due to many shared characteristics of the earth system of the 20^{th} and 21^{st} century, for example, comparable atmospheric CO_2 concentration (Fig.1.1a) and a similar continental configuration (*Dowsett et al.*, 2010). For the first time, *Zubakov and Borzenkova* (1988) proposed that the Pliocene climate could be regarded as a geological reference for the warming in the mid-21st century. On the basis of ice volume and temperature proxy records, which are estimated from stable oxygen isotope, Pliocene surface temperatures were about 2-3°C warmer and the sea level was about 25 m higher with less ice sheet in the high latitudes, relative to the pre-industrial (*Dowsett and Cronin*, 1990; *Mudelsee and Raymo*, 2005; *Ravelo et al.*, 2004). The tropical Pacific warm pool was greatly expanded (Fig.1.1b, c) with largely reduced zonal sea surface temperature (SST) gradient (*Wara et al.*, 2005). Such warming signal was progressively enhanced towards the high latitudes (Fig. 1.1d), resulting in a much reduced meridional temperature gradient (*Brigham-Grette et al.*, 2013; *Dowsett and Poore*, 1991). Additionally, the monsoon system and hydrological cycle was intensified (*Zhang et al.*, 2009), vegetation cover was expanded and desert restricted (*Dupont*, 2006). Since the late Pliocene around 2.7 Ma B.P., global climate has undergone a major climate transition from a warm and relatively stable state to "icehouse" conditions, known as the Northern Hemisphere glaciation (NHG). During the NHG, the Northern Hemisphere continental ice sheet extensively developed, especially over Greenland, and to

a lesser extent over the Antarctica (*Lisiecki and Raymo*, 2005). Furthermore, ice sheets waxed and waned on a periodicity of 41 thousand-year (ka) to obliquity variation, in contrast to the 100 ka cycle since the mid-Pleistocene at ∼0.8 Ma B.P. (*Lisiecki and Raymo*, 2005).

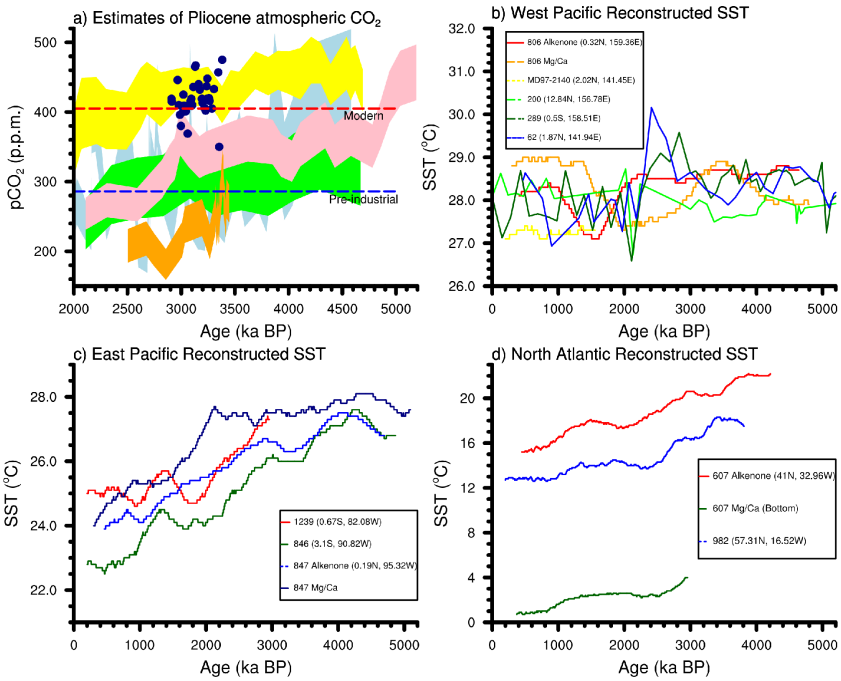

Figure 1.1: *Atmospheric CO_2 and SST reconstructions over the last 5 Ma from different proxy data, (a) Estimates of atmospheric CO_2 concentrations with pre-industrial and modern levels (horizontal lines) for comparison; green band, alkanone (Pagani et al., 2010); pink band, alkenone (Seki et al., 2010); yellow band, alkenone (Seki et al., 2010); blue band, $\delta^{11}B$ (Bartoli et al., 2011); orange band, Ba/Ca (Tripati et al., 2009); navy blue dots, $\delta^{13}C$ (Raymo and Horowitz, 1996). (b), (c) and (d) SST Trends computed as 400-ka running means of the original proxy temperature data (Fedorov et al., 2013 and references therein).*

1.2 Drivers for climate evolution

Both the horizontal and vertical displacements associated with tectonic plates and declined atmospheric CO_2 concentrations are hypothesized to have driven the long-term cooling throughout the Cenozoic era, which is the last 65 Ma B.P. (*Zachos et al.*, 2001). Tectonic changes strongly influence oceanic heat and moisture transport, which is a fundamental driver of the climate system and characterizes the climate variability (*Rind and Chandler*, 1991). Three largest climate transitions throughout the Cenozoic were associated with changes in ocean circulation, and driven by quite subtle tectonic motions. The declined CO_2 reduces the re-emission of the outgoing Earth heat radiation, hence the global heat budget and climate change. On the other hand, diminished water vapor associated with the cooling reduces the latent heating for extratropical cyclones (*Black*, 1998). Therefore, synoptic-scale meteorology in the mid-latitudes is also modulated.

Geological records suggest that the final closure of the Panama Seaway and the restriction

of the Indonesian Passages are among the keys to understand the climate evolution from the Pliocene to the pre-industrial. The tectonic evolution of the Panama Seaway is complex and long-lasting for millions of years since early Miocene (23–25 Ma B.P.; *Farris et al.*, 2011). From an oceanographic perspective, a critical threshold is the constriction of deep waterflow. *Montes et al.* (2015) suggests that deep and intermediate water mass exchange between both basins had already vanished at ∼15 Ma B.P.. However, ocean records indicate the existence of upper-ocean (less than 200 m) connections between the Caribbean Sea and the Pacific until the Pliocene (*Haug et al.*, 2001). Paleoenvironmental evidence indicate that the final closure of the Panama Seaway between ∼4.8–4 Ma B.P. were still sufficient to influence the ocean circulation and global climate (*Steph et al.*, 2010). The final closure of the Panama Seaway led to the development of salinity contrast between the Atlantic and the Pacific (*Steph et al.*, 2006), which initiated the strengthening of the Atlantic Meridional Overturning Circulation (AMOC) including the Gulf Stream and increased poleward heat and salinity transport (*Haug et al.*, 1999). Furthermore, this triggered overall shoaling of the tropical Pacific thermocline and the transition to the equatorial cold tongue state (*Steph et al.*, 2010). Shoaled thermocline depth allowed for stronger ocean-atmosphere interactions in the tropical Pacific, thereby invoking atmospheric teleconnection to broadcast the tropical signals globally (*Philander and Fedorov*, 2003).

The constriction of the Indonesian Passages is due to the collision between Australia and Southeast Asia. Since the earliest Miocene (∼25 Ma B.P.), Australia has been moving northward slowly and converging with Asia. Following the final closure of the Panama Seaway (∼4.8–4 Ma B.P.), the constriction and uplift of the Indonesian Passages (∼4-3 Ma B.P.), which refer to the passages between today's New Guinea and Sulawesi, reduce the heat and mass transport from the Pacific to the Indian via the Indonesian Throughflow (ITF). Warm waters deepened the thermocline in the west Pacific warm pool, warming the SSTs and increasing west-east Pacific SST gradient. The intensified Walker circulation driven by the SST gradient then projected local and remote climatic effects over the tropics and extratropics (*Molnar and Cronin*, 2015). On the other hand, the cooling in the Indian Ocean reduced precipitation in east Africa, causing the retreat of vegetation and expansion of desert (*Cane and Molnar*, 2001). Moreover, the constriction of Indonesian Passages may have reduced poleward heat transport associated with the AMOC by constraining the salinity transport to the Atlantic via the Agulhas current (*Karas et al.*, 2017). Such change is suggested to have preconditioned the onset of Northern Hemisphere glaciation and influenced global climate (*Cane and Molnar*, 2001). However, *Jochum et al.* (2009) found rather weak global climate impact of an altered Indonesian Passages with coupled climate model simulations. The simulated climatic impact is observed only in the equatorial Pacific and the properties of ENSO.

1.3 Tropical Pacific in paleoclimate

The tropical Pacific plays a significant role in the aforementioned hypothesis by determining the causes and characteristics of paleoclimate evolution (*Cane*, 1998). Three properties of ocean-atmosphere dynamics in the tropical Pacific, exemplified by the El Niño/Southern Oscillation (ENSO), are particularly prominent: high dependence and sensitivity to the mean state and its seasonal cycle; remarkable ability of reorganization; ability to broadcast tropical climate changes to the extratropics (*Chiang and Bitz*, 2005). ENSO is governed by a positive

coupled ocean-atmosphere feedback, the Bjerknes feedback. This feedback can be summarized as follows: warm (cold) SST anomalies in the eastern equatorial Pacific weaken (strengthen) the trade winds by mediating SST gradient, which in turn causes a thermocline deepening (shoaling) in the east which further enhances the SST anomalies. Much of the sensitivity is attributed to the rapid atmospheric response associated with tropical moist convection (on the order of a few hours) to the background climatic conditions (*Pierrehumbert*, 2000). In the Tropics, the convection perturbations could then generate Kelvin and Rossby waves that rapidly propagate across the longitude (*Matsuno*, 1966), which drives the SSTs through oceanic heat transport and thus reorganizes tropical convective climate. Furthermore, influences of anomalous tropical convection can be broadcasted globally via atmospheric Rossby waves and its interactions with the mid-latitude westerly flow (*Alexander et al.*, 2002). In addition, tropical ocean-atmohspere interactions can influence the AMOC in two ways. First, the hydrological cycle affects the freshwater budget in the tropical Atlantic (*Latif et al.*, 2000; *Schmittner et al.*, 2000). Second, changes in the tropical Pacific can readily affect interaction between the surface heat flux associated with winds and density-driven AMOC via atmospheric teleconnections (*Mignot and Frankignoul*, 2005). Thus, the ocean-atmosphere dynamics in the tropical Pacific could explain the paloclimate evolution associated with the mean state changes forced by varying continental configurations, greenhouse gas and the orbital variations (*Cane*, 1998).

1.4 Obliquity-driven climate variability

The Earth's orbit varies in three ways: the precession (the orientation of the Earth's rotational axis), the obliquity (the tilt of the Earth's rotational axis), and the eccentricity (the shape of the Earth's orbit). These orbital parameters sufficiently change the seasonal, seasonal and meridional, global averaged distribution of insolation at the top of the atmosphere, causing the climate to vary at 19 ka and 23 ka, 41 ka, 100 ka frequencies, respectively (*Berger*, 1988). In contrast to ∼100 ka glacial cycles in the late Pleistocene (0.8-0.01 Ma), orbital resolution records from both the North Atlantic and 57 globally distributed sites indicate high amplitude of climate variability to obliquity forcing during the interval of 3.2-2.5 Ma B.P. (Fig.1.2a,c). This geological interval, known as the Pliocene-Pleistocene transition, is among the major climate transitions, which featured significant development of northern hemisphere continental ice sheet, especially the Greenland ice sheet. During this climate transition, proxy data suggests progressively intensified climate variability to obliquity forcing (Fig. 1.2b,d). It is hypothesized that the interaction involving continental ice sheets and North Atlantic current that accounts for the high amplitude of obliquity-driven variability (*Lawrence et al.*, 2009). However, studies on the key mechanisms are further needed. Furthermore, *Martínez-Botí et al.* (2015) suggests that the earth system sensitivity, i.e., the sensitivity of Earth's climate to per doubling CO_2 during the Pliocene was identical to the late Pleistocene. Therefore, the impacts of the continental ice-volume on the climate response to obliquity forcing is of particular interest.

1.5 Thesis outline

To date, the influences of oceanic gateways on the Pliocene climate evolution, especially regional climate changes, and the mechanism for high amplitude of climate variability to obliquity

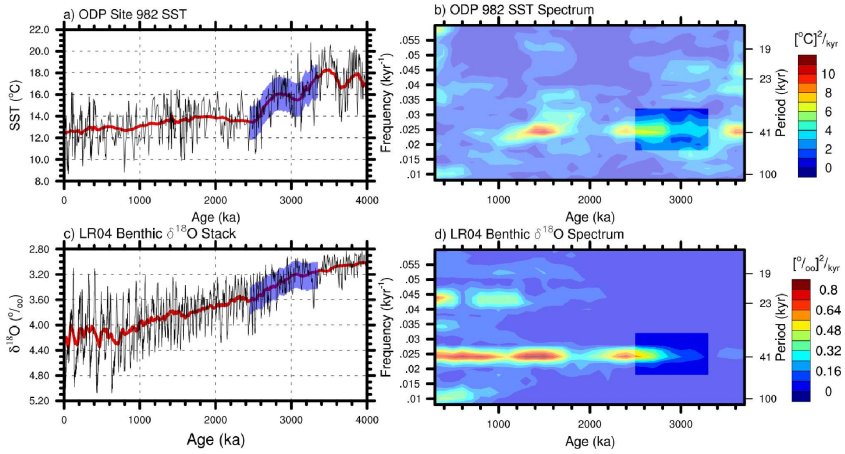

Figure 1.2: *Paleoclimate data during the last 4 Ma. (a) Time series of SST (Alkenone) from ODP site 982 (Lawrence et al., 2009) and (b) its evolutionary spectrum. (c) time series of an average of 57 globally distributed benthic $\delta^{18}O$ records (Lisiecki and Raymo, 2005) and (d) its evolutionary spectrum. Red lines in Fig.1.2a and Fig.1.2c are smoothed time series with a 300 ka running mean. Evolutionary spectra were computed using the ARAND software (Howell, 2001) with default settings (auto covariance function, a full linear detrend, a 600 ka window, a 50% lag, and an increment of 50 ka) of the iterative mode. All data were interpolated to even intervals of 2 ka temporal resolution and prewhitened by setting prewhitening equal to 1 prior to the spectral analysis. Each plot is scaled to its own maximum spectral density. The Pliocene-Pleistocene transition (3.3∼2.5 Ma) is highlighted with shadings.*

variation have drawn much attention but remain controversial. This thesis attempts to assess the impacts of oceanic gateways, declined atmospheric CO_2-concentration and the expansion of Greenland ice sheets on the climate evolution from the Pliocene to the pre-industrial by means of coupled ocean-atmosphere-sea ice general circulation model (CGCM) simulations and model-data comparison. CGCM provides a numerical and comprehensive representation for dominant large-scale features of the climate system. It is an irreplaceable tool for investigating the underlying mechanisms for climate evolution. The following questions are discussed in three individual chapters.

1. What are the model sensitivities to seaway and CO_2 changes with respect to the large-scale features and East Asian summer monsoon during the Pliocene?

2. What are the influences of seaway and CO_2 changes during the Pliocene on tropical pacific climate with respect to mean sate, annual cycle, ENSO, and their Interactions?

3. How does the expansion of Greenland ice sheet enhance sensitivity of Pliocene-Pleistocene climate to obliquity forcing?

Each chapter includes an introduction, experimental design, results, and discussion section. Chapter 2 will show the results from a set of model sensitivity studies, to investigate the impacts of oceanic seaway and CO_2 changes on the global climate and Asian monsoon during the Pliocene. Chapter 3 addresses the tropical Pacific climate change and chapter 4 the increased climate variability to obliquity forcing. Both are reprints of published journal articles. Summary and discussions are given in chapter 5.

Chapter 2

The Impacts of Seaway and CO_2 Changes on the large-scale features of the Pliocene Climate: Results from Model Sensitivity Studies

Abstract

The Pliocene epoch from about 5.3 million to 2.6 million years before present is the most recent period of sustained global warmth similar to the near future projections. The restriction of the Indonesian Passages, the closure of the Panama Seaway and declining atmospheric CO_2-concentration are suggested to have caused the global climate evolution to the present-day condition. Here, we present the Pliocene sea surface temperature (SST) reconstructions, East Asian Summer Monsoon (EASM) records, along with sensitivity experimental results from the Kiel Climate Model. We find that, in terms of SST, simulated model sensitivity to CO_2 is in good agreement with the Pliocene reconstructions in most regions except the North Atlantic and Arctic. This suggests underestimation of climate feedback in the high-latitudes and the necessity for improved boundary conditions. In terms of large-scale features, the simulated mean state is most sensitive to the CO_2 changes, while the influences of seaway changes are restricted within the tropics.

Influences of declining CO_2 on the EASM are more prominent. An intensification of the intensity of EASM by $\sim$50% is simulated in response to the declining CO_2, which is largely attributed to the strengthened land-ocean thermal contrast, while the precipitation decreases by $\sim$4.8%. In contrast, the restriction of two seaway changes only drives relatively weak changes with respect to wind speed and precipitation. A water vapor budget analysis suggests that the reduced atmospheric moisture content due to decreasing CO_2 significantly contributes to precipitation response.

2.1 Introduction

The Pliocene epoch, from 5.3 to 2.6 million years before present (Ma B.P.), was characterized as a period of global cooling and evolving towards the present-day climate. Paleogeochemical proxies indicate an atmospheric CO_2-concentration similar to the present-day values, with concentrations amounting to ∼405 ppm (parts per million by volume) (*Haywood et al.*, 2011). In particular, the global mean temperature during the mid-Pliocene (∼3.3–3 Ma B.P.) was 2–3°C warmer, global sea level 25 m higher than today (*Dowsett*, 2007). The Northern Hemisphere continental ice sheet extensively developed, especially over Greenland, in the late Pliocene around 3 Ma B.P. (e.g., *Lisiecki and Raymo*, 2005; *Rohling et al.*, 2014).

During the Pliocene, a number of significant oceanic seaway changes created the modern ocean geometry and had profound effects on global and regional climate evolution (e.g., *Haug and Tiedemann*, 1998; *Cane and Molnar*, 2001). The closure of the Panama Seaway that connected the tropical Atlantic to the Pacific has been one of the predominant seaway changes. The tectonic evolution of the Panama Seaway is complex and long-lasting for millions of years since early Miocene (23–25 Ma B.P.; *Farris et al.*, 2011). From an oceanographic perspective, a critical threshold is the constriction of deep water flow. *Montes et al.* (2015) suggests that deep and intermediate water mass exchange between both basins had already vanished at ∼15 Ma B.P.. However, ocean records indicate the existence of upper-ocean connections between the Caribbean Sea and the Pacific until the Pliocene (*Haug et al.*, 2001). Notably, paleoceanographic data indicate that the final closure of the Panama Seaway between ∼4.8–4 Ma B.P. were still sufficient to influence the ocean circulation and global climate (*Steph et al.*, 2010). Numerical modeling studies show that the final closure enhances the Atlantic Meridional Overturning Circulation (AMOC), by differing magnitudes depending on the configuration of the seaway and the selection of climate models (*Zhang et al.*, 2012b), as the closure of seaway enhances the salinity contrast between the Pacific and Atlantic. Enhanced AMOC is also suggested to have caused the shoaling of thermocline depth in the east equatorial Pacific (*Steph et al.*, 2010), which is supported by model results (*Zhang et al.*, 2012b). The shoaled thermocline depth may have preconditioned the modern Pacific cold tongue and favored the development of ENSO. On the other hand, the warmer SSTs in the North Atlantic associated with strengthened AMOC would have increased the precipitation and presumable glaciation over Greenland (*Haug and Tiedemann*, 1998). However, paleoclimate reconstructions (*Lawrence et al.*, 2010) suggest gradual cooling in the North Atlantic at the same period. Furthermore, climate model experiments suggest the glaciation over Greenland is controlled by declining CO_2 but not increased precipitation (*Lunt et al.*, 2008).

The constriction of the Indonesian Passages is due to the collision between Australia and Southeast Asia. Since the earliest Miocene (∼25 Ma B.P.) Australia has been moving northward slowly and converging with Asia. Following the final closure of the Panama Seaway (∼4.8–4 Ma B.P.), the restriction of the Indonesian Passages (∼4-3 Ma B.P.) played a prominent role in constraining warm and salty water entering the Indian Ocean from the Pacific (e.g., *Karas et al.*, 2009, *Karas et al.*, 2017). *Karas et al.* (2017) further suggested that the constriction of the Indonesian Passages might have weakened the AMOC by reducing the salinity transport into the Atlantic Ocean from the Indian Ocean. Such change is suggested to have preconditioned the onset of Northern Hemisphere glaciation and influenced global climate, including the aridification of East Africa (*Cane and Molnar*, 2001). However, *Jochum et al.* (2009) found rather

weak global climate impact of an altered Indonesian Passages with coupled climate model simulations. The simulated climatic impact is observed only in the equatorial Pacific and the properties of ENSO. Additionally, *Krebs et al.* (2011) found that the restricted Indonesian Passages could explain the aridification of northwestern Australia during the Plio–Pleistocene. The East Asian Summer Monsoon (EASM) is one major component in the global climate system and provides fresh water resources for the most populated regions in the world. The EASM is mainly driven by the land-ocean thermal contrast. Due to the different thermal capacity of land and ocean, a warm low-pressure system over the East Asia continent drives southerly winds and brings precipitation into East Asia during boreal summer (JJA). Multifold geological evidence for surface air temperature and precipitation revealed the EASM evolution since the Pliocene. Biological and geochemical records indicate drying climate and weakening EASM trend from 4.5 to 2.7 Ma B.P. on the Chinese Loess Plateau (e.g., *Ge et al.*, 2013; *Wang et al.*, 2006). However, recent magnetic proxies contradict these records, which revealed a cooling and wetting climate at the same period (*Nie et al.*, 2014). Furthermore, by extending the rock magnetic parameter record to ∼4.8-4.3 Ma B.P., *Nie et al.* (2014) suggests a link between the final closure of the Panama Seaway and enhanced precipitation associated with intensified EASM. The idea is that the closure of Panama Seaway strengthened the high pressure center over the North Pacific, enhancing southerly winds, which in turn intensify the precipitation brought by EASM (*Nie et al.*, 2014). A group of proxy data with a decent age control ranging from 3.0-3.3 Ma B.P., which indicates relatively reliable cooling temperature and/or decreasing precipitation, suggests a weakening trend of EASW since the mid-Pliocene (2.1). Atmospheric CO_2-concentration could also modulate the EASM. Modeling studies show a weakening trend of EASM under global warming (*Li et al.*, 2010).

In this study, we investigate the sensitivity of the KCM's large-scale circulation and mean state to external changes during the Pliocene, forced by changes in atmospheric CO_2 and ocean geometry. Special attention is given to the influence of final closure of the Panama Seaway (∼4.8-4 Ma B.P.) and the restricted of Indonesian Passages (∼ 4.-3. Ma B.P.), and to the mean climate and the EASM response. The structure is as follows. In section 2.2, we describe the coupled model and the experimental design. Mean state changes and the verification of model sensitivity are presented in section 2.3. The response of large-scale circulation is addressed in section 2.4. In section 2.5, the EASM is discussed along with the decomposition of precipitation. We conclude with a brief summary and a discussion of the main results in section 2.6.

Proxy Type	Location	Age (Ma B.P.)	Geological Record	Reconstructed climate	Reference
Rock magnetic	35.1°N, 107.2°E	4.8-2.7	Air temperature and precipitation	Cooling and wetting climate	*Nie et al.* (2014)
Pollen	35.88°N, 107.97°E	4.5-3.7	Decreased forest plants, occurrence of desert	Cooling and drying climate	*Wang et al.* (2006)
Pollen	36.27°N, 105.98°E	3.3-3.0	More tree and shrubs, fewer herbs	Wetter (relative to pre-industrial)	*Jiang and Ding* (2008)
Pollen	35.12°N, 107.2°E	3.0-2.6	Cupressaceae, forest vegetation	Warmer and wetter (relative to pre-indutrial)	*Wu et al.* (2007)
Pollen	35.12°N, 107.35°E	3.3-3.0	Cupressaceae, Juniperus and lower Ulmus	Warmer and wetter (relative to pre-indutrial)	*Ma et al.* (2005)
Pollen	38.37°N, 91.73°E	3.1-3.0	More broad-leaved trees, fewer xerophytic taxa	Warmer and wetter (relative to pre-indutrial)	*Cai et al.* (2012)
Pollen	37.80°N, 94.80°E	3.3-3.0	Existence of subtropical trees	Warmer and wetter (relative to pre-indutrial)	*Wu et al.* (2011)

Table 2.1: *Reconstructed Proxy for the East Asian summer monsoon during the Pliocene.*

2.2 Model, experimental setup and methods

The Kiel Climate Model (KCM, *Park et al.*, 2009 is used in this study. The KCM consists of the ECHAM5 as the atmosphere model (*Roeckner et al.*, 2003) running on a T31 (3.75° x 3.75°) horizontal resolution, with 19 vertical levels up to 10 hPa. It is coupled to the NEMO ocean-sea ice component (*Madec*, 2008) running on a 2° Mercator mesh, with 31 vertical levels, through the OASIS3 coupler (*Valcke*, 2006). The meridional resolution for the ocean component enhances towards lower latitudes, with ∼0.5° in the equatorial region. The ocean and the atmosphere component is coupled once per day without employing any form of flux correction.

Four experiments are conducted (Table 2.2) aiming to separate the model sensitivity of lowering atmospheric CO_2, constriction of the Indonesian Passages and closure of the Panama Seaway. The experiment **Pre-industrial** is simulated with low-CO_2 (286 ppm) and modern Indonesian Passages and modern Panama Seaway. This experiment is integrated for 3,200 years starting from the Levitus climatology of temperature and salinity, which serves as a control simulation. Experiment **Plio** differs from experiment **Pre-industrial** only in the CO_2-concentration which is higher (405 ppm). **Plio** serves as sensitivity run for the high-CO_2 experiments. The other two experiments, which investigate the effects of two seaway changes, are initialized with the output from **Plio** and integrated for 1,800 years. The last 300 years monthly output from each of the experiments are used for analysis.

Experiment	CO_2 (ppm)	Indonesian Passages	Panama Seaway	Integration
Pre-industrial	286	Modern	Modern	3200
Plio	405	Modern	Modern	3500
Indo. Passages	405	Pliocene	Modern	1800
Panama Seaway	405	Modern	Pliocene	1800

Table 2.2: *Overview of the model simulations analyzed in this study. The depth of the Panama Seaway is 106 m. The unit for the length of integration is year.*

The geometry for the Indonesian Passages and the Panama Seaway during the Pliocene are shown in Fig. 2.1. *Cane and Molnar* (2001) suggested the deeper and wider geometry of the Indonesian Passages during the early Pliocene: the passages between Sulawesi and New Guinea are 1,000 m deeper relative to the modern bathymetry, the northern coast of New Guinea is located 2° south due to the missing of the northern part, and the passage between Timor and Australia is also wider and deeper by removing part of Timor.

An open Panama Seaway is represented in the model by replacing four land grids by ocean grids between North and South America at ∼8°N. We employ a depth of 106 m representing an open Panama Seaway to simulate the final stage of the shoaling process between 4.8 and 4.0 Ma B.P. (*Haug et al.*, 2001).

We compare the simulated SST with the reconstructions from various types of proxies for the mid-Pliocene. The reconstructed dataset, which consists of 95 globally distributed sites, is from the Pliocene Research, Interpretation and Synoptic Mapping (PRISM) project (*Dowsett et al.*, 2012). The estimates for SST are averaged over the time period between 3.264 and 3.025 Ma B.P.. The foraminifera based proxies, which are widely distributed in the low- and mid-latitudes, are of relatively higher confidence compared with other types (*Dowsett et al.*, 2012). The Hadley Centre Sea Ice and Sea Surface Temperature data set (HadISST) is used as the

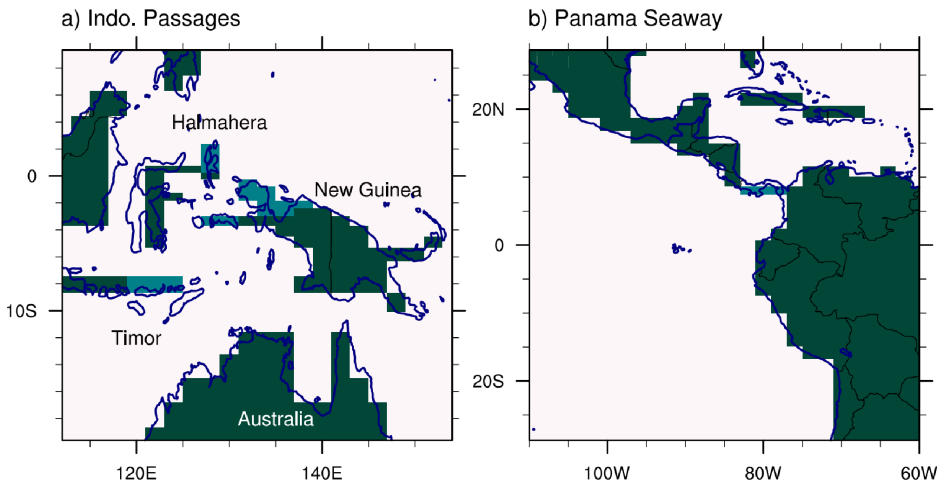

Figure 2.1: *Oceanic gateways and their representations in the KCM. (a) The Indonesian Passages and its representation in the model. Dark green shaded regions indicate the Pliocene configuration, light green shaded areas indicate the difference to modern geometry, and blue contours show the modern coastlines. (b) Same as a) but for the Panama Seaway.*

observed SST. The HadISST is on a global 1° x 1° grid covering the period from 1870 to 2017. Only a sub-period (1870-1930) average is employed to represent the pre-industrial climatological mean.

The mass stream function along the equator (5°S∼5°N) is calculated to measure the Walker circulation after *Yu and Zwiers* (2010),

$$\psi = 2a\pi \int_{10hPa}^{Surf} u_D \frac{dp}{g} \tag{2.1}$$

where u_D, a, p and g are the divergent component of the zonal wind, the radius of the earth, the pressure and gravitational acceleration, respectively. The zonal wind is meridionally averaged between 5°N and 5°S and integrated from 10 hPa to surface.

The Hadley circulation is represented by calculating the zonal mean stream function following the equation

$$\psi = 2a\pi \cos\theta \int_{10hPa}^{Surf} v \frac{dp}{g} \tag{2.2}$$

where v, a, θ, p and g are the zonal mean merdional wind, the latitude, the radius of the earth, the pressure and gravitational acceleration, respectively.

2.3 Model sensitivity

2.3.1 Mean climate

In this section, we address the responses of mean state to CO_2 and seaway changes. Decreasing atmospheric CO_2-concentration alters the radiation balance at the top of the atmosphere and hence the poleward heat transport. The constrictions of both seaways allows for the reorganization of large-scale ocean and atmosphere circulation, which redistributes heat and salt. Furthermore, the surface temperature and hydrological cycle also respond to these changes. Lower atmospheric CO_2 in **Pre-industrial** dominates the global averaged SST and 2m-air-temperature response, which amount to -2.33°C and -3.12 K, while the constriction of Indonesian Passages and the Panama Seaway lead to a slight warming of SST and 2m-air-temperature (Table 2.3). The global averaged SST response to decreasing CO_2 is within the range (∼2-3°C) estimated from proxies, suggesting the dominant role of CO_2 on the surface temperature evolution from the Pliocene to the pre-industrial. Both the Arctic and Antarctic sea ice extent and volume illustrates significant increase at lower CO_2 due to polar amplification (Table 2.3). In contrast, the constriction of both seaways reduces the Arctic and Antarctic sea ice with respect to the volume but not the extent. Additionally, lower CO_2 significantly enhances the averaged ice sheet accumulation rate by 45.8 mm/yr (∼44%), especially over south and west Greenland (Fig. S2.1). Constraint of both seaways slightly slows down the glaciation over Greenland (Table 2.3). The relative change, however, is less than 10%. *Cane and Molnar* (2001) and *Haug and Tiedemann* (1998) hypothesized that both the restriction of the Indonesian Passages and the closure of the Panama Seaway contribute to the Northern Hemisphere glaciation. Contradictory to their hypothesis, our result suggests that the Northern Hemisphere glaciation during the late Pliocene may not be attributed to the changes in the oceanic gateways. Despite the enhanced precipitation over Greenland due to both seaway changes, the warmer temperature increases the melting of ice sheet at lower topography (Fig. S2.1). An overall effect of the constriction of both seaways reduces the accumulation of Greenland ice sheet. The glaciation may have been dominated by declined CO_2, which largely reduces ice sheet melting, especially in JJA (not shown).

Variable	Annual mean for **Plio**	Response to decresing CO_2	Response to restricted Indo. Passages	Response to closed Panama Seaway
Global mean SST (°C)	18.44	−2.33	+0.08	+0.17
Global mean SAT (K)	287.70	−3.22	+0.16	+0.32
GrIS accumulation (mm/yr)	105.1	+45.8	−7.6	−9.6
Global mean precip. (mm/day)	2.85	−0.21	+0.01	+0.02
NH sea ice extent (km^2)	12782	+3082	+7	−480
SH sea ice extent (km^2)	10353	+7592	−384	−419
NH sea ice volume (km^3)	30494	+25672	−901	−4108
SH sea ice volume (km^3)	7778	+7588	−291	−255

Table 2.3: *300-year global annual mean climate parameters for all experiments. Response to decreasing CO_2 is defined as the difference between the **Pre-indutria** and **Plio**. Response to the restricted **Indo. Passages** is defined as the difference between **Plio** and **Indo. Passages**. Resposen to the closed Panama Seaway is defined as the difference between **Plio** and **Panama Seaway**.*

Next we examine the responses of zonal mean variables. As shown in Fig. 2.3a, lower CO_2 cools the zonal mean temperature by ∼2 K, while the impacts of seaway changes hardly show up. Additionally, the precipitation between 10°S and 10°N is suppressed from 5.23 mm/day in

Plio to 4.66 mm/day in **Pre-industrial**, in response to low CO_2 (Fig. 2.2a). The constriction of Indonesian Passages and the Panama Seaway slightly enhances the precipitation by 0.15 mm/day and 0.19 mm/day over the tropics between 10°S and 10°N Fig. 2.2b), in relative to **Plio**. Increased cloud cover in **Pre-industrial** strengthens the re-emission of radiation, which is consistent with the temperature response (Fig. 2.2c). According to the Clausius-Clapeyron relation, a cooler atmosphere holds less water vapor. As shown in Fig. 2.2d, lower CO_2 in **Pre-industrial** significantly reduces the column integrated water vapor by ∼10 kg/m^2 in the tropics (10°S-10°N). The closure of Panama Seaway increases the water vapor content by ∼3 kg/m^2 over the tropics, which is stronger than the constriction of the Indonesian Passages (Fig. 2.2d)., The influences of both seaway changes barely reach the extratropical region.

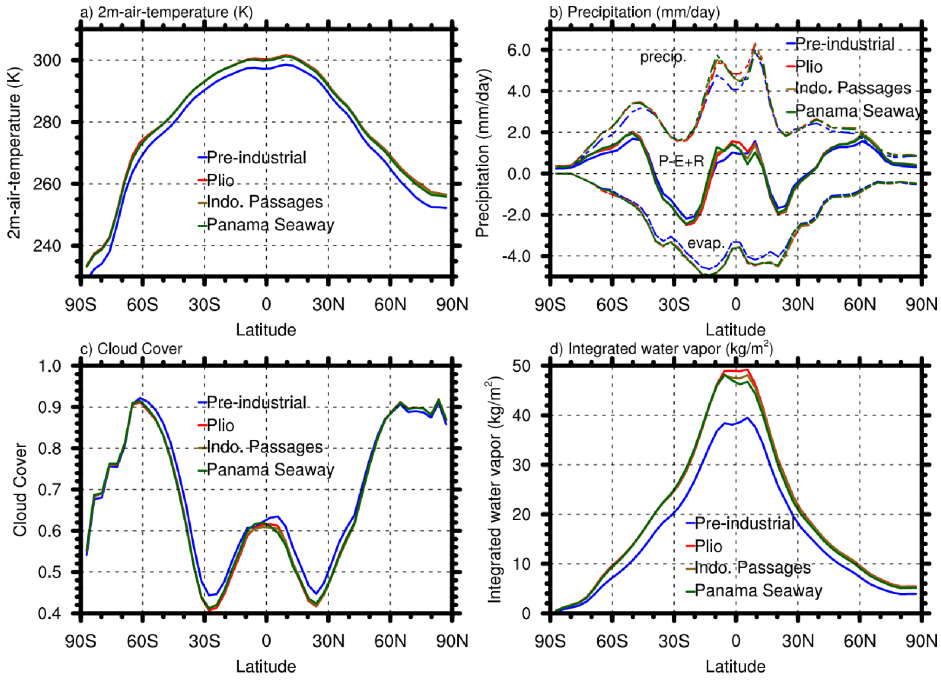

Figure 2.2: *(a) Zonally averaged 2 m air temperature (K). (b) Zonally averaged precipitation, evaporation and total freshwater balance (defined as precipitation minus evaporation plus river runoff, in mm/day). (c) Zonally averaged cloud cover. (d) Zonally averaged column integrated water vapor.*

The impacts of CO_2 and seaway changes on the SST are not spatially homogeneous (Fig. 2.3), indicating the reorganization of large-scale circulation. In response to lower CO_2, relatively weaker cooling occurred in the western boundary current regions in the Northern Hemisphere, especially over the Kuroshio and Gulf Stream region (Fig. 2.3a). Both could be attributed to the enhanced heat transport associated with the strengthened North Equatorial Current (NEC), which is driven by the enhanced trade winds (*Wang et al.*, 2016; *Duan et al.*, 2017). The Indonesian Throughflow (ITF) also strengthens from 14.75 Sv in **Plio** to 15.0 Sv in **Pre-industrial**, which contributes to the stronger cooling in the Pacific warm pool than the equatorial Indian Ocean. Weaker cooling in the high latitudes is attributed to the increased sea ice fraction (Table 2.3) that hinders the ocean-atmosphere heat exchange. The impacts of two seaway changes are similar, with the closure of Panama Seaway illustrating stronger effect (Fig. 2.3b, c). The constriction of Indonesian Passages warms the equatorial Pacific and cools the Indian due to a weakening of the ITF by ∼2.7 Sv. Reduced heat transport associated with

the ITF further cools the southern Indian and Atlantic Ocean. The closure of Panama Seaway prevented the water exchange amounting to ∼6.5 Sv between the Pacific and the Atlantic. The SST response is asymmetric between two hemispheres, with general warming in the Northern Hemisphere and cooling in the Southern Hemisphere except the Bellingshausen Sea and the Amundsen Sea (Fig. 2.3c).

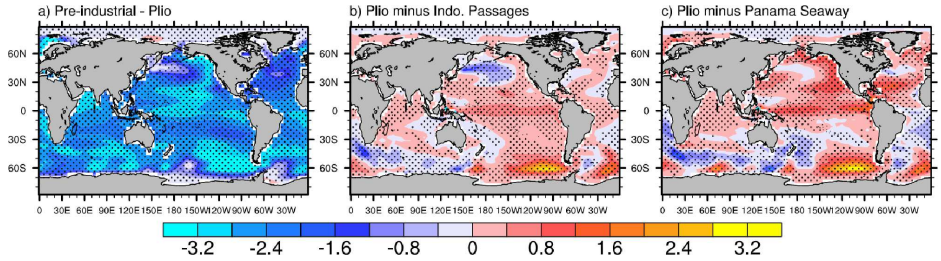

Figure 2.3: *SST (°C) responses to (a) decreasing CO_2, (b) the constriction of Indonesian Passages and (c) the final closure of Panama Seaway. Stippling indicates the differences are significant at the 95% confidence level using Student's t-test.*

According to a Student's t-test, the impact of low CO_2 on freshwater balance is significant in the tropics, between 30°N and 30°S (stippling in Fig 2.4a). Largely reduced precipitation in the Pacific warm pool and increased precipitation in the cold tongue suggest weaker convection due to surface cooling in **Pre-industrial**. Additionally, much reduced precipitation is observed over subtropical Africa and South America. *Cane and Molnar* (2001) suggested a possible link between the constriction of Indonesian Passages and the African aridification around 4∼3 Ma B.P.. Our results show that a declined CO_2 can also cause such aridification. In addition, the precipitation response depicts a wetter condition in the subtropics and a drought in the mid-latitudes.

The effects of seaway changes on freshwater response are quite similar. Both the constriction of the Indonesian Passages and closure of the Panama Seaway cause wetter conditions to the east of the Maritime Continent, and drought to the west (Fig. 2.4b, c). Furthermore, the drought over subtropical Africa and equatorial Atlantic is strongly amplified due to the closure of the Panama Seaway, in comparison with that of the Indonesian Passages.

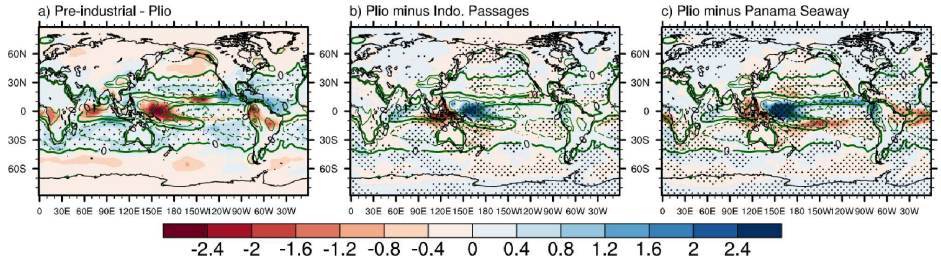

Figure 2.4: *Freshwater balance (P-E+R, Unit: mm/day) responses to (a) decreasing CO_2, (b) the constriction of the Indonesian Passages and (c) the final closure of the Panama Seaway. Green contours indicate the annual mean freshwater balance for* ***Plio*** *(contour interval: 2 mm/day). Stippling indicates the differences are significant at the 95% confidence level using a Student's t-test.*

2.3.2 Comparison to proxy data

Next we compare the simulated SST with the SST reconstructions from the PRISM project. There are 95 marine locations in total, which are distributed globally (Fig. 2.5a). The reconstructions in low- and northern mid-latitudes are generally of high confidence, while the high- and southern mid-latitude reconstructions are of relatively low confidence, due to the limitations of reconstruction method or a low temporal resolution between 3.264 and 3.025 Ma B.P. (*Dowsett et al.*, 2012). We first compare the simulated climatological mean SST with the proxies, and then the simulated SST difference between the **Plio** and **Pre-industrial** with the observed difference. Here the observed SST difference between the **Plio** and **Pre-industrial** is estimated by subtracting the interpolated HadISST from the PRISM dataset at each proxy location.

To assess the model performance, we first compare the simulated zonally averaged annual mean SST. The high-CO_2 experiments with different seaway configurations are generally in good agreement with reconstructions in the Southern Hemisphere, while models substantially underestimate the polar amplification in the Northern Hemisphere (Fig. 2.5b). The model-proxy discrepancy over the northern mid- and high-latitudes amounts to a maximum of 10°C, especially over the North Atlantic and Arctic region (not shown). Neither of the tropical seaway changes helps to reduce this discrepancy. A pointwise comparison is further shown in Fig. 2.5c by interpolating the simulated SST in **Plio** to each proxy site. The annual mean interpolated SST in **Plio** is 15.13°C, in comparison to an average of 17.67°C for the proxies. Additionally, various types of proxies confirmed the underestimated warming in the Northern Hemisphere.

Apart from the northern mid- and high-latitudes, the SSTs over California and Peru coastal upwelling regions significantly cool down, in comparison to the mid-Pliocene (Fig. 2.6a). On the contrary, the SSTs over the Atlantic upwelling region remain quite stable (Fig. 2.6a). Considering the model bias for the KCM to reproduce pre-industrial mean climate, we calculate the difference between **Plio** and **Pre-industrial** to cancel the model errors. The SST changes in the tropics are relatively modest, ranging from -2 to 2°C as suggested by the observations (red symbols in Fig. 2.6b). However, the simulated difference between **Plio** and **Pre-industrial** is quite uniform in signs, amounting to about 2-3°C. This suggests the missing of negative feedbacks or the inaccuracy of boundary conditions in **Plio**. The southern ocean is still in generally good agreement with the observed SST difference. On the other hand, the model-data discrepancy in the Northern Hemisphere remains quite large, with the simulated SST difference ranging from less than ∼2°C and the observation amounting to ∼9°C. By far, no climate models could fully reproduce the warming during the mid-Pliocene as suggested by the proxies. This may provide new sights into the mid-Pliocene boundary conditions or even the predictive abilities of the climate model.

2.4 Large-scale circulation

2.4.1 Walker circulation

The results of precipitation changes imply the general modification of atmospheric circulation to seaway and CO_2. The response of zonally averaged meridional (5°S∼5°N) mean stream function is shown in Fig. 2.7 Positive (solid contours in Fig. 2.7) and negative values (dashed contours in

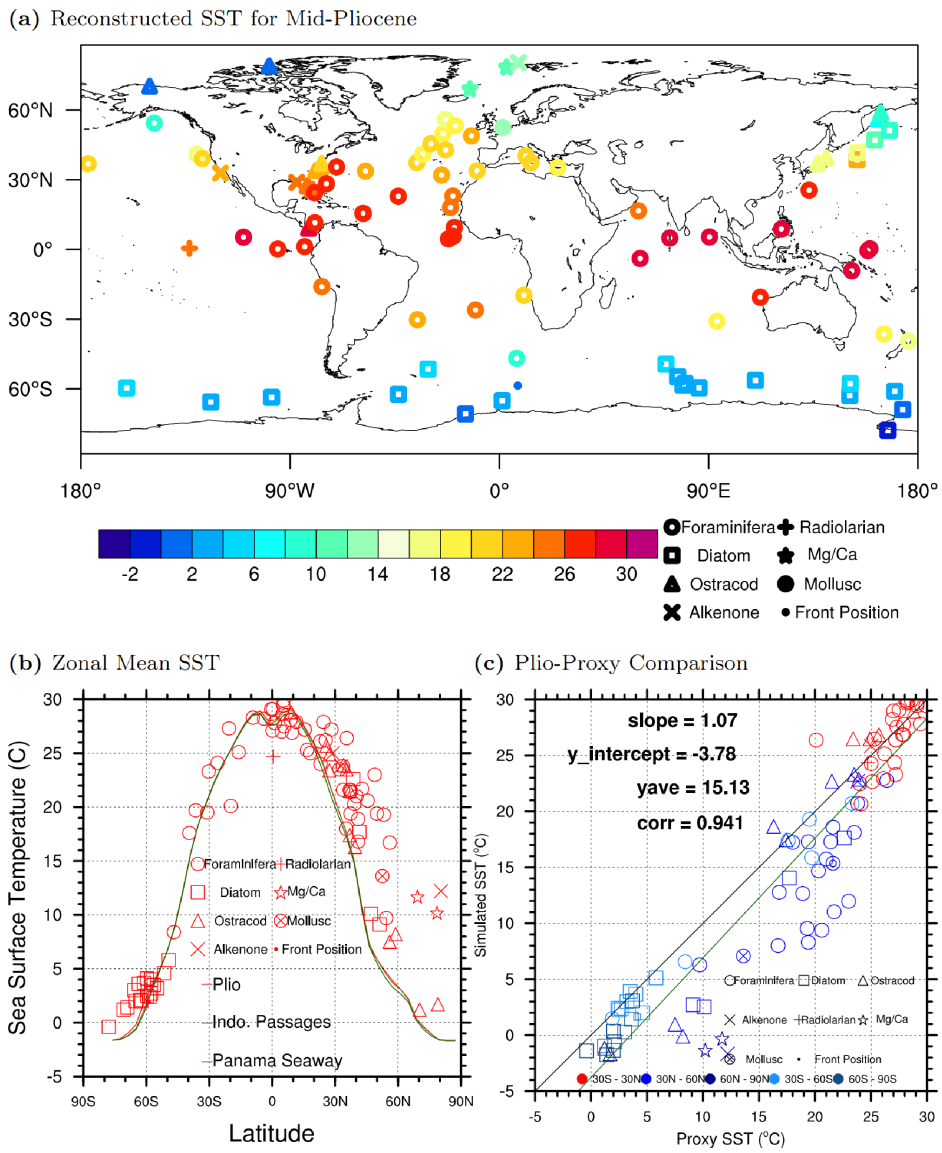

Figure 2.5: *Model-data comparison. (a) Mean annual SST from PRISM dataset at 95 sites. (b) SST proxies superimposed on zonally averaged annual mean SST from three high-CO_2 simulations. (c) Scatter plot showing the comparison between PRISM3 SSTs and the simulated annual mean SSTs in* ***Plio****. The* ***Plio*** *SSTs are interpolated to each proxy site. The black line in Fig. 2.5c indicates the ideal regression for the simulated SST and observations, while the green line is the realistic regression.*

Fig. 2.7) indicate a clockwise and an anticlockwise circulation, respectively. Positive (negative) differences (shading) over the negative (positive) mean circulation (contours) represent a slow-down of circulation. The thick zero contours of mean circulation indicate three main convention regions over Africa, the Maritime Continent and South America. The most prominent feature in the Walker circulation response to seaway and CO_2 changes is the shift of the Pacific cell in the zonal direction. Here, we quantify the location of the Pacific cell with the zero contour of the stream function over the Pacific warm pool, which defines the approximate location of the maximum convection. Lower CO_2 induces a westward shift of the Pacific Walker circulation

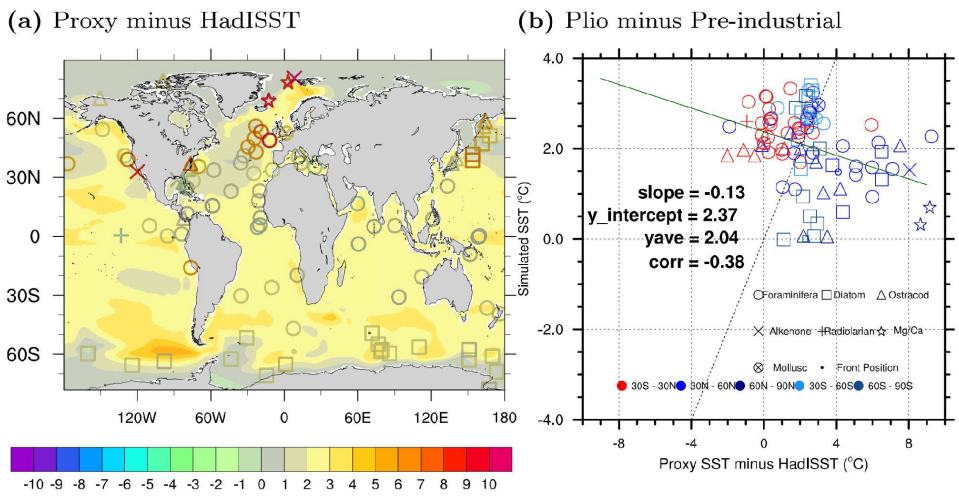

Figure 2.6: *(a) Observed difference between PRISM SST dataset and HadISST dataset (averaged between 1870 and 1900) showing the observed SST change between the mid-Pliocene and the pre-industrial. (b) Scatter plot showing the simulated SST difference between* ***Plio*** *and* ***Pre-industrial*** *and the observed SST difference. The black line in Fig. 2.6b indicates the ideal regression for the simulated SST and observations, while the green line is the realistic regression.*

from 159°E in **Plio** to 152°E in **Pre-industrial**. The intensity of Indian Ocean cell, defined as the averaged stream function between 300 and 600 hPa over the Indian ocean from 60°E to 90°E, strengthens from -1.06x10^{11}kg/s to -1.44x10^{11}kg/s in response to decreasing CO_2. The restricted Indonesian Passages and closed Panama Seaway both cause eastward shift of the Walker circulation, from 152°E in **Indo. Passages** and 150°E in **Panama Seaway** to 159°E in **Plio**. The intensity of the Pacific Walker Cell, defined as the averaged stream function between 300 and 600 hPa from 120°W to 160°W, remains relatively stable across various seaway configurations but not the Indian cell and Atlantic cell (Fig. 2.7b, c). Restricted Indonesian Passages weakens the Indian Ocean cell from -1.34x10^{11}kg/s to -1.06x10^{11}kg/s, while closed Panama Seaway significantly weakens both the Indian cell and Atlantic cell, from -1.27x10^{11}kg/s to -1.06x10^{11}kg/s and from -1.36x10^{11}kg/s to -1.06x10^{11}kg/s, respectively.

2.4.2 Hadley circulation

The Hadley circulation, the meridional component of three-dimensional tropical atmospheric circulation, transports large amount of energy and angular momentum poleward and thus, plays a pivotal role in the Earth's climate. The ascending and subsiding branches of the Hadley cell determines the locations of ITCZ, and the subtropical dry zones where major tropical/subtropical deserts are distributed. Substantially weakened Hadley cells in both Hemispheres are simulated in **Pre-industrial**, in comparison with **Plio** (Fig. 2.8a). The annual mean location of ITCZ shift southward by ∼1.5° in response to lower CO_2. Thus, the decreased precipitation intensity over the tropical region in Fig. 2.4a is attributed to the weaker Hadley cell and reduced water vapor content. Both seaway changes intensify the Hadley cell, especially its Northern Hemisphere branch (Fig. 2.8b, c). A stronger subsiding northern branch (Fig. 2.8b, c) reduces the precipitation over the Sahara desert, east and southwest Africa (Fig. 2.4b, c). This is consistent with pollen-based precipitation data (*DeMenocal*, 2004; *Dupont et al.*,

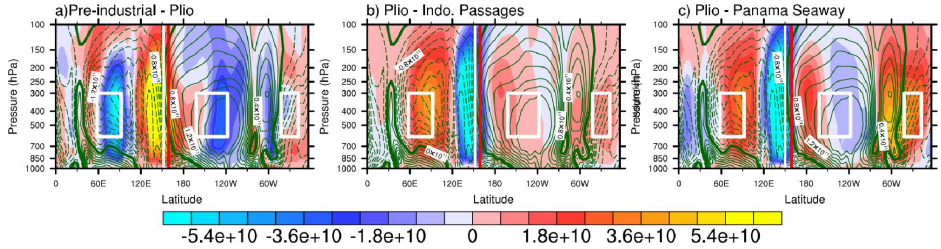

Figure 2.7: *Responses (shading) of atmospheric stream function (unit: kg/s) along the equator (5°S-5°N) to (a) decreasing CO_2, (b) the constriction of the Indonesian Passages and c) the closure of the Panama Seaway. Contours depict climatological mean stream function along the equator. The white boxes ranging between 300 hPa and 600 hPa over 60∼90°E, 160∼120°W and 40∼20°W indicate the Indian Ocean cell, Pacific Ocean cell and Atlantic Ocean cell, respectively (Yu and Zwiers, 2010). The thick red lines indicate the location of Pacific Walker cell for* ***Plio****. Green contours indicate the annual mean stream function for* ***Plio*** *(contour interval: 0.2 $x10^{11}$ kg/s). The white lines in Fig. 2.7a-c indicate the locations of Pacific Walker cell for* ***Pre-industrial****,****Indo. Passages*** *and* ***Panama Seaway****, respectively.*

2005). On the other hand, the location of ITCZ barely shifts to seaway changes. The northward heat transport associated with the Hadley cell decreases slightly (∼0.2 PW at 46°N) in **Pre-industrial**, and remains rather stable across both seaway configurations (Fig. S2.2).

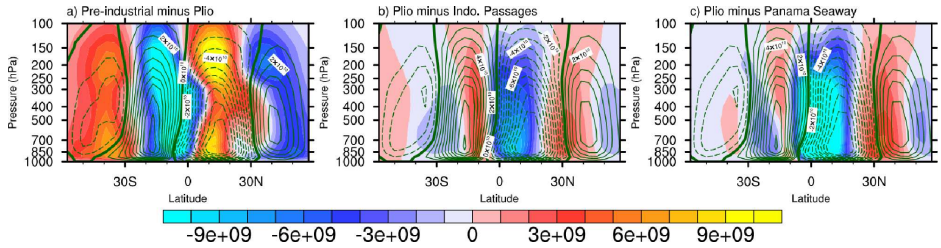

Figure 2.8: *Responses (shading) of zonal mean atmospheric stream function (unit: kg/s) to (a) decreasing CO_2, (b) the constriction of the Indonesian Passages and (c) the closure of the Panama Seaway. Green contours depict the climatological zonal mean stream function for* ***Plio*** *(contour interval: 2 x 10^{10}kg/s).*

2.4.3 Atlantic meridional overturning circulation

Marine proxies suggest a gradually cooling trend in the North Atlantic since 5 Ma B.P. (Fig. 1.1d). A slow-down of AMOC could have contributed to the reduced northward heat transport, thus explaining this remarkable cooling. Seaway and CO_2 changes could modify the surface heat flux and salinity transport thereby affecting density-driven AMOC. Here, we define the AMOC index as the maximum barotropic stream function at 30°N. Compared to **Plio**, a slow-down of the upper AMOC and a speed-up of lower AMOC are simulated in **Pre-industrial** (Fig. 2.9a). However, the AMOC index barely changes in response to lower CO_2. The constriction of the Indonesian Passages induces an eastward shift of Walker cell and largely reduces the freshwater input into the tropical Indian Ocean (Fig. 2.4b). More saline water is transported into the Atlantic Ocean and enhances the convection over the Irminger and Greenland-Iceland-Norwegian Seas (not shown). As a result, the AMOC index slightly enhances by ∼0.3 Sv

(Fig. 2.9b). The final closure of the Panama Seaway prevents an eastward volume transport of less saline water from the Pacific to the Atlantic by ∼6.5 Sv, thereby increasing the poleward salinity transport associated with the Gulf Stream. Thus, enhanced convection strengthens the AMOC by ∼2.0 Sv (Fig. 2.9c).

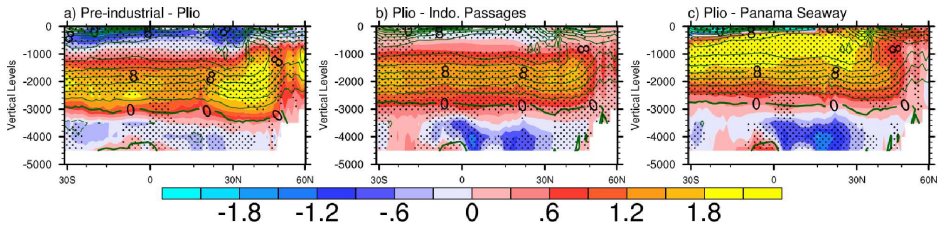

Figure 2.9: *Responses (shading) of barotropic stream function (unit: Sv; 1 Sv = $10^6 m^3/s$) to (a) decreasing CO_2, (b) the constriction of the Indonesian Passages and (c) the closure of the Panama Seaway. Green contours depict the climatological mean stream function for* ***Plio*** *(contour interval: 2 Sv).*

2.5 East Asian summer monsoon

In this section, we investigate the responses of EASM to seaway and CO_2 changes. Fig. 2.10 shows the JJA mean responses of sea level pressure (SLP). While the surface cooling due to decreasing CO_2 is globally ubiquitous (not shown), an enhanced land-ocean SLP contrast between the Pacific and East Asia is simulated (Fig. 2.10a). There is a large SLP decrease of about 1.2 hPa over East China (red box in Fig. 2.10). The SLP over the Tibetan Plateau decreases by ∼3.6 hPa, while there is a weaker positive SLP response over the west Pacific (Fig. 2.10a). In contrast, the restriction of the Indonesian Passages and the Panama Seaway reduces the land–ocean SLP contrast (Fig. 2.10b,c). The seaway changes increase SLP over east China by ∼0.4 hPa and ∼0.6 hPa (Red boxes in Fig. 2.10b,c). The impacts of seaway changes on the west Pacific is modest.

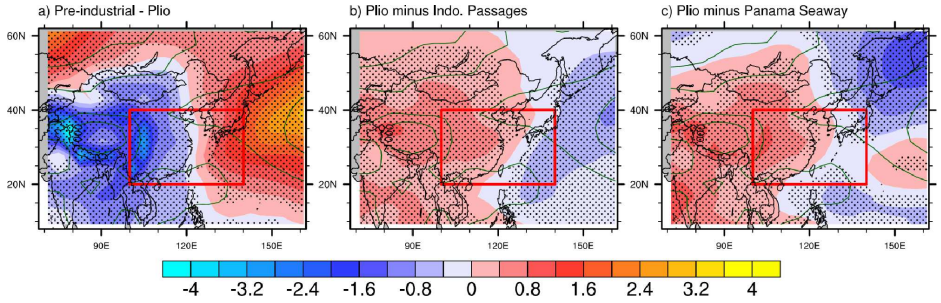

Figure 2.10: *Responses (shading) of JJA mean sea level pressure (unit: hPa) to (a) decreasing CO_2, (b) the constriction of the Indonesian Passages and (c) the closure of the Panama Seaway. Green contours depict the JJA mean SLP for* ***Plio****. Red boxes indicate the range of East Asian monsoon (20°N–40°N, 100°E–140°E).*

Following *Yang et al.* (2002), we define the intensities of EASM as the JJA mean 850 hPa meridional wind averaged over 20°N–40°N and 100°E–140°E (Red boxes in Fig. 2.11). Consistent with the SLP response to lower CO_2, enhanced land–ocean thermal contrast strengthens

the EASM from ∼1.1 m/s in **Plio** to ∼1.65 m/s in **Pre-industrial** (Fig. 2.11b). As opposed to the impact of lower CO_2, the constriction of Indonesian Passages and the Panama Seaway weakens the EASMI to a lesser extent, by ∼0.2 m/s and ∼0.3 m/s, respectively (Fig. 2.11c, d). The SLP response is the dominant driver for the EASM response to seaway changes.

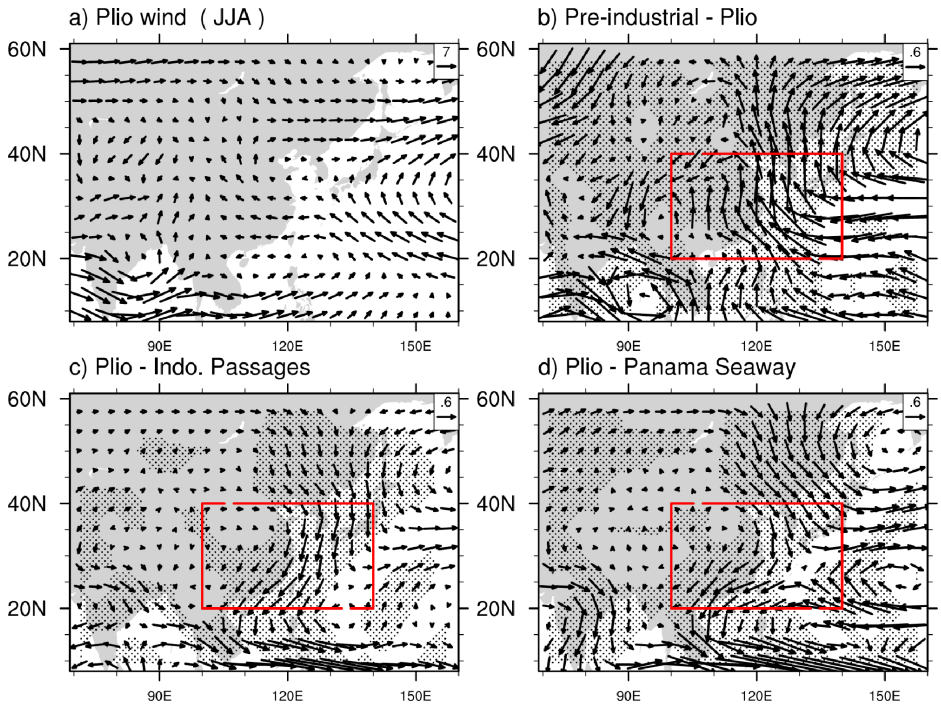

Figure 2.11: *Climatological JJA mean 850 hPa winds for (a)* ***Plio****, and its responses to (b) decreasing CO_2, (c) the constriction of the Indonesian Passages and (d) the closure of the Panama Seaway. Red boxes indicate the range of EASM (20°N-40°N, 100°E-140°E). Wind vector scales (Unit: m/s) are shown in the upper right corner of each panel. Stippling indicates the differences for meridional wind are significant at the 95% confidence level using Student's t-test.*

The impact of lower CO_2 on modulating the precipitation is stronger than that of seaway changes. Despite the enhanced EASM in **Pre-industrial**, the JJA mean precipitation averaged over the monsoon region decreases to 5.78 mm/day in **Pre-industrial**, in comparison to 6.20 mm/day in **Plio**. There is a large decrease of precipitation over the west Pacific (20°N-40°N, 130°E-150°E) amounting to 1.0 mm/day. The precipitation response to lower CO_2 over east China is a dipole pattern, with wetter condition in the north and drought in the north (Fig 2.12a). Both seaway changes induce contradictory precipitation response between east China and the west Pacific (Fig. 2.12b,c). The precipitation over land decreases while increases over the ocean. The overall JJA mean precipitation over the monsoon region slightly reduces by 0.13 mm/day and 0.01 mm/day, in response to the constriction of the Indonesian Passages and the Panama Seaway. The reduced precipitation response over land is associated with the weakened EASMI (Fig. 2.11c,d).

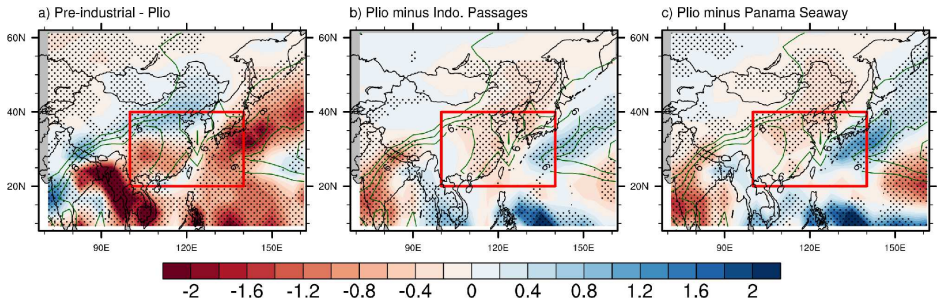

Figure 2.12: *Responses (shading) of JJA mean precipitation (unit: mm/day) to (a) decreasing CO_2, (b) the constriction of the Indonesian Passages and (c) the closure of the Panama Seaway. Contours depict the JJA mean precipitation for* ***Plio****. Red box indicates the range of EASM (20°N–40°N, 100°E–140°E). Stippling indicates the differences for precipitation are significant at the 95% confidence level using Student's t-test.*

2.5.1 Possible mechanisms for the precipitation change

In order to account for the precipitation response to CO_2 and seaway changes, water vapor budgets are analyzed with the following decomposition by *Huang et al.* (2013). The precipitation is decomposed into

$$\Delta P \sim (\overline{\omega} \cdot q + \omega \cdot \overline{q}) \tag{2.3}$$

where P, ω and q are the precipitation, atmospheric vertical velocity (measured as the Lagrangian pressure tendency) and surface specific humidity, respectively. The overbar and Δ represent the **Plio** JJA climatology and responses to CO_2 and seaway changes. The two terms on the right hand side represent the thermodynamic and dynamic component, respectively. The positive vertical velocity represents ascending motion and vice versa. The underlying assumption for Eq. 2.3 is that the precipitation is produced by air that is transported from the boundary layer up to the mid-troposphere, where the water vapor condenses to become precipitation. This decomposition enables to separate the relative importance of the thermodynamic and dynamic contribution to precipitation response. The decomposition results are shown in Fig. 2.13. The water vapor budget (Fig. 2.13g-i) generally reproduces the responses of precipitation to CO_2 and seaway changes, in comparison to Fig. 2.12. The local contribution of thermodynamic component (Fig. 2.13a-c) is weaker compared to that of the dynamic component (Fig. 2.13d-f). Lower CO_2 in **Pre-industrial** largely reduces the thermodynamic contributions by 5.62 Pa/day to precipitation averaged over monsoon region (black box in Fig. 2.13a). Vertical profile of the corresponding specific humidity suggests that the response is robust and consistent throughout the troposphere to 300 hPa (Fig. 2.14a,c). The restriction of the Indonesian Passages and Panama Seaway slightly increases the water vapor content, and thermodynamic contribution by 0.45 Pa/day (Fig. 2.13b) and 1.20 Pa/day (Fig. 2.13c), respectively. A Student's t-test shows that the response is statistically significant over most of the monsoon region (stippling in Fig. 2.13b,c), albeit much weaker change compared to that of lower CO_2. The dynamic component illustrates stronger local contribution to precipitation (Fig. 2.13d-f). Lower CO_2 generally enhances the precipitation associated with the vertical pressure velocity over East China, while weakens the dynamic contribution in the west Pacific.

However, the averaged contribution over the monsoon region amounts to ∼0.38 Pa/day. It is much weaker than the thermodynamic component, which is mainly due to the compensation within the monsoon region. The vertical profile of the vertical velocity suggests that the lower troposphere is more sensitive to decreased CO_2 in **Pre-industrial** (Fig 2.14b,d). The constriction of both seaways weakens the ascending motion over East China and strengthens over west Pacific. The averaged contributions of dynamic component over monsoon region amount to -2.08 Pa/day and -0.51 Pa/day, respectively. Using a Student's t-test, we find that the significance is not as widely distributed as that of specific humidity, albeit the much stronger contribution of the dynamic component.

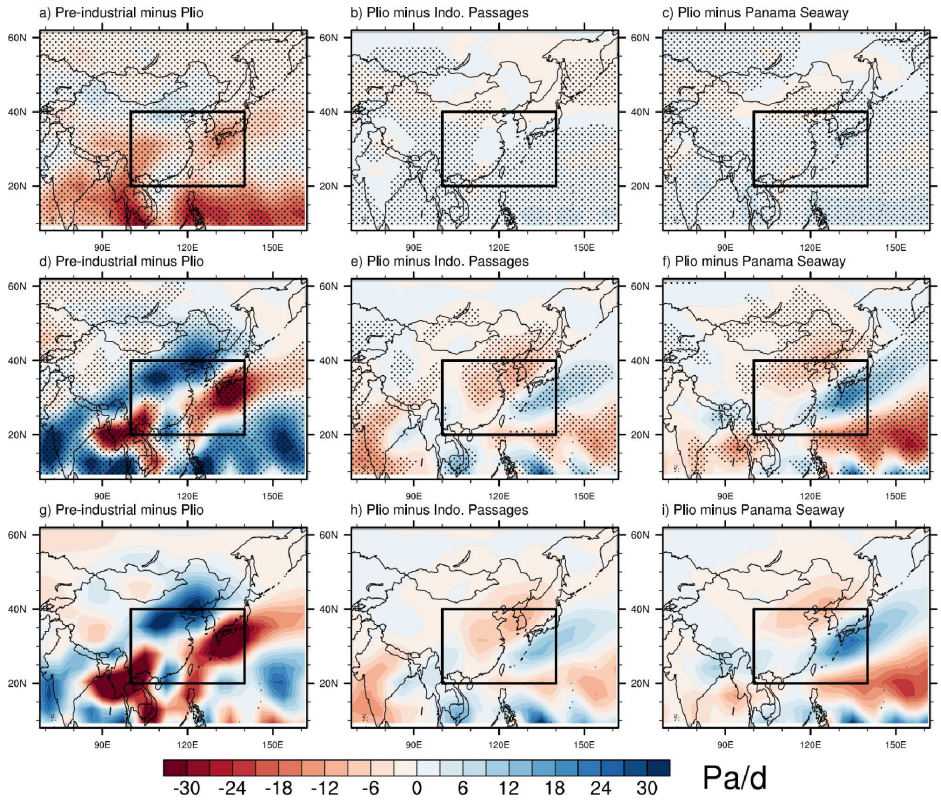

Figure 2.13: *Decomposition of precipitation change as determined from the water vapor budget. Refer to the text for more details. (a) thermodynamic component in response to lower CO_2, (b) the constriction of the Indonesian Passages and (c) the closure of the Panama Seaway. Stippling indicates the differences for surface specific humidity are significant at the 95% confidence level using Student's t-test. (d)-(f) same as in (a)-(c) but for dynamic component. Stippling indicates the differences for vertical velocity are significant at the 95% confidence level using Student's t-test. (g)-(i) summation of thermodynamic and dynamic component. The unit is Pa/day.*

2.6 Summary and discussion

This study investigates the KCM sensitivity to changes in the atmospheric CO_2 concentration, the Indonesian Passages and the Panama Seaway on the large-scale features of the Pliocene climate. In particular, we have compared the model sensitivity with the Pliocene SST reconstructions and EASM in a set of four sensitivity simulations with the KCM, which differ in

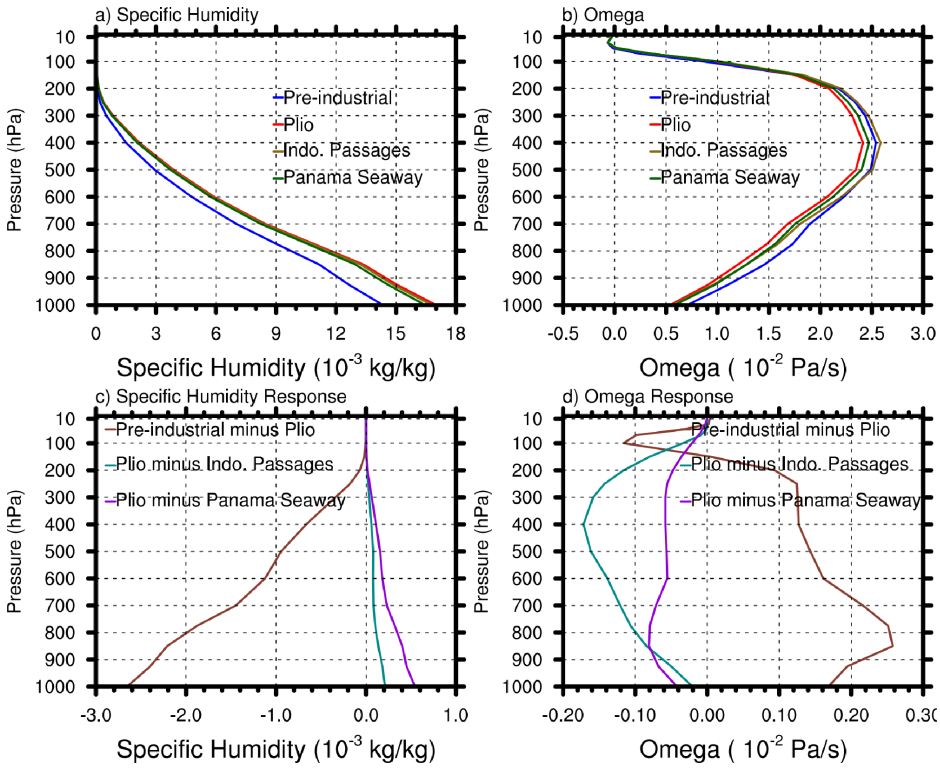

Figure 2.14: *Vertical profile of JJA mean (a) specific humidity and (b) vertical pressure velocity averaged over the monsoon region (20°N–40°N, 100°E–140°E). Vertical profile of response of JJA mean (c) specific humidity and (d) vertical pressure velocity over the monsoon region to CO_2 and seaway changes.*

the geometry of atmospheric CO_2 concentration and the aforementioned passages. We studied the effect of decreasing CO_2-concentration, the restriction of the Indonesian Passages and the closure of the Panama Seaway individually.

Model results show that global mean surface temperature anomalies are dominated by the atmospheric CO_2 concentration. Decreasing CO_2 cools global mean SST and 2m-air-temperature by 2.33°C and 3.12 K, respectively (Table 2.3), which is consistent with surface temperature change (∼2-3 K), estimated from the proxies during the Pliocene. In comparison to the results from Pliocene Model Intercomparison Project (PlioMIP), the simulated 2m-air-temperautre difference between **Pre-industrial** and **Plio** is within the range (∼1.86-3.60 K) of the PlioMIP ensemble mean (*Haywood et al.*, 2013). The constriction of Indonesian Passages and the Panama Seaway warms the global mean 2m-air-temperature barely, which amounts to ∼0.16 K and ∼0.32 K, respectively. Additionally, we observe a significantly increased ice sheet accumulation rate by ∼44% at low CO_2 in **Pre-industrial** compared to **Plio**. In contrast, the constriction of seaway changes slightly slows down the ice sheet accumulation by ∼7.2% and ∼9.1%. It is the melting of ice sheet associated with surface temperature that dominates the glaciation over Greenland in the KCM. Our results support the notion by *Lunt et al.* (2008) that the Northern Hemisphere glaciation during the late Pliocene is controlled by the decline of atmospheric CO_2. The influences of seaway changes, however, are of minor importance.

Although the simulated the global mean surface temperature change between **Plio** and

Pre-industrial agrees reasonably well with the proxies, large model-data discrepancies exist in multiple regions. A comparison with proxy data shows that the model sensitivity agrees well with the SST changes in the southern oceans (Fig. 2.6); however, it substantially underestimate the polar amplification by up to 9°C in the Northern Hemisphere, especially over the North Atlantic and Arctic region (Fig. 2.6). Additionally, the simulated low-latitude temperature responses to CO_2 are uniform in signs, in contrast to diverse responses estimated from proxies over the Caribbean Sea, Arabian Sea and the South China Sea (Fig. 2.6). So far, no climate models could capture the strong polar amplification, or the diverse SST response in the tropics suggested by the proxies during the Pliocene (*Dowsett et al.*, 2012). The reasons may be threefold. First, this suggests the necessity for improved boundary conditions for the Pliocene. Several possible tectonic changes, such as retreated Antarctic ice sheet, a closed Bering Strait and/or a deeper Greenland-Scotland-Ridge are not included in our study (*Hill*, 2015; *Hill et al.*, 2017; *Otto-Bliesner et al.*, 2017. Second, the dicrepancy indicates the weakness and limitations, such as missing and/or weak climate feedbacks of the coupled climate model. For instance, *Burls and Fedorov* (2014) further highlight the importance of an reduced meridional gradient of the cloud albedo in maintaining weak the zonal and meridional temperature gradient. Additionally, better representation of climate feedbacks over high latitudes, such as the water vapor and sea ice feedback, in the coupled models may be underestimated. We note that there is large model bias of the KCM in the North Atlantic. *Park et al.* (2016) shows that correcting this model bias greatly enhances the simulated mean state and decadal variability in this region. Third, this discrepancy also highlights the need for improved proxy interpretation (*Schneider et al.*, 2010) and reduced uncertainties in temperature estimates from geological proxies (*Haywood et al.*, 2013). For instance, *Stewart et al.* (2004) shows that well-preserved foraminifera reveal lower tropical SSTs than previously stated. A proxy-proxy comparison over the Benguela upwelling region suggests that the Mg/Ca and alkenone SST proxies are strongly skewed toward cold and warm seasons, respectively (*Leduc et al.*, 2014).

The model sensitivity of large-scale ocean and atmosphere circulation is also examined. In the equatorial region, lower CO_2 in **Pre-industrial** induces a westward shift of the Pacific Walker circulation, while the restriction of two seaways shifts the Walker cell eastward, in comparison to **Plio**. The intensity of the Pacific Walker cell remains relatively stable (Fig. 2.7). In response to two seaway changes, strengthened Hadley circulation enhances the subsidence in the subtropics and reduces the precipitation over the Sahara desert, east and southwest Africa, which is consistent with pollen-based precipitation data (*DeMenocal*, 2004; *Dupont et al.*, 2005). As for **Pre-industrial**, the effect of reduced water vapor content associated with low CO_2 overwhelms that of weaker subsidence, which amplifies the drought in the subtropics (Fig. 2.4). Despite that the restriction of seaways largely influences the horizontal transport of salinity and heat, the AMOC is relatively stable across all simulations. The closure of the Panama Seaway strengthens the AMOC by ∼2 Sv, which is within the range of PlioMIP results (*Zhang et al.*, 2012b). The impacts of constraining Indonesian Passages and lower CO_2 amount to ∼0.3 Sv and 0.1 Sv. Our result does not support the hypothesis by *Karas et al.* (2017), in which they suggest the restricted Indonesian Passages enhances the AMOC. Relatively modest moisture and heat transport associated with meridional ocean and atmosphere circulation accounts for the rather weak climate responses to CO_2 and seaway changes in the KCM. Our result is consistent with the PlioMIP model ensemble (*Haywood et al.*, 2013).

The EASM response to CO_2 and seaway changes is investigated. Lower CO_2 in **Pre-industrial** strengthens the EASMI by 0.56 m/s, in relative to **Plio**. This is in contrast to the

results of PlioMIP (Table 2.4). Seven out of eight PlioMIP members simulate weaker EASMI in pre-industrial experiment by a range from 0.12 m/s to 1.2 m/s, and only one stronger EASMI in pre-industrial experiment by 0.30 m/s, in composition to mid-Pliocene simulation (*Zhang et al.*, 2013a). JJA mean precipitation over the monsoon region decreases from 6.20 mm/day in **Plio** to 5.78 mm/day in **Pre-industrial**, albeit stronger EASM in **Pre-industrial**. The simulated precipitation response is larger than ensemble mean of PlioMIP amounting to 0.25 mm/day, but within the range from -0.51 mm/day to 0.75 mm/day among individual models. The simulated response to lower CO_2 is consistent with the proxies (*Ding et al.*, 2001; *Wan et al.*, 2007), which suggests a wetter and warmer monsoon region during the Pliocene. The constraint of two tropical seaways both weakens the EASMI (Fig. 2.11). The restriction of Indonesian Passages and the Panama Seaway weakens the EASMI by 0.28 m/s and 0.20 m/s, respectively. Accordingly, JJA mean precipitation over the monsoon region in response to both seaway changes decreases by 0.11 mm/day and 0.01 mm/day, respectively.

Model	Response of EASMI (m/s)	Response of precipitation (mm/day)
CCSM4	−0.12	−0.05
COSMOS	+0.30	+0.77
HadCM3	−1.20	−0.83
IPSLCM5A	−0.22	−0.47
MIROC4m	−1.07	−0.47
ModelE2-R	−0.43	−0.71
MRI-CGCM2.3	−0.36	−0.24
NorESM-L	−0.31	−0.24
KCM	+0.56	−0.42

Table 2.4: *The response (defined as the difference between Pre-indurial and Plio) of the intensity of East Asian summer monsoon (EASMI) and JJA mean precipiation over the monsoon region (20°N-40°N, 100°E-140°E) in the KCM and the PlioMIP experiments (Zhang et al., 2013a).*

In order to account for the precipitation responses, a water vapor budget analysis is conducted by decomposing the precipitation into thermodynamic and dynamic component. In general, the local contribution of dynamic component to precipitation is stronger than the thermodynamic component. The water vapor budget generally agrees well with the precipitation response. Reduced precipitation over monsoon region in **Pre-industrial** is mainly attributed to thermodynamic component (-5.62 Pa/day). The dynamic component amounting to ∼0.38 Pa/day compensates the reduced precipitation slightly. The precipitation response to the restricted Indonesian Passages is owing to the compensation of the thermodynamic (0.45 Pa/day) and dynamic component (-2.08 Pa/day). The impact of closed Panama Seaway is rather weak over the monsoon region, which is consistent with ∼0.01 mm/day precipitation change.

Multiple geological evidences for temperature and humidity ranging from ∼3.3 to 3.0 Ma B.P. suggest cooling and drying monsoon region since the mid-Pliocene (*Ma et al.*, 2005; *Wu et al.*, 2007, *Wu et al.*, 2011; *Jiang and Ding*, 2008; *Cai et al.*, 2012). Our result indicates that the EASM response is largely attributed to the declining CO_2. The impact of seaway changes is much weaker, in comparison to low CO_2. On the other hand, model results do not support the hypothesis by *Nie et al.* (2014), in which they proposed that the final closure of the Panama Seaway may have intensified the EASM from 4.8 to 2.7 Ma B.P.. We find that

the closed Panama Seaway barely weakens the EASM. Instead, declining CO_2 could explain the cooling and wetting trend over the proxy site. Additionally, the impacts of orography changes over the Himalayan Mountains and the Tibetan Plateau may be of greater importance (*An et al.*, 2001; *Zhang et al.*, 2012a).

Supplemental figures

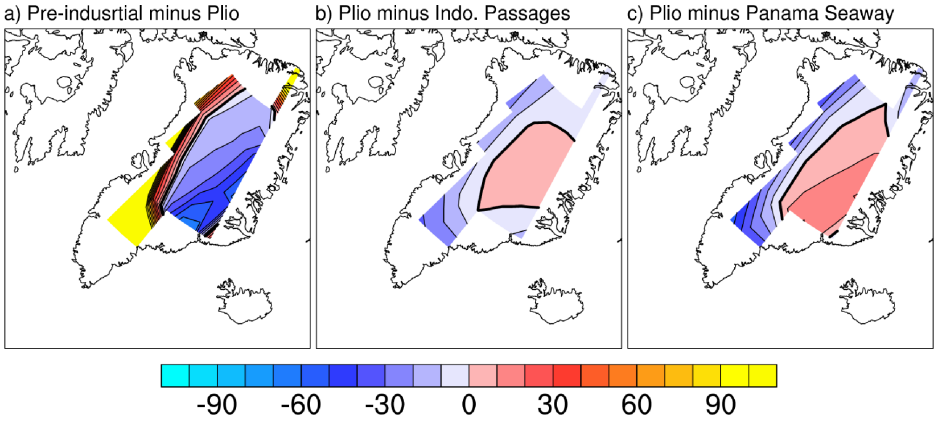

Figure S2.1: *Annual mean ice sheet accumulation rate (mm/yr) in response to (a) decreasing CO_2, (b) the constriction of the Indonesian Passages and (c) the closure of the Panama Seaway.*

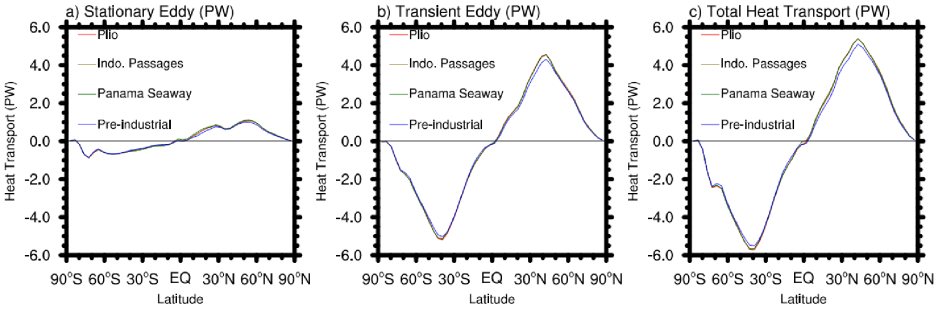

Figure S2.2: *Atmospheric heat transport (Unit: PW) by (a) stationary eddies, (b) transient eddies and (c) their summation for four experiments.*

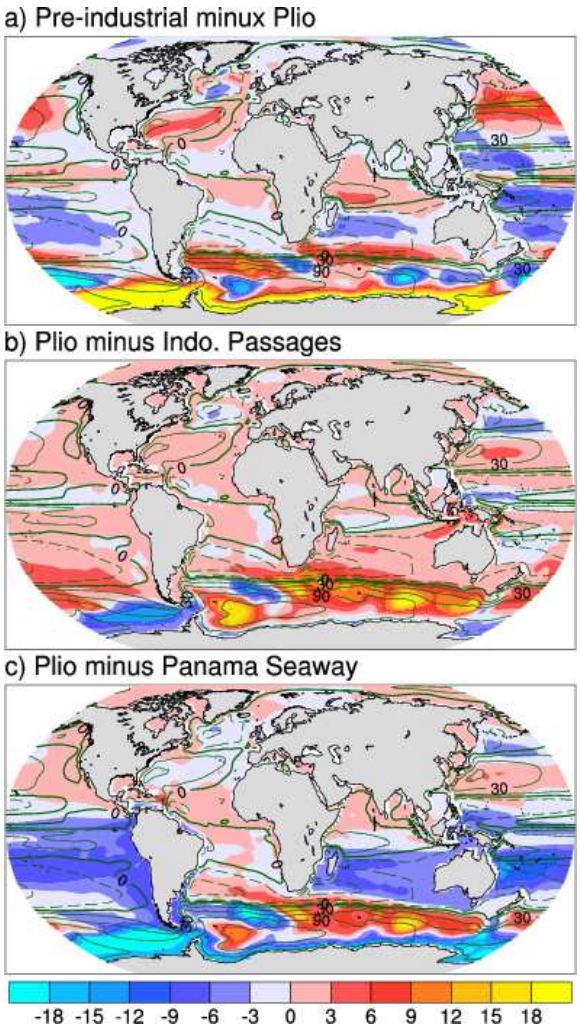

Figure S2.3: *Barotropic stream function (Unit: Sv) responses to (a) decreasing CO_2, (b) the constriction of the Indonesian Passages and (c) the closure of the Panama Seaway. Dark green contours depict the climatological mean stream function for* ***Plio****.*

Chapter 3

Influence of Seaway Changes on Tropical Pacific Climate: Mean State, Annual Cycle, ENSO, and their Interactions

This chapter is a reprint of paper "Influence of Seaway Changes during the Pliocene on Tropical Pacific Climate in the Kiel Climate Model: Mean State, Annual Cycle, ENSO, and their Interactions" published in Climate Dynamics

Citation: Song, Z., Latif, M., Park, W., Krebs-Kanzow, U., and Schneider, B. (2017). Influence of seaway changes during the Pliocene on tropical Pacific climate in the Kiel climate model: mean state, annual cycle, ENSO, and their interactions. Climate Dynamics, 48(11-12), 3725-3740. doi:10.1007/s00382-016-3298-x.

Abstract

The El Niño/Southern Oscillation (ENSO) is the leading mode of tropical Pacific interannual variability in the present-day climate. Available proxy evidence suggests that ENSO also existed during past climates, for example during the Pliocene extending from about 5.3 million to about 2.6 million years B.P.. Here we investigate the influences of the Panama Seaway closing and Indonesian Passages narrowing, and also of atmospheric carbon dioxide (CO_2) on the tropical Pacific mean climate and annual cycle, and their combined impact on ENSO during the Pliocene. To this end the Kiel Climate Model (KCM), a global climate model, is employed to study the influences of the changing geometry and CO_2-concentration. We find that ENSO is sensitive to the closing of the Panama Seaway, with ENSO amplitude being reduced by about 15% - 20%. The narrowing of the Indonesian Passages enhances ENSO strength but only by about 6%. ENSO period changes are modest and the spectral ENSO peak stays rather broad.

Annual cycle changes are more prominent. An intensification of the annual cycle by about 50% is simulated in response to the closing of the Panama Seaway, which is largely attributed to the strengthening of meridional wind stress. In comparison to the closing of the Panama Seaway, the narrowing of the Indonesian Passages only drives relatively weak changes in the annual cycle. A robust relationship is found such that ENSO amplitude strengthens when the annual cycle amplitude weakens.

3.1 Introduction

Proxy data suggests the El Niño/Southern Oscillation (ENSO), the leading mode of present day tropical interannual variability, was active across a wide variety of past climate states as far back as the late Cretaceous, Eocene, Miocene, Pliocene, Pleistocene and the Holocene (*Davies et al.*, 2012; *Huber and Caballero*, 2003; *Galeotti et al.*, 2010; *Watanabe et al.*, 2011; *Scroxton et al.*, 2011; *Cobb et al.*, 2003; *McGregor et al.*, 2013). The Pliocene was the last period that featured an atmospheric CO_2-concentration which was similar to the present-day values, with concentrations amounting to about 405 ppm (*Haywood et al.*, 2011). Paleogeochemical proxies indicate that sea surface temperature (SST) within the tropical warm pool regions may have changed little over the last 3 to 5 million years (*Wara et al.*, 2005; *Pagani et al.*, 2010. On the other hand, the cold tongue in the eastern equatorial Pacific was about 4-5 °C warmer than today (*Wara et al.*, 2005; *Fedorov et al.*, 2006) and SSTs in the subtropical upwelling zones were substantially warmer than the present (*Brierley et al.*, 2009). The proxy records suggest that much reduced zonal and meridonal SST gradients existed in the early Pliocene (*Wara et al.*, 2005; *Fedorov et al.*, 2013). Although the SST gradient strengthened as time progressed, it was still considerably reduced in the mid-Pliocene, which is thought to have had significant consequences for the tropical Pacific climate at that time, especially for ENSO.

Wara et al. (2005) referred the much warmer cold tongue in the eastern equatorial Pacific, which considerably reduces the zonal SST gradient, to as "permanent El Niño-like" conditions. *Haywood et al.* (2007) and *Fedorov et al.* (2010) report weak extant ENSO variations in coupled climate models. In contrast, proxy data and other modeling results suggest persistent signifi-

cant ENSO variability. Proxy evidence suggesting persistent ENSO activity during the Pliocene has been provided by *Watanabe et al.* (2011) and *Scroxton et al.* (2011). Climate model simulations from the Pliocene Model Intercomparison Project (PlioMIP) yield ENSO variability simulated under reconstructed mid-Pliocene conditions (*Haywood et al.*, 2011; *Dowsett et al.*, 2012; *Brierley*, 2015). *Manucharyan et al.* (2014) simulate a robust ENSO under very different climatological zonal SST gradients. They manipulate the east-west equatorial Pacific SST gradient decreasing it from 6.0°C to 1.4°C, while the amplitude of ENSO decreases by only 30% - 40%. How do these so called permanent El Niño-like tropical Pacific mean states maintain a "healthy" ENSO?

The opening and closing of oceanic gateways has a profound influence on the distribution of fresh water, nutrients, and energy in the global ocean, and is thus a major factor in driving past global environmental and climate changes. Here we investigate by means of a global climate model, the Kiel Climate Model (KCM, *Park et al.*, 2009), the influences of the Panama Seaway closing and Indonesian Passages narrowing during the Pliocene on tropical Pacific mean climate, annual cycle and interannual variability. A particular focus is ENSO which, in simple nonlinear models, can be understood as the first (Hopf) bifurcation (*Jin et al.*, 1996), moving the system from a stable to an oscillatory regime, when increasing the strength of ocean–atmosphere coupling which in turn is related to the zonal SST gradient. The tropical Pacific is special among the tropical oceans exhibiting a strong zonal asymmetry in its upper ocean thermal structure, which is clearly seen in the equatorial SST. In the western warm pool region SSTs amount to up to 29°C, in the eastern cold tongue region SSTs are typically up to 10°C colder. It is this zonal asymmetry that enables ENSO. In the central-eastern equatorial Pacific, variations in thermocline depth modulate SST through vertical advection of temperature anomalies by the mean upwelling – a process referred to as "thermocline feedback" - thereby communicating subsurface temperature signals to the surface. This introduces changes in the zonal SST gradient along the equator, which in turn interacts with the easterly trade winds (*Bjerknes*, 1969), giving rise to a positive feedback. In conjunction with delayed negative feedbacks by the wind-driven ocean circulation and oceanic waves, these processes are at the heart of the ENSO mechanism.

How the character of ENSO changes when the tropical Pacific mean state changes is an important question. To assess the overall stability of ENSO in state-of-the-art climate models, *Jin et al.* (2006) proposed the Bjerknes stability (BJ) Index. This index has been used to investigate a large range of ENSO behaviors in and among coupled general circulation models (CGCMs) under a variety of background ocean-atmosphere mean states (e.g.; *Kim and Jin*, 2011a; *Kim and Jin*, 2011b), which aided the understanding of ENSO dynamics in climate models. The BJ index has also been applied to observations to understand differences between the equatorial Pacific and equatorial Atlantic interannual variability and shifts in ENSO behavior during the most recent decades (*Lübbecke et al.*, 2013; *Lübbecke et al.*, 2014)

Another important factor in determining the character of ENSO is the annual cycle, which is readily seen, for example, by the seasonal phase locking of ENSO with strongest SST anomalies in boreal winter and weakest in boreal spring. The annual cycle involves the development and decay of the eastern equatorial Pacific cold tongue, which is forced by the solar radiation in the first place. At the equator, however, the solar radiation exhibits a semiannual cycle. Yet the SST in the eastern and central Pacific depicts a pronounced annual cycle. The northerly position of the Intertropical Convergence Zone (ITCZ), owing to the hemispheric asymmetry of land-sea

distribution, generates a weak annual cycle of surface wind forcing at the equator (*Li et al.*, 1996). One important mechanism in the equatorial annual cycle is the propagation of annual cycle signal from the South America coast through the Wind-Evaporation-SST (WES) feedback and the subsequent coupled ocean-atmosphere disturbance, as first pointed out by *Liu and Xie* (1994) and *Liu* (1996). Additionally, coupled air-sea feedbacks intensify the wind forcing by invoking a near-annual frequency mode that propagates westward (*Li et al.*, 1996; *Xie*, 1996). Through the mechanism of frequency entrainment, the tropical annual cycle interacts with and tends to damp ENSO (*Liu*, 2002; *Chang et al.*, 1994).

In this study, we describe the sensitivity of the KCM's mean state, annual cycle and ENSO to external changes during the Pliocene, forced by changes in ocean geometry and atmospheric CO_2, Special attention is given to the influence of the Panama Seaway closing and Indonesian Passages narrowing, and to the interaction between the annual cycle and ENSO. The structure of this paper is as follows. In section 3.2, we describe the coupled model and the experimental design. Mean state changes are presented in section 3.3. The response of the SST annual cycle is addressed in section 3.4. In section 3.5, ENSO stability is discussed on the basis of the BJ Index. We conclude this paper with a brief summary and a discussion of the main results in section 3.6.

3.2 Coupled model, experimental setup, and methods

3.2.1 Coupled model and experimental setup

We use the Kiel Climate Model (KCM, *Park et al.*, 2009). The atmosphere model is ECHAM5 (*Roeckner et al.*, 2003) which is integrated with T31 (3.75° x 3.75°) horizontal resolution and 19 vertical levels up to 10 hPa. The ocean-sea ice component is NEMO (*Madec*, 2008) on a 2° Mercator mesh, with 31 vertical levels. The meridional resolution increases towards lower latitudes, with 0.5° in the equatorial region. The two components are coupled with the OASIS3 coupler (*Valcke*, 2006). No form of flux correction or anomaly coupling is employed. The KCM has been applied in studies addressing past, present-day and future climate. A list of references of published studies employing the KCM can be obtained from http://www.geomar.de/en/research/fb1/fb1-me/research-topics/climate-modelling/kcms/.

In terms of gross indices, ENSO is simulated reasonably well by the KCM, as described in *Park et al.* (2009) and more recently, in *Latif et al.* (2015). The ENSO response of the KCM to strongly increasing atmospheric CO_2 has also been described in *Park et al.* (2009) and *Latif et al.* (2015). The tropical Pacific response to increasing greenhouse gas concentrations in other climate models, which participate in the Coupled Model Intercomparsion Project Phase 3 (CMIP3) and Phase 5 (CMIP5), and in the Pliocene Model Intercomparison Project (PlioMIP), has been explored, for example, in *Latif and Keenlyside* (2009), *DiNezio et al.* (2012), *Collins et al.* (2010), *Bellenger et al.* (2014) and *Brierley* (2015). In comparison to those models, the KCM is somewhat special, as it projects strongly increasing ENSO amplitude under global warming conditions (Fig. S3.1, S3.2, S3.3), which is mainly due to strengthened thermocline feedback and enhanced atmospheric sensitivity to SSTA (*Park et al.*, 2009). Further, skewness and kurtosis also increase at higher CO_2 (Fig. S3.4).

A set of eight experiments is conducted (Table 3.1) in order to separate the climate effects

of lowering atmospheric CO_2, narrowing of the Indonesian Passages and closing of the Panama Seaway, which happened during the Pliocene. Experiment names consist of three sequential letters representing different boundary conditions. The first letter indicates CO_2-concentration [Low (286 ppm) and High (405 ppm)], the second letter the Indonesian Passages [Modern or Pliocene geometry (wider and deeper than modern)], and the third letter the Panama Seaway [Modern (closed) or Pliocene geometry (open, with a depth 1200 m)]. For example, LMM represents the experiment with Low-CO_2 and Modern Indonesian Passages and Modern Panama Seaway, and this integration serves as a pre-industrial control simulation. LMM is integrated for 2,000 years starting from the Levitus climatology of temperature and salinity. Experiment HMM differs from experiment LMM only in the CO_2-concentration which is higher. HMM serves as control run for the high CO_2 experiments. The other six experiments are initialized with the output from either LMM or HMM and integrated for 800 years. The last 300 years from each of the integrations are used in the subsequent analysis.

The deeper and wider geometry of the Indonesian Passages during the Early Pliocene follows the assumption of *Cane and Molnar* (2001): the passages between Sulawesi and New Guinea are 1,000 m deeper relative to the modern bathymetry, the northern coast of New Guinea is located 2° south due to the missing of the northern part, and the passage between Timor and Australia is also wider and deeper by removing part of Timor. Effects of such tectonic changes have been shown to cause the acidification off Australia and a series of complex Indo-Pacific climate changes (*Krebs et al.*, 2011). An open Panama Seaway is accomplished in the model by replacing four land grid cells by ocean grid cells between North and South America located at approximately 8°N. We employ a depth of 1,200 m representing a deep Panama Seaway to simulate the early stage of the shoaling process.

Experiment name	Atmospheric CO_2		Indonesian Passages		Panama Seaway		Integration model years
LMM	286 ppm	L	Modern	M	Closed	M	2000
LPM	286 ppm	L	Deep/wide	P	Closed	M	800
LMP	286 ppm	L	Modern	M	1200 m	P	800
LPP	286 ppm	L	Deep/wide	P	1200 m	P	800
HMM	405 ppm	H	Modern	M	Closed	M	1000
HPM	405 ppm	H	Deep/wide	P	Closed	M	800
HMP	405 ppm	H	Modern	M	1200 m	P	800
HPP	405 ppm	H	Deep/wide	P	1200 m	P	800

Table 3.1: *Overview of the model simulations analyzed in this paper. Acronyms of the experiments stand for* ***L****ow (****H****igh) atmospheric CO_2-concentration,* ***M****odern (****P****liocene) Indonesian Passages,* ***M****odern (****P****liocene) Panama Seaway for the first, second, and third characters, respectively. HMM and LMM are the "present-day" control simulations with high and low CO_2-concentration, respectively.*

3.2.2 Amplitude equation for the annual cycle

With some modifications and systemic assumptions that filter out interannual variability signals, the governing mixed layer SST anomaly equation for the annual cycle over the equatorial eastern Pacific deduced by *Xie* (1994) is:

$$\frac{\partial T^{'}}{\partial t} = -\left(\bar{u}_0 - c\right)\frac{\partial T^{'}}{\partial x} + \frac{2Q_s}{\rho C_p h} - \left(1+\frac{\eta}{H}\right)\frac{2\bar{Q}_E}{\rho C_p h}\frac{\bar{v}}{|\bar{u}|^2}v^{'} - \varepsilon T^{'} \tag{3.1}$$

where $T^{'}$ is the SST anomaly (relative to the annual-mean SST) in the mixed layer, $\bar{u}_0$ denotes the mean zonal current velocity, c is the phase speed due to a 90° phase difference between the zonal wind stress and SST, and h the depth of the mixed layer. The relative importance between the mean latent heat flux and vertical mixing is measured by the ratio η/H; Q_S and $\bar{Q}_E$ are the perturbation solar radiation and the mean latent heat flux, respectively; $\bar{u}_0$ and $\bar{v}$ are the mean zonal and meridional wind stress, respectively. The constants ρ and C_p denote ocean density and heat capacity of sea water at constant pressure, respectively. ε is the thermal damping timescale. The first three terms on the right hand side indicate westward propagation via air-sea coupling, the surface solar radiation and the latent heat flux depending on changes in the meridional wind stress, respectively. The fourth term is surface radiative cooling. More details about Eq. 3.1 can be found in *Xie* (1994). For the derivation, see *Anderson et al.* (1985) and *Xie et al.* (1989). From Eq. 3.1, the westward propagation of the annual cycle signal is dominant at the equator where the meridional SST gradient vanishes. Meridional advection becomes more important off the equator due to the increasing meridional SST gradient.

An and Choi (2013) multiplied Eq. 3.1 by $T^{'}$ to derive the amplitude tendency equation:

$$\frac{\partial}{\partial t}\left\langle T^{'2}\right\rangle = -\left(\bar{u}_0 - c\right)\frac{\partial}{\partial x}\left\langle T^{'2}\right\rangle + \frac{4}{\rho C_p h}\left\langle Q_s T^{'}\right\rangle - \left(1+\frac{\eta}{H}\right)\frac{4\bar{Q}_E}{\rho C_p h}\frac{\bar{v}}{|\bar{u}|^2}\left\langle v^{'}T^{'}\right\rangle - 2\varepsilon\left\langle T^{'2}\right\rangle \tag{3.2}$$

As seen in Eq. 3.2, the annual cycle of SST in the eastern Pacific is largely controlled by the second and third term on the right hand side. Within a seasonal cycle, the solar forcing is positively correlated to SST (i.e. $\left\langle Q_s T^{'}\right\rangle$ is positive), while the cross-equatorial southerly is negatively correlated to the SST (i.e. $\left\langle v^{'}T^{'}\right\rangle$ is negative, also see Fig.6 in *An and Choi* (2013)). Thus the amplitude of annual cycle is positively correlated to solar forcing ($\frac{\partial}{\partial t}\left\langle T^{'2}\right\rangle \propto \left\langle Q_s T^{'}\right\rangle$) in the second term, latent heat flux ($\frac{\partial}{\partial t}\left\langle T^{'2}\right\rangle \propto \bar{Q}_E \cdot -\left(\left\langle v^{'}T^{'}\right\rangle\right)$), v ($\frac{\partial}{\partial t}\left\langle T^{'2}\right\rangle \propto \bar{v}\cdot -\left(\left\langle v^{'}T^{'}\right\rangle\right)$) in the third term and negatively correlated to the mixed layer depth ($\frac{\partial}{\partial t}\left\langle T^{'2}\right\rangle \propto \frac{1}{h}$) and zonal wind ($\frac{\partial}{\partial t}\left\langle T^{'2}\right\rangle \propto \frac{1}{|\bar{u}|^2}\cdot -\left(\left\langle v^{'}T^{'}\right\rangle\right)$). The mixed layer depth (h) involves both terms; therefore it has somewhat stronger effect on the annual cycle of the SST. Detailed analysis using the output from the numerical experiments will be presented in section 3.4.

3.2.3 Bjerknes stability index

We assess the characteristics of the ENSO mode in our experiments through quantifying the relative strength of positive and negative feedbacks by using the Bjerknes stability index derived by *Jin et al.* (2006) from the linear equation for SST anomalies in the mixed layer [Eq. (1) in

Jin et al., 2006]. The volume average of the linearized SST equation is taken over the upper eastern equatorial Pacific where the SST exhibits its maximum interannual variability.

The resulting equation obtained by applying several approximations is written as:

$$\frac{\partial \langle T \rangle_E}{\partial t} = 2I_{BJ} \langle T \rangle_E + F[h] \tag{3.3}$$

where

$$2I_{BJ} = -\left(\frac{\langle u \rangle_E}{L_x} + \frac{\langle -2y\bar{v} \rangle_E}{L_y^2} + \frac{\langle \bar{w} \rangle_E}{H_m}\right) - \alpha + \mu_a\beta_u \left\langle -\frac{\partial \bar{T}}{\partial x} \right\rangle_E + \mu_a\beta_w \left\langle -\frac{\partial \bar{T}}{\partial z} \right\rangle_E + \mu_a\beta_h \left\langle \frac{H(\bar{w})\bar{w}}{H_m} a_h \right\rangle_E \tag{3.4}$$

and

$$F = \beta_{uh} \left\langle -\frac{\partial \bar{T}}{\partial x} \right\rangle + \left\langle \frac{H(\bar{w})\bar{w}}{H_m} \right\rangle_E a_h \tag{3.5}$$

with $\langle \rangle_E$ denoting the volume average over the eastern equatorial Pacific box. Variables with an overbar indicate climatological means. T, u, v and w represent the SST anomalies, the zonal, meridional and vertical velocity anomalies, respectively; and Q ($\alpha = \frac{\langle Q \rangle}{\langle T \rangle}$) denotes the anomalous net heat flux from the atmosphere into the ocean and diffusive processes. The zonal and meridional extents of the eastern equatorial box are L_x and L_y , y is the distance from the equator. The factor $\frac{-2y}{L_y}$ comes from the assumption that the meridional structure of ENSO-related SST anomalies is Gaussian-like with an e-folding decay scale of L_y. The depth H_m is the effective depth for vertical advection, α the linear estimation of thermal damping and μ_a the zonal wind stress response to SST forcing. β_u, β_w and β_h describe the ocean surface current, the upwelling and thermocline slope to equatorial zonal wind forcing, respectively. β_{uh} is the geostrophic adjustment of zonal currents to the thermocline depth anomalies, a_h the subsurface temperature change response to thermocline depth variations. The step function *H(x)* ensures that only upward vertical motion affects surface temperature. The Bjerknes stability index is denoted by I_{BJ} while F is a phase transition term associated with the recharge/discharge of the heat content. The terms of the BJ Index in Eq. 3.4 describe either negative or positive feedbacks involved to damp or enhance an SST anomaly in the eastern equatorial Pacific. From left to right the first two terms that make negative contributions correspond to dynamical (mean zonal advection and upwelling) and thermal damping, while the last three terms describing positive feedbacks are the zonal advection, Ekman pumping and thermocline feedback. A negative BJ Index is associated with a stable, damped system, and vice versa.

The computation of the BJ Index is sensitive to the region over which the variables are averaged. The longitudinal range of the volume average boxes that are indicated by $\langle \cdot \rangle_E$ and $\langle \cdot \rangle_W$ are defined as 120°E∼180°, 5°S∼5°N and 180°∼80°W, 5°S∼5°N within the mixed layer, respectively. Thus, the Niño-3 region, the area of strongest interannual SST variability (see Fig. 3.6), is accounted for in the eastern volume average box. The vertical range is from the

surface to the bottom of the mixed layer. The mixed layer depth in the model is estimated by a Richardson number-dependent mixing parameterization, with a density threshold of 0.01 kg·m^3. In this study, we employ the depth of the 20°C isotherm (Z20) to represent the thermocline depth. Interannual anomalies are computed by subtracting a mean seasonal cycle from all time-series after detrending them.

3.3 Simulated mean tropical climate

Under preindustrial conditions (LMM: low CO_2, modern oceanic passages), a warm pool with SSTs exceeding 29°C is simulated in the west and a cold tongue in the east, which together allow for strongly zonally asymmetric tropical Pacific SSTs (Fig. 3.1a). The simulated preindustrial SSTs are considerably colder compared to those simulated for the early Pliocene (HPP: high CO_2, wide Indonesian Passages, open Panama Seaway), as shown in Fig. 3.1b. Exceptions are limited regions in the North Pacific and North Atlantic, which depict warmer SSTs under preindustrial conditions. The generally warmer SSTs simulated for the early Pliocene must be due to the combined effects of enhanced atmospheric CO_2 and altered oceanic passages. The open Panama Seaway yields weaker Atlantic Meridional Overturning Circulation (AMOC) and Kuroshio Current (*Maier-Reimer et al.*, 1990), which accounts for the cooler SSTs in parts of the North Atlantic and North Pacific.

This study mainly focuses on the SST changes due to seaway change. Fig. 3.2 shows global SST differences between the different experiments which differ in the geometry of the Indonesian and/or Panama Seaways, or CO_2 concentration. Relative to the deep and wide Indonesian Passages (LPM) run, the pre-industrial control run (LMM) with narrower and shallower Indonesian Passages depicts small surface warming in the Pacific warm pool area and cooling in the eastern Indian Ocean warm pool area, with SST changes amounting to well below 1°C for low atmospheric CO_2 (Fig. 3.2a). The stronger SST response (Fig. 3.2b) to narrowing the Indonesian Passages is probably due to the considerably stronger ocean circulation changes at higher CO_2 (Fig. S3.5). The closed Panama Seaway experiments, independent of the CO_2 concentration (LPM, Fig. 3.2c; HPM, Fig. 3.2d), generally yield stronger SST changes. In the equatorial Pacific, a meridional dipole is observed, which is strongest in the east, with cooling south and warming north of the equator (Fig. 3.2c, d). The Pacific warm pool area becomes warmer, but by less than 1°C. Relatively strong changes are seen in the extratropical oceans. SSTs in the North Pacific and North Atlantic increase by 2°C or by even more in localized regions. The warming in the North Atlantic is due to enhanced northward heat transport associated with a stronger Atlantic Meridional Overturning Circulation (AMOC) (not shown). This is supported by the cooling of the South Atlantic, which together with the North Atlantic warming is a typical signature of AMOC strengthening in climate models (*Latif et al.*, 2004) and referred to as the Interhemispheric Dipole (e.g., *Folland et al.*, 1986). The closed Panama Seaway prevents fresher water being transported from the Pacific into the Atlantic, which eventually enhances the formation of North Atlantic Deep Water (NADW). The influences of the closed Panama Seaway on North Atlantic sector climate and the corresponding mechanisms have been discussed from a multi model perspective in *Zhang et al.* (2012b). The influence of the Panama Seaway closing on the AMOC in the KCM and its potential role in Northern Hemisphere glaciation will be the subject of a forthcoming paper.

When the Indonesian Passages and Panama Seaway are changed together towards modern

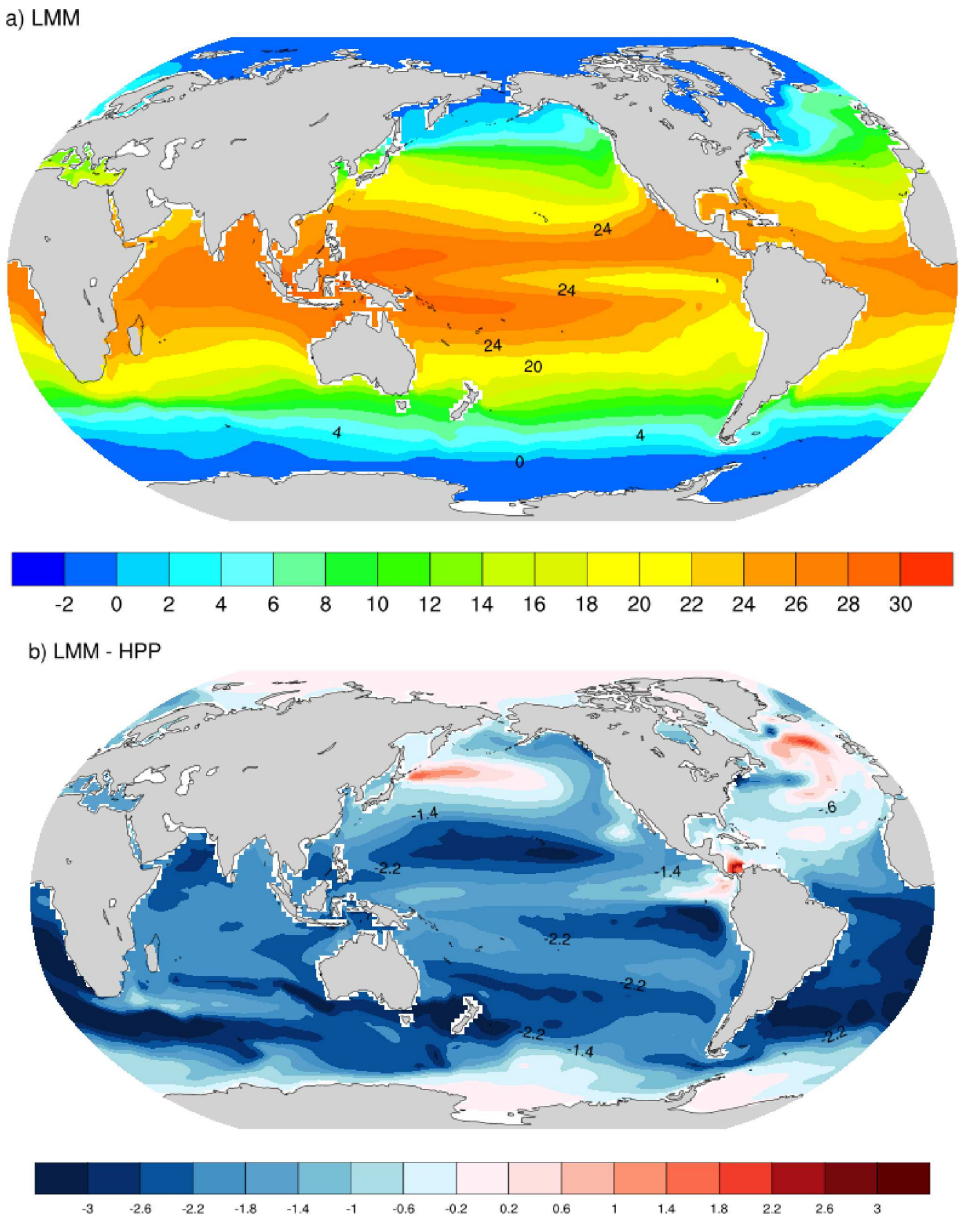

Figure 3.1: *(a) Climatology of SST (°C) in the pre-industrial control simulation LMM (low-CO_2, modern ocean geometry). (b) Difference between LMM and HPP (high-CO_2, wide and deep Indonesian Passages and open Panama Seaway). 300 years from each experiment were used in the calculations. Experiment HPP represents early Pliocene conditions.*

conditions (Fig. 3.2e, f), the SST responses are very similar to those of the Panama Seaway-closing experiment, indicating much stronger influences of the Panama Seaway change. In the equatorial Pacific, the warming is slightly larger when both passages are changed simultaneously in the KCM. Not much dependence on the CO_2 concentration is found; the SST patterns are quite similar in the low- (Fig. 3.2, left panels) and high-CO_2 (Fig. 3.2, right panels) simulations.

We next analyze thermocline depth in the tropics (30°N-30°S), as represented by the depth of the 20°C isotherm (Z20, Fig. 3.3). The field of mean Z20 (Fig. 3.3b) simulated by the KCM

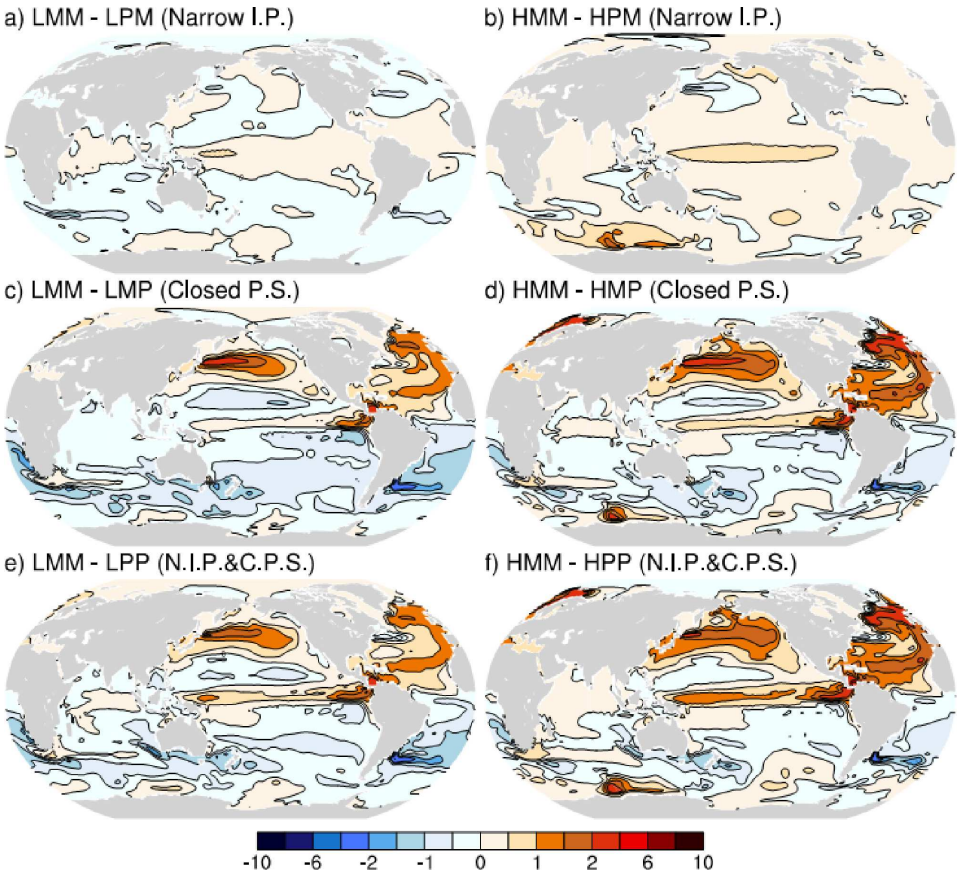

Figure 3.2: *SST (°C) responses to changes in topography with respect to the control simulation LMM employing low CO_2-concentration (left panels; a, c, e) and HMM employing high CO_2-concentration (right panels; b, d, h), due to (a, b) the narrowing of the Indonesian Passages, (c, d) closing of the Panama Seaway, and (e, f) due to both changes in ocean geometry. The contour intervals are 0.5°C in the range of -2°C to 2°C and 2°C in the range of 2°C to 10°C, respectively.*

under present-day conditions is compared to observations in *Park et al.* (2009) (see Fig. 5 therein). The narrower Indonesian Passages mainly shoals the Z20 in the Indonesian Throughflow region (Fig. 3.3c, d) and deepens the thermocline elsewhere, with largest deepening in the subtropics of all three tropical oceans. A generally stronger Z20-response is observed when the Panama Seaway is closed. Shallower Z20 is simulated in the tropical Indian Ocean, especially in its southern part, mainly due to constrained heat transport associated with the Indonesian Throughflow narrowing (Fig. 3.3c, d). In the tropical Pacific, Z20 shoals north of the equator and deepens south of the equator owing to decreased mixing of Pacific and Atlantic waters. In the tropical Atlantic, on the other hand, the Z20 deepens north of the equator but shoals to the south owing to enhanced northward heat transport associated with stronger AMOC. The strongest change in Z20 is observed in the North Atlantic depicting much deeper mixed layer depths.

Mean-state changes are also prominent in other oceanic and atmospheric variables (Fig. 3.4). Fig. 3.4a displays the meridionally averaged (5°S-5°N) annual-mean equatorial Pacific SSTs. All three runs with geographical changes towards modern conditions yield warmer equatorial Pacific SSTs, with the experiment HMM (high CO_2, modern oceanic passages) providing

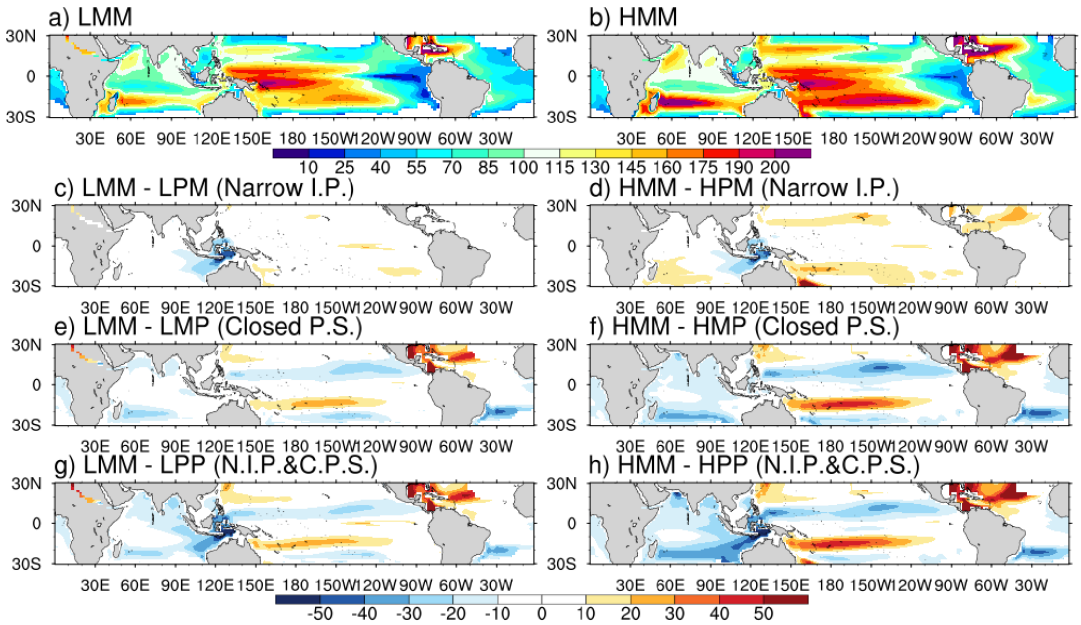

Figure 3.3: *Annual-mean depth (m) of the 20°C isotherm (Z20) in the control experiment (a) LMM and (b) HMM (contour interval: 15 m). (c-h) Z20-changes in the simulations with low/high-CO_2 and different ocean geometry with respect to LMM/HMM (contour interval: 10 m).*

the warmest equatorial Pacific SSTs. Warmer temperatures generally go along with weaker easterly zonal wind stress over the eastern and central equatorial Pacific (Fig. 3.4b) and stronger northward meridional wind stress (Fig. 3.4c). The latter explains the north-south asymmetry in the equatorial SST response. Consistent with the weaker easterly zonal wind stress equatorial thermocline (Z20) tilt is reduced. The Z20 shoals in the west and to a lesser degree also in the east (Fig. 3.4d); the overall shoaling of Z20 indicates a substantial subsurface cooling due to the closing of the Panama Seaway (*Karas et al.*, 2009).

Fig. 3.5 depicts the simulated annual cycle of SST along the equatorial Pacific (averaged over 5°S-5°N) for each experiment (upper panels: low CO_2 experiments, lower panels: high-CO_2 experiments). In all experiments and consistent with present-day conditions, there is an annual cycle in the east and a semi-annual cycle in the west. However, the amplitude of the semi-annual and annual cycle considerably varies among the experiments. The annual cycle amplitude is defined here as the difference between the maximum and the minimum SST anomaly relative to the annual mean (*Bellenger et al.*, 2014; Table 3.2). Both the closing of the Panama Seaway and the narrowing of the Indonesian Passages can increase the annual cycle amplitude. In the four open-Panama Seaway runs (Fig. 3.5c, d, g, h), the annual cycle amplitude is relatively weak amounting to 1.09°C, 0.77°C, 1.28°C and 0.84°C in experiments LMP, LPP, HMP and HPP (Table 3.2), respectively. In response to the closing of the Panama Seaway (Fig. 3.5a, b, e, f), the amplitude of the SST annual cycle in the eastern equatorial Pacific increases, with values up to 2.00°C and 1.93°C in the experiments HMM and LMM, respectively. We note, however, that all simulations are biased with respect to the present-day SST annual cycle, with the cold tongue in the east not being maintained until the end of the calendar year. The simulation of the SST annual cycle in the eastern equatorial Pacific is a long-standing problem in climate models (e.g., *Mechoso et al.*, 1995).

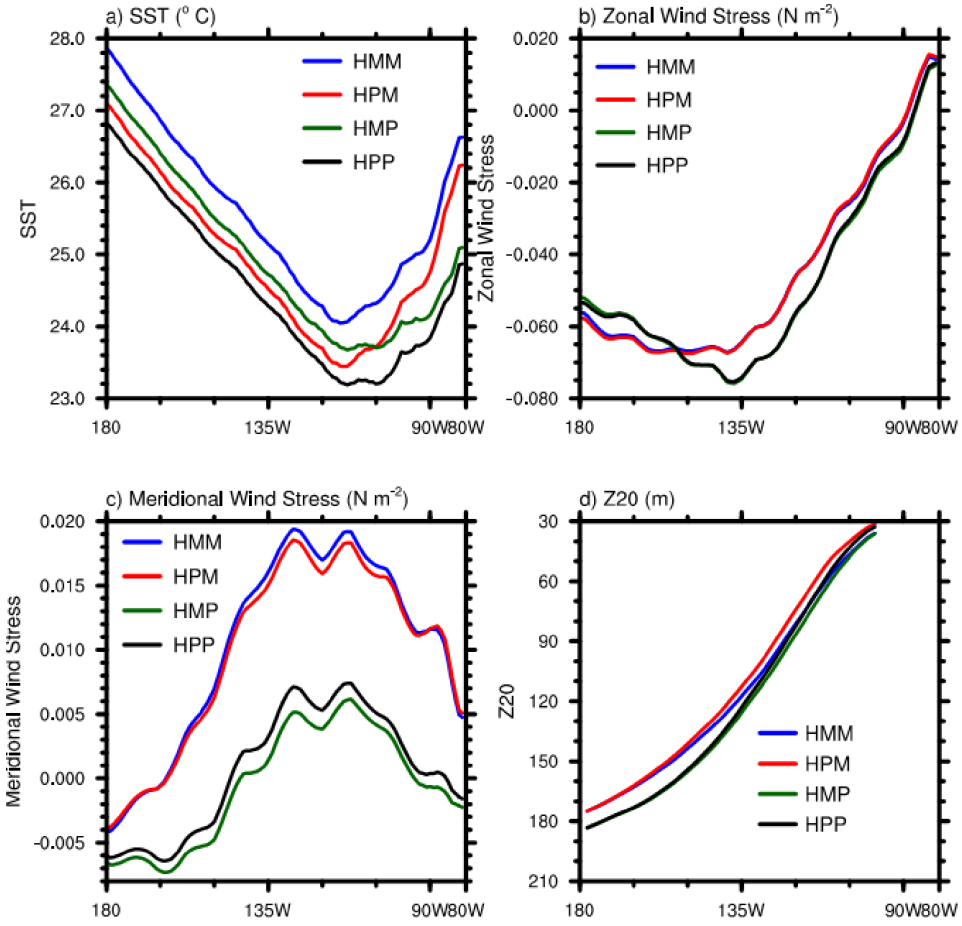

Figure 3.4: *Annual-mean values of selected variables along the equator (5°S-5°N) in the simulations with high CO_2. (a) SST (°C), (b) zonal wind stress (Nm^{-2}), (c) meridional wind stress (Nm^{-2}), (d) depth (m) of 20°C isotherm (Z20).*

Experiment name	Annual cycle amplitude (°C)
LMM	1.93
LPM	1.58
LMP	1.09
LPP	0.77
HMM	2.00
HPM	1.42
HMP	1.28
HPP	0.84

Table 3.2: *The amplitude of annual cycle in the east equatorial Pacific (EEP) is summarized. The amplitude of annual cycle in EEP is defined as the difference between the maximum and minimum Niño3 (150∼90°W, 5°S∼5°N) domain-averaged monthly mean SST anomalies in relative to the climatological annual mean.*

The changes in the annual cycle have the potential to modify ENSO. In fact, the level of ENSO variability, as shown by the standard deviation of the monthly SST anomalies, varies

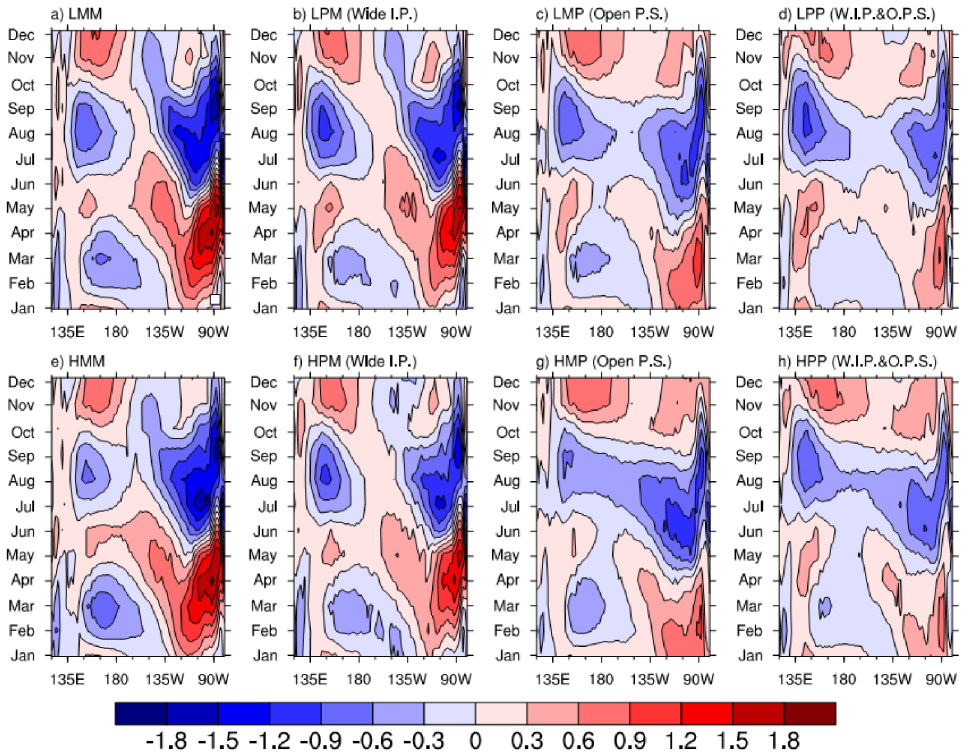

Figure 3.5: *Seasonal cycle (departure from the annual mean) of SST (°C) along the equatorial Pacific (averaged over 5°S∼5°N latitudinal band) in the simulations with (a-d) low and (e-h) high CO_2 and different ocean geometries (contour interval: 0.2°C).*

considerably among the simulations (Fig. 3.6). The ENSO amplitude, defined here as the standard deviation of the monthly SST anomalies averaged over the Niño3 region (90°W-150°W, 5°S-5°N), in the open Panama Seaway experiments LMP, HMP, LPP and HPP amount to 0.99°C, 1.07°C, 1.00°C, 1.04°C, respectively. Closing the Panama Seaway induces weaker ENSO variability. The ENSO amplitude in experiments LMM (Fig.3.6a) and HMM (Fig. 3.6b) reduces to 0.85°C and 0.91°C, respectively. Yet it is stronger than the wider-Indonesian Passages experiments LPM and HPM in which the ENSO amplitude is 0.80°C and 0.90°C, respectively. The strength of strong events remains relatively stable in the experiments (not shown). The spectra of the monthly SST anomalies averaged over the Niño3 region depict significant peaks at interannual timescales (Fig. 3.7), for low (Fig. 3.7a) and high (Fig. 3.7b) atmospheric CO_2. No significant changes in ENSO period are seen across the ensemble of experiments, indicating sensitivity of ENSO with respect to amplitude but not period.

In the following we investigate the changes in ENSO dynamics in more detail. This part benefits from extensive previous work on tropical climate changes with regard to the mean state, oceanic and atmospheric feedbacks, ocean adjustment processes and annual cycle, and response to global warming (e.g., *Latif and Keenlyside*, 2009; *Collins et al.*, 2010; *Vecchi et al.*, 2007; *Timmermann et al.*, 2007; *Huang*, 2015).

3.4 Annual cycle response

We start with the response of the annual cycle (Fig. 3.5), because the annual cycle strongly influences ENSO, as expressed, for example, by the seasonal phase locking of ENSO. The KCM simulates a considerably strengthened annual cycle in the eastern equatorial Pacific in response to the closing of the Panama Seaway, independent of the CO_2 concentration (Fig. 3.5b, d; experiments LPM and HPM). Utilizing the amplitude tendency equation (Eq. 3.2) deduced by *An and Choi* (2013), we address the physical mechanisms responsible for the enhancement in the amplitude of the SST annual cycle in eastern equatorial Pacific relative to the early Pliocene. Specifically, the effects of altered zonal and meridional surface winds, equatorial SST gradient and mixed layer depth are examined.

Forced by annual variations in solar radiation off the equator, the annual variability is initiated along the South American coast, exhibiting its largest amplitude near 15°S. The signal propagates to the equator and to the west due to surface ocean atmosphere interactions. At the equator, the annual cycle is related to the SST gradient, determined by the Walker circulation, and zonal currents in the mixed layer (*Xie*, 1996). The first term on the right hand side of Eq. 3.2 denotes the westward propagation of the annual cycle. It can be inferred from Fig. 4b that the zonal wind stress in the east decreases in response to the Panama Seaway closing (i.e., difference between experiments HMM and HMP). The surface zonal winds change due to air-sea interaction. More specifically, the closing of the Panama Seaway reduces the zonal winds east of 150°W and intensifies them to the west (Fig. 3.4b). The most prominent changes are seen in the surface meridional winds (Fig. 3.5c). In the experiments with a closed Panama Seaway (HMM and HPM), the KCM simulates much stronger meridional winds, which is key to the existence of an SST annual cycle (AC) at the equator.

Stronger surface meridional winds (given the negative correlation between surface meridional wind and SST within a seasonal cycle) drive a stronger AC (and vice versa) according to Eq. 3.2 ($\frac{\partial}{\partial t}\left\langle T'^2 \right\rangle \propto \bar{v} \cdot -\left(\left\langle v'T' \right\rangle\right)$). Changes in the mean surface meridional wind ($\bar{v}$) modify the surface latent heat flux thereby also affecting the amplitude of the AC. The closing of the Panama Seaway, on the other hand, substantially develops the meridional SST gradient (Fig. 3.2c, d, e, f) and surface meridional winds in the east. The latter is seen in the annual-mean meridional wind (southerly) stress which increases by more than 30% in response to the closing of Panama (Fig. 3.4c). Thus, the AC is substantially intensified under the enhanced southerly wind induced by the closing of the Panama Seaway. Narrowing the Indonesian Passages (i.e., difference between experiments HMM and HPM) hardly modifies the zonal SST gradient in the east. This geometry change mainly modifies the strength of the throughflow in the western Pacific, which hardly influences the eastern equatorial Pacific SST (Fig. 3.2a, b).

As indicated in Eq. 3.2, deeper mixed layer depth suppresses the amplitude of the AC, because its growth rate is inversely proportional to the mixed layer depth ($\frac{\partial}{\partial t}\left\langle T'^2 \right\rangle \propto \frac{\left\langle Q_s T' \right\rangle}{h}$ and $\frac{\partial}{\partial t}\left\langle T'^2 \right\rangle \propto \frac{\bar{Q}_E}{h} \cdot -\left(\left\langle v'T' \right\rangle\right)$). The effect of solely narrowing the Indonesian Passages (e.g., HMM minus HMP) hardly modifies the mixed layer depth (expressed by Z20) in the eastern equatorial Pacific (see Fig. 3.3c and Fig. 3.4d). In response to the closing of the Panama Seaway, the annual-mean mixed layer depth in the eastern equatorial Pacific changes only little either, with changes on the order of a few percent of the annual-mean depth. We conclude that

in the eastern equatorial Pacific, the change in mixed layer depth is much less important than that of the meridional winds. The influences of surface solar radiation (Q_S) and latent heat flux Q_E are negligible (not shown).

In summary, the enhanced equatorial asymmetry forced by the closing of the Panama Seaway is the dominant factor for amplifying the annual cycle during the course of the Pliocene. This can happen in two ways: Directly, the increased continentality to the north of the equator enhances northward meridional wind; indirectly, the strengthened AMOC warms the Northern Hemisphere through bipolar seesaw, which then affects the eastern equatorial Pacific in the same sense (*Zhang et al.*, 2005; *Wu et al.*, 2007). Our experimental setup, however, does not allow separation of these two effects. Consistent with *Timmermann et al.* (2004) and *Huang* (2015), lower CO_2-concentration weakens the annual cycle due to hemispheric cooling asymmetry.

3.5 ENSO stability

3.5.1 Linear feedbacks

In this section, we assess the stability of ENSO in the different experiments by quantifying the strength of the (linearized) positive and negative feedbacks. The first two terms in Eq. 3.4 are negative feedbacks which describe the dynamical and thermal damping effects on eastern equatorial Pacific SST anomalies. Dynamical damping feedback consists of three terms that are associated with mean zonal ($-\frac{\langle \bar{u} \rangle_E}{L_x}$) and meridional currents ($-\frac{\langle -2y\bar{v} \rangle_E}{L_y^2}$) as well as mean upwelling at the base of the mixed layer ($-\frac{\langle \bar{w} \rangle_E}{H_m}$). Dynamical damping, ranging from -3.38 yr^{-1} to -3.84 yr^{-1}, is the dominant negative feedback in the KCM (Fig. 3.8a). Please note the different scales in Fig. 3.8. The dynamical damping, especially its upwelling component, reduces slightly in response to the narrowing of the Indonesian Passages (the difference between experiments LMM and LPM, for example, amounts to -0.07 yr^{-1}). In response to the closing of the Panama Seaway, the change in dynamical damping is considerably larger (the difference between LMM and LMP, for example, amounts to about -0.25 yr^{-1}). This change results from several competing factors: the spatially averaged mixed layer in the eastern box, which enters the upwelling damping term in the denominator ($\propto -\frac{\langle \bar{w} \rangle_E}{H_m}$), moves slightly downward due to the enhanced southerly wind stress (Fig. 3.4c) and reduces the damping; the meridional current-damping term increases due to the enhanced meridional SST gradient. Its magnitude, however, is small compared to that of the upwelling-damping term. The zonal currents forced by surface zonal wind stress slightly weaken, but the magnitude is also rather small. The total dynamical damping thus declines, when moving from the early Pliocene geometry towards the modern. ENSO amplitude depicts a large negative correlation with the dynamical damping, which is shown in Fig. 3.8a that summarizes the results from all experiments. The regression indicates that stronger ENSO would go along with stronger dynamical damping.

The thermal damping term α is associated with the relationship between interannual anomalies of surface heat flux (shortwave, longwave, latent and sensible heat flux) and of SST in the eastern equatorial Pacific [$\langle Q \rangle_E = \alpha \langle T \rangle_E$]. It is computed as a linear least-squares regression of the net anomalous surface heat flux against SST anomalies. To compare α to other terms of the BJ Index, they are converted to a time scale by dividing by the mixed layer depth, the density and specific heat capacity of water. Compared to the dynamical damping, the thermal

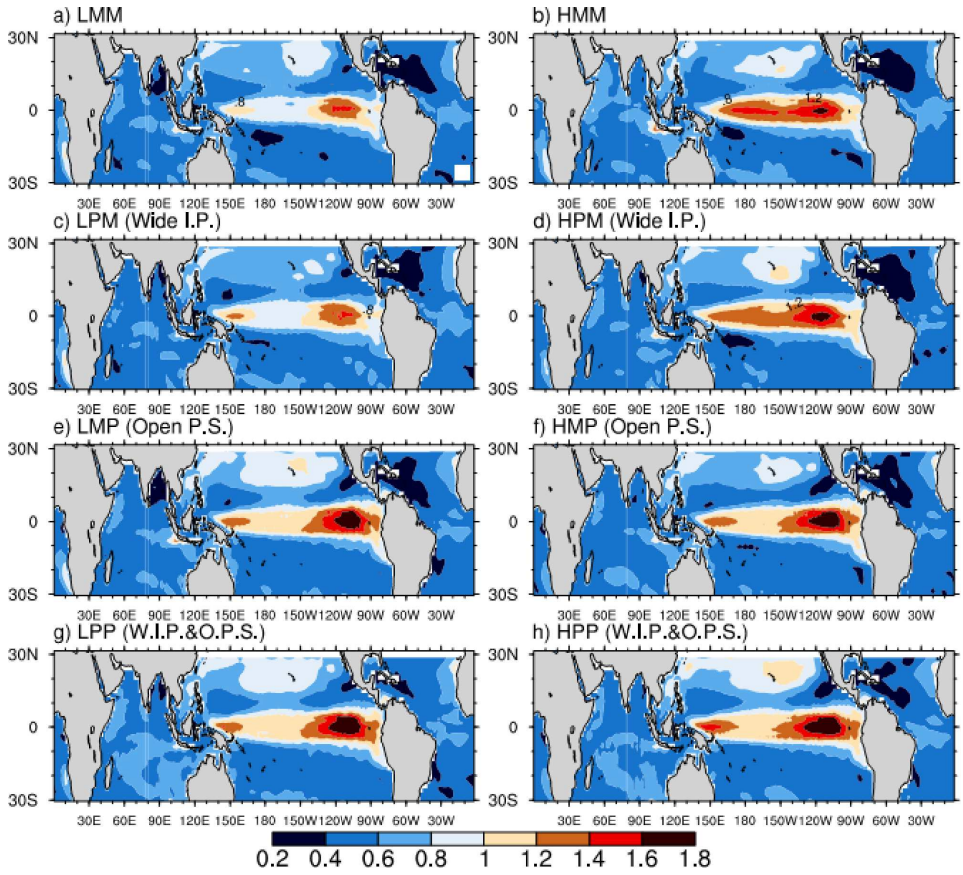

Figure 3.6: *SST variability (monthly standard deviation, °C) in the tropics in a) the pre-industrial control run LMM (low-CO_2). (c, e, g) low-CO_2 experiments with different ocean geometries. (b, d, f) are the corresponding high-CO_2 experiments (contour interval: 0.2°C).*

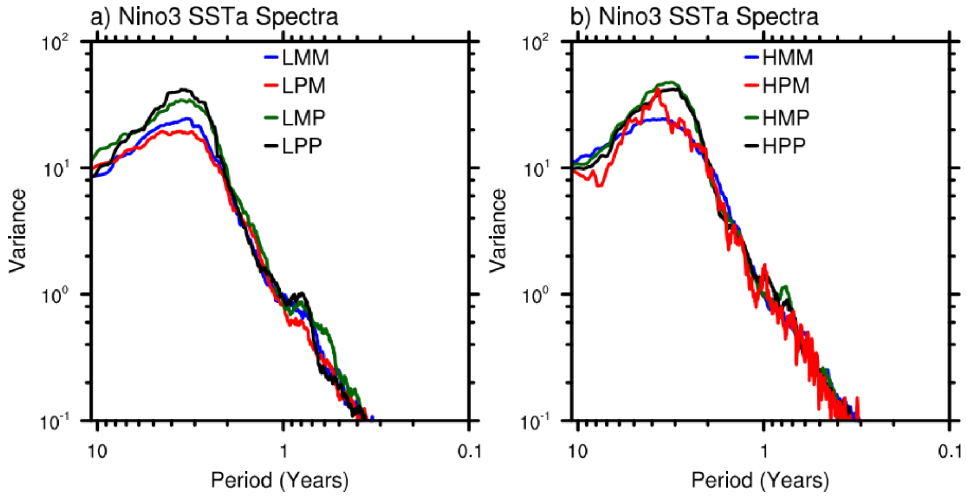

Figure 3.7: *Power spectra (°C^2) of SST anomalies averaged over the Niño-3 region (90°W-150°W, 5°S-5°N) in the experiments with (a) low and (b) high CO_2.*

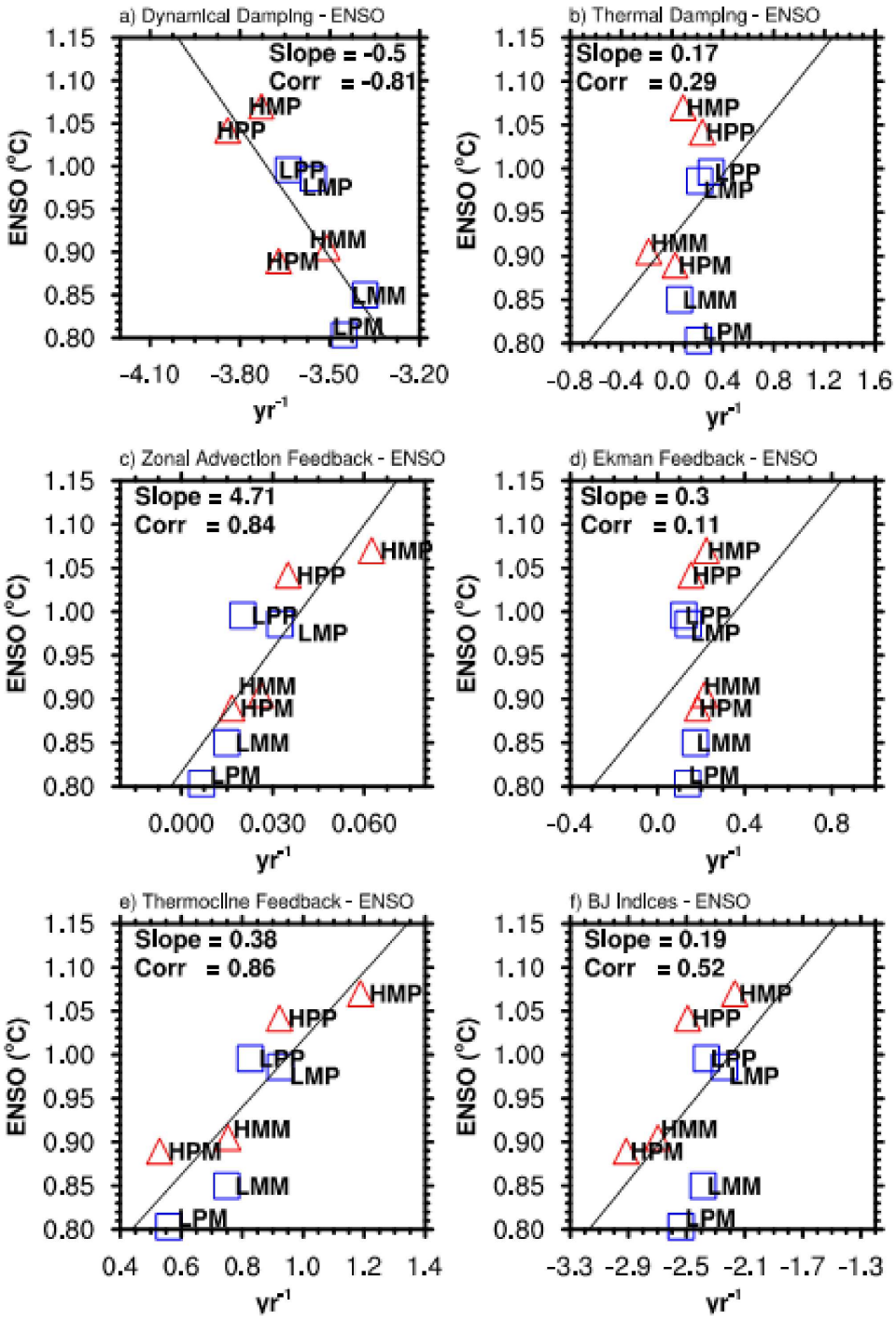

Figure 3.8: *Scatter plots of ENSO amplitude (°C) versus (a) dynamical damping, (b) thermal damping, (c) zonal advection feedback, (d) thermocline feedback, (e) Ekman feedback and (f) BJ index. Each component of the BJ index is converted to* yr^{-1}*. The black lines depict the least square regression. ENSO amplitude is defined by the standard deviation of Niño-3 SST anomalies. Red triangles and blue squares indicate high-*CO_2 *and low-*CO_2 *experiments, respectively.*

damping coefficients are rather small (Fig. 3.8b). Thus, the thermal damping is a much less important negative feedback in the KCM. Further, there is no consistent relationship of α with ENSO amplitude in the ensemble of experiments, as expressed by the rather low correlation of 0.29 (Fig. 3.8b).

All three positive feedbacks depend on several ocean-atmosphere coupling parameters (defined in Eqs. [5]-[8] of *Jin et al.* (2006)) that characterize the ocean response to surface wind stress anomalies and the atmospheric response to SST anomalies. The parameter μ_a describes the linear response of zonally averaged wind stress anomalies to forcing by eastern equatorial Pacific SST anomalies ($[\tau_x] = \mu_a \langle T \rangle_E$). Similarly, β_u and β_w characterize the linear effects of direct wind stress forcing on anomalous zonal currents and upwelling in the eastern equatorial Pacific ($\langle u \rangle_E = \beta_u [\tau_x] + \beta_{uh} \langle h \rangle_w$, $\langle H(\bar{w})\, w \rangle = -\beta_w [\tau_x]$). The coefficient β_h is estimated from the linear regression between Z20 east-west slope anomalies (defined as $\langle h \rangle_E - \langle h \rangle_W$) and the zonally averaged wind stress anomalies ($\langle h \rangle_E - \langle h \rangle_W = \beta_h [\tau_x]$).

Consistent with the results of *Kim and Jin* (2011b) analyzing climate models (10 out of 12 models) and *Lübbecke et al.* (2013) analyzing observations, the dominant positive feedback in the KCM is the thermocline feedback and it depicts a rather high correlation amounting to 0.86 with ENSO amplitude (Fig. 3.8d). The thermocline feedback describes how eastern equatorial Pacific thermocline perturbations and thus subsurface temperature anomalies impact SST. Both the zonal advection feedback (Fig. 3.8c) and the Ekman feedback (Fig. 3.8e) are considerably smaller. The thermocline feedback weakens in response to the closing of the Panama Seaway and intensifies in response to the narrowing of the Indonesian Passages, which results from the corresponding changes in coefficients β_h and a_h The weakening of β_h reflects the shoaling of Z20 in the eastern Pacific owing to the closing of the Panama Seaway (Fig. 3.3c, d). The thermocline depth, as expressed by Z20, is related to the subsurface ocean temperature. Since subsurface ocean water is actually transported into the mixed layer only when upwelling occurs, the relation is given by ($\langle H(\bar{w})\, T_{sub} \rangle_E = a_h \langle h \rangle_E$) in the thermocline feedback, which follows the simple formulation of the subsurface temperature parameterization used in the *Zebiak and Cane* (1987) model. The parameter a_h weakens in response to the closing of the Panama Seaway, which means for the closed-Panama runs (i.e. experiments LMM and HMM) that Z20 in the eastern equatorial Pacific becomes shallower in comparison to the open-Panama runs (i.e. experiments HMP, HPP, LMP and LPP) (Fig. 3.4d).

The Ekman feedback is suppressed by the thermocline feedback (*An and Choi*, 2013), since the latter modifies vertical stratification. A larger thermocline depth yields weaker stratification ($\left\langle -\frac{\partial \bar{T}}{\partial z} \right\rangle_E$), and thus the growth rate by this effect is reduced. On the contrary, *Manucharyan et al.* (2014) show that the Ekman feedback can even overcome the thermocline feedback in experiments with a deep thermocline depth in the eastern equatorial Pacific. The Ekman feedback becomes slightly stronger in response to the closing of the Panama Seaway (Fig. 3.8e).

Summing up all negative and positive feedbacks, the BJ Index is negative in all eight simulations conducted with the KCM (Fig. 3.8f), indicating a damped ENSO mode, with the open-Panama Seaway experiments (HMP, HPP, LMP and LPP) less damped. Notably, despite large variations in the magnitudes of the individual negative and positive feedbacks, the BJ Index is relatively constant, staying in the range from -2.3 yr^{-1} (experiment HMP) to -1.65 (experiment LPP) yr^{-1} (Fig. 3.8f). Comparing experiments LPM and LMM or HPM and HMM

shows that the narrowing Indonesian Passages hardly modifies ENSO stability. The closing of the Panama Seaway has a much stronger effect on ENSO and reduces its amplitude. Blue squares and red triangles in Fig. 3.8 indicate the low CO_2 and high-CO_2 runs, respectively. Low-CO_2-concentration yields weaker dynamical damping, zonal advection feedback and thermocline feedback, and stronger Ekman feedback. The major results, however, are basically independent of the CO_2 concentration.

We note that the computed magnitudes should be interpreted with caution in light of the accumulated errors of the various linear regressions constituting the BJ Index. Further, BJ analysis does neither account for stochastic processes nor the nonlinearities important for strong El Niño events (*Graham et al.*, 2014). Additionally, the results depend on the size and location of the averaging box, and the selection of the depth to compute subsurface temperature anomalies. For example, we choose here the same region as in *Kim and Jin* (2011b) to ease comparison with the BJ analysis of other climate models. Alternatively, we could have selected a smaller region such as the Niño-3 region, the region of maximum interannual SST variance. Although the calculated values may vary with the choice of the averaging box, the main findings presented above do not change, which has been confirmed by a number of sensitivity tests (not shown).

3.5.2 Relationship of ENSO amplitude to the annual cycle

As suggested, for example, by *Liu* (2002), the annual cycle tends to suppress the development of ENSO through the nonlinear mechanism of frequency entrainment. Such interaction is strongly supported by our set of model experiments, which is a major result of this study. As shown in Fig. 3.9, the suppression effect of the annual cycle on ENSO is clearly seen in our simulations. The correlation between the strength of the annual cycle and ENSO amplitude calculated from the eight model experiments amounts to -0.83. For example, closing the Panama Seaway induces a significantly enhanced annual cycle, largely by strengthening the meridional winds, and reduced ENSO amplitude by about 20%. It should be noted, however, that the origin of changes in the annual cycle and BJ index, especially the dominant thermocline feedback in the latter, are closely related to geometry changes. This hinders a clear separation of the relative importance of positive feedback and damping impact of annual cycle on ENSO variability.

3.6 Summary and discussion

This study investigates the impact of changes in the Panama Seaway and Indonesian Passages during the Pliocene on tropical Pacific climate and its variability. In particular, we have explored tropical Pacific mean-state and annual cycle changes, and changes in the El Niño/Southern Oscillation (ENSO) in a set of eight sensitivity simulations with the Kiel Climate Model (KCM), which differ in the geometry of the aforementioned passages and atmospheric CO_2-concentration. We studied the effect of the closing of the Panama Seaway and the narrowing of the Indonesian Passages, individually and together, using two different CO_2-concentrations.

The closing of the Panama Seaway in the KCM strongly modifies the tropical Pacific climatology. We observe shoaling of the thermocline across the tropical Pacific and strengthening of the southerly wind stress in the east, where the latter is forced by an enhanced meridional

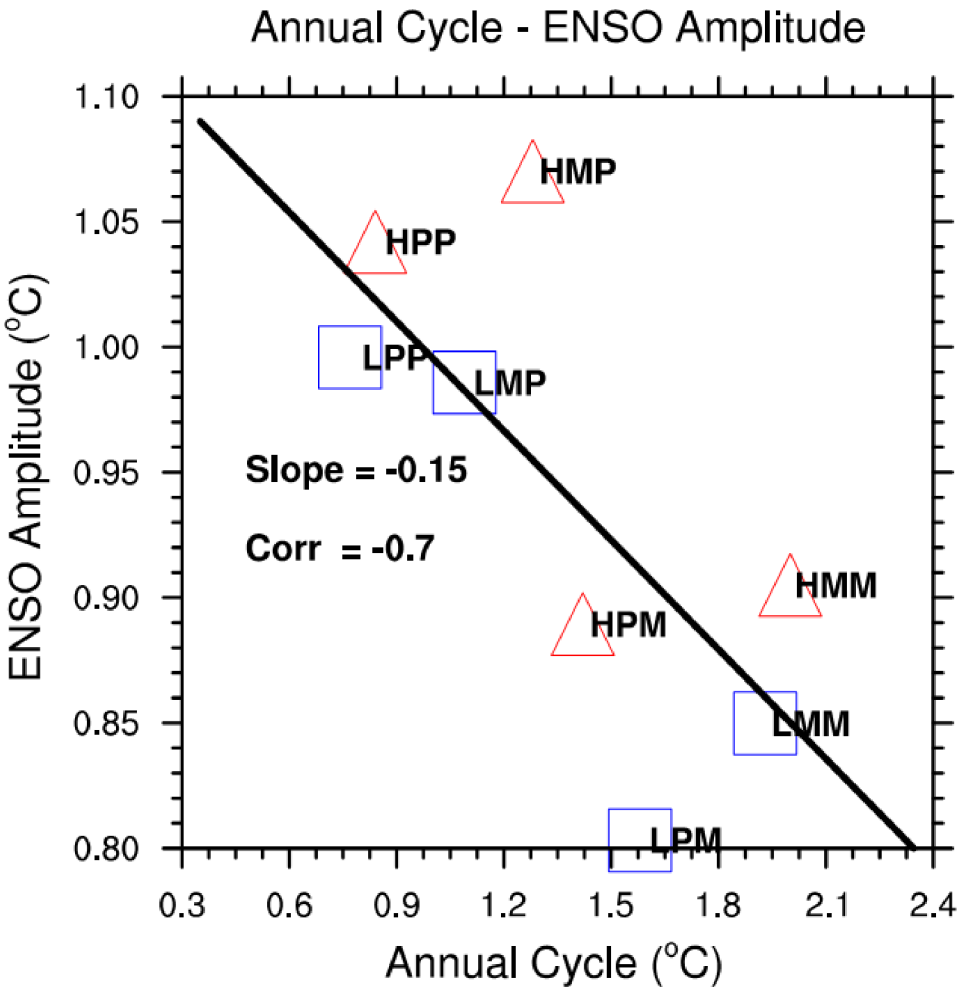

Figure 3.9: *Scatter plot of ENSO amplitude (°C) versus annual-cycle strength (°C). The meaning of the symbols is as in Fig. 3.8. The black line depicts the least square regression. The amplitude of the annual cycle is defined as the difference between the maximum and minimum SST in Niño-3 region (see Fig. 3.5).*

sea surface temperature (SST) gradient. A slightly decreased zonal equatorial SST gradient and zonal wind stress, indicating ocean-atmosphere coupling, is also simulated in the eastern equatorial Pacific. The strongly enhanced southerly wind stress simulated in response to the closing of the Panama Seaway is the most important factor strengthening the annual cycle. The changes in the Indonesian Passages have less impact.

We find that the simulated ENSO is relatively robust across the set of experiments. ENSO amplitude decreases in response to closing the Panama Seaway and increases in response to narrowing the Indonesian Passages (consistent with *Jochum et al.*, 2009). The dominant ENSO period does not significantly change in the experiments. Higher atmospheric CO_2 enhances ENSO amplitude, consistent with *Park et al.* (2009) and *Latif et al.* (2015). As ENSO can be understood within the recharge oscillator framework, the Bjerknes stability analysis developed by *Jin et al.* (2006) is applied to assess changes in ocean-atmosphere feedbacks and ENSO dynamics from a linear perspective. The Bjerknes index (BJ), which sums all positive and

negative feedbacks, illustrates relatively small changes across the set of experiments albeit large differences in the individual positive and negative feedbacks, which is consistent with the small but statistically significant changes in ENSO amplitude and only modest changes in ENSO period. An increase of the BJ index is accompanied by larger ENSO amplitude and vice versa.

In all experiments, dynamical damping and thermocline feedback are the dominant negative and positive feedbacks, respectively. Moreover, weakening of positive feedbacks is largely compensated by reduced dynamical damping. As a result, ENSO behavior is relatively stable across the set of experiments. Narrowing the Indonesian Passages in the model shows opposite effects in comparison to closing the Panama Seaway, and the influence of the former is much weaker. The suppression effect of the SST annual cycle on ENSO is a robust feature of the KCM: there is a clear linear relationship between the strength of the annual cycle and ENSO amplitude in the ensemble of model simulations with varying ocean geometry and atmospheric CO_2. Interestingly, changes of positive and negative feedbacks in response to closing the Panama Seaway mirror the effects of lower CO_2-concentration on these feedbacks.

Our results may provide some clues about the climate evolution from the Pliocene to the present. There are, however, several limitations in the present study. For example, when employing high atmospheric CO_2 and an open Panama Seaway, the model fails to reproduce the full extent of Pliocene warming in the mid-latitudes and upwelling regions as suggested by proxy data. This might be due to a number of physical processes not well resolved or poorly represented in the KCM. For example, variations in orbital forcing, ice sheets and vegetation distribution are not considered in the experiments. Model bias may also degrade the response.

Acknowledgments

This study was supported by the Excellence Cluster "The Future Ocean" at Kiel University and the SFB 754 "Climate Biogeochemistry Interactions in the Tropical Ocean", which both are sponsored by the German Science Foundation (DFG). The model simulations were conducted at the Computing Center of Kiel University. Zhaoyang Song is a Ph.D. student, sponsored by the China Scholarship Council (CSC).

Supplemental figures

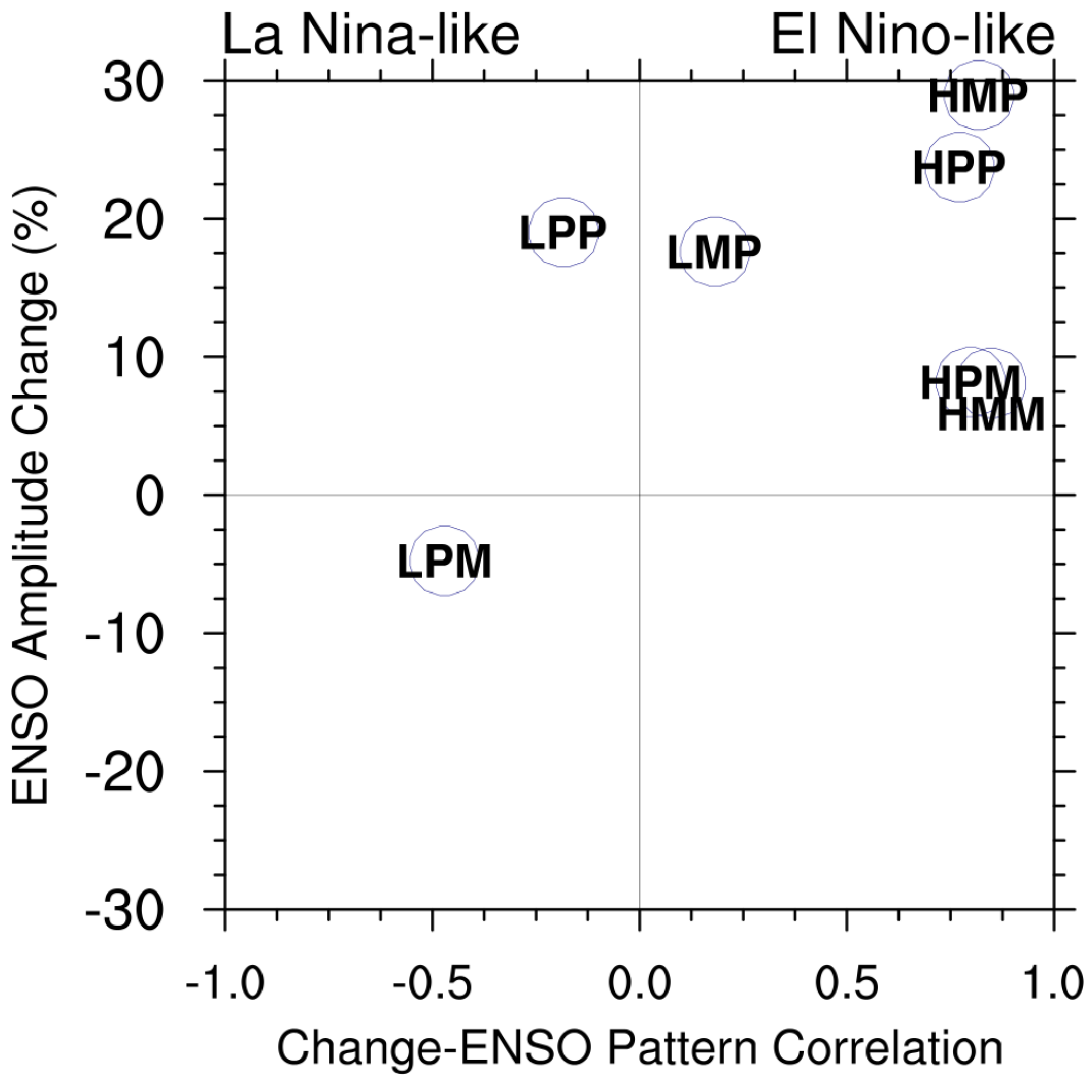

Figure S3.1: *Scatter plot of the relative change in ENSO amplitude (%) versus the correlation of mean state changes projected on the LMM leading EOF mode.*

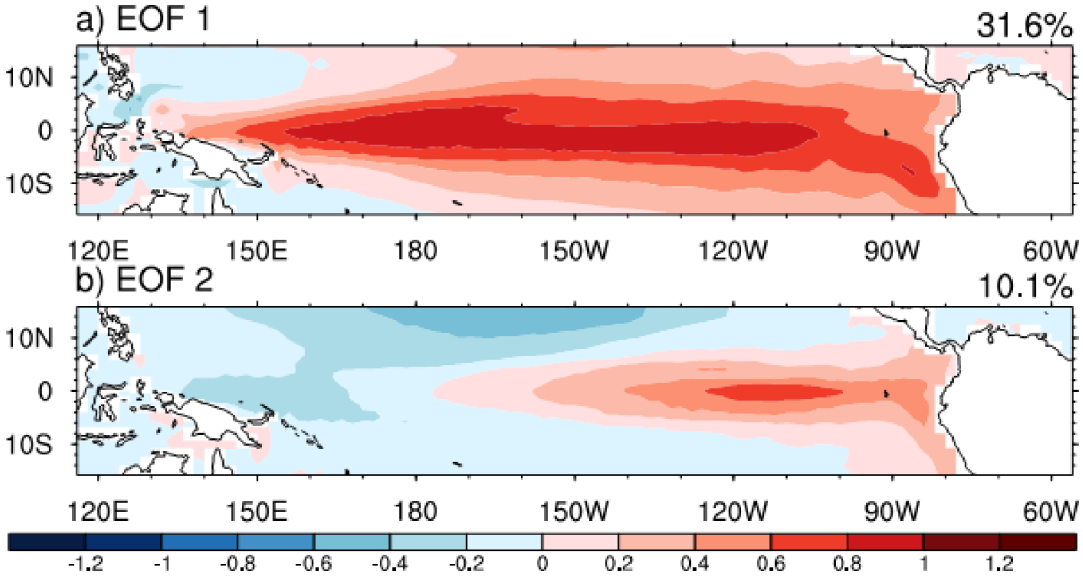

Figure S3.2: *The monthly SST anomalies (300-year) are projected onto the (a) first and (b) second empirical orthogonal functions of experiment LMM for the tropical Pacific. The unit is °C/°C, which represents SST anomalies per standard deviation. The percentage of variance explained by each EOF is shown at the top of each panel.*

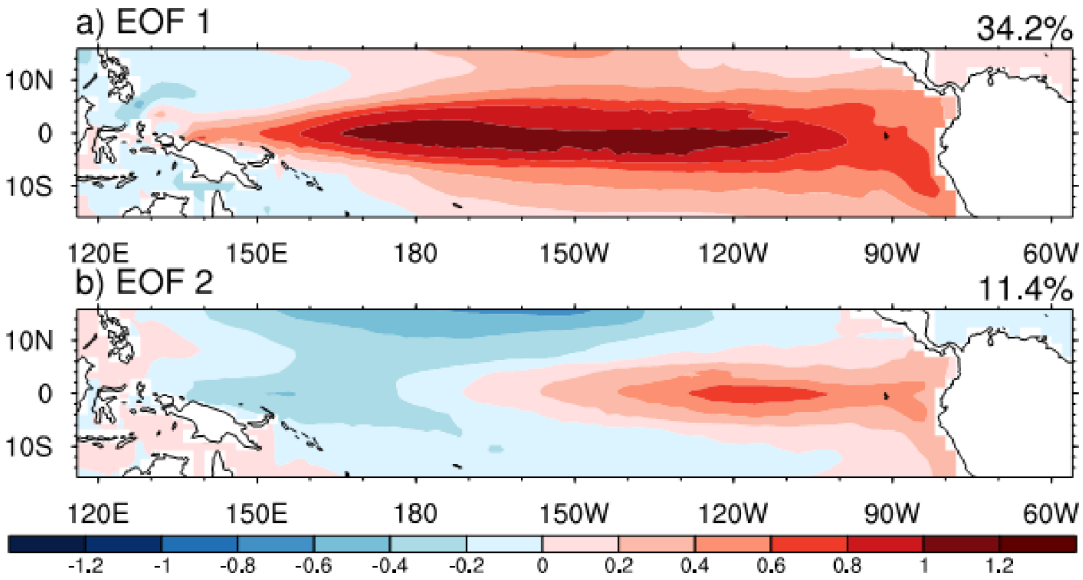

Figure S3.3: *Same as Fig. S3.2 but for experiment HMM.*

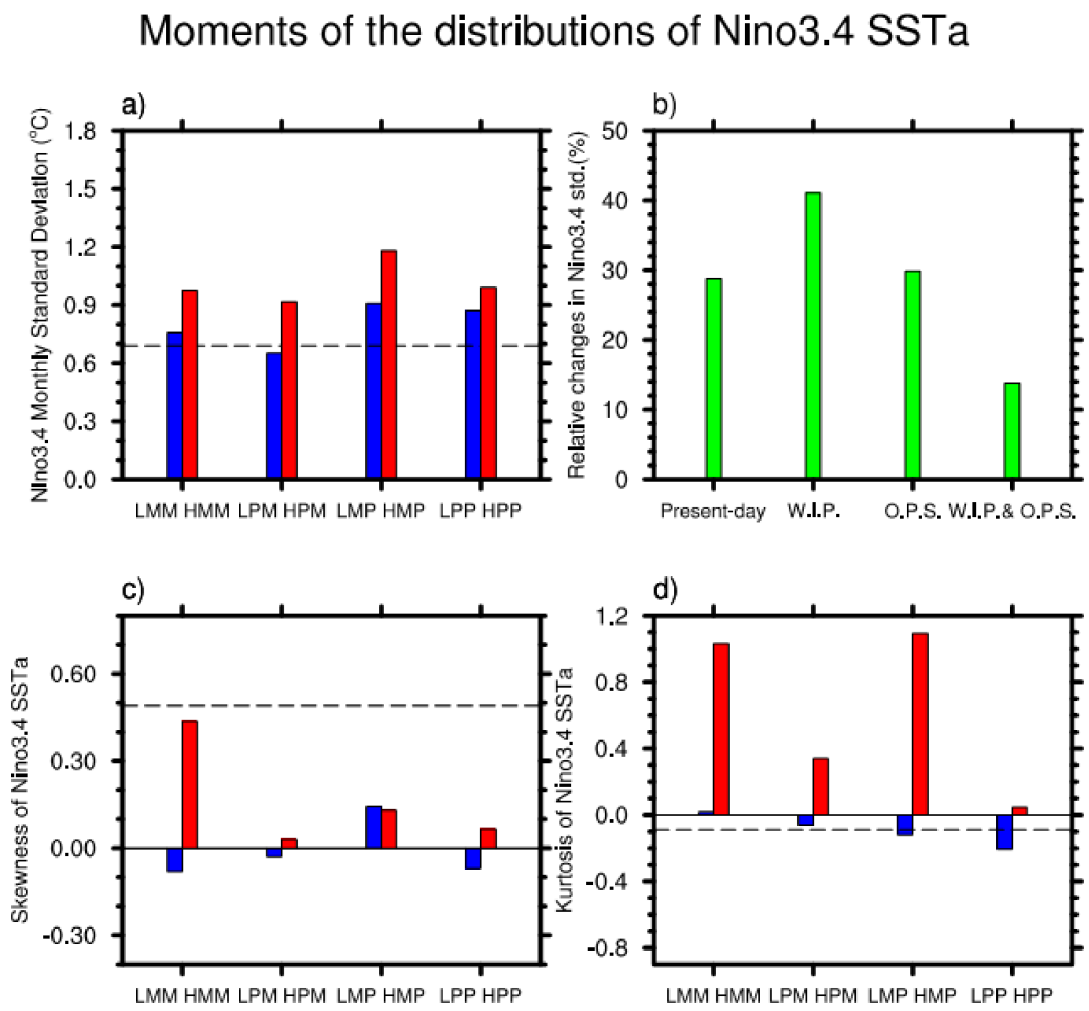

Figure S3.4: *(a) Standard deviation, (b) relative changes of standard deviation, (c) skewness and (d) kurtosis of monthly Niño3.4 SST anomalies for all experiments. The black dashed line indicates the ERSST observations. Positive skewness represents stronger extreme El Niños than extreme La Niñas. Positive kurtosis stands for a more strongly peaked distribution than the normal distribution.*

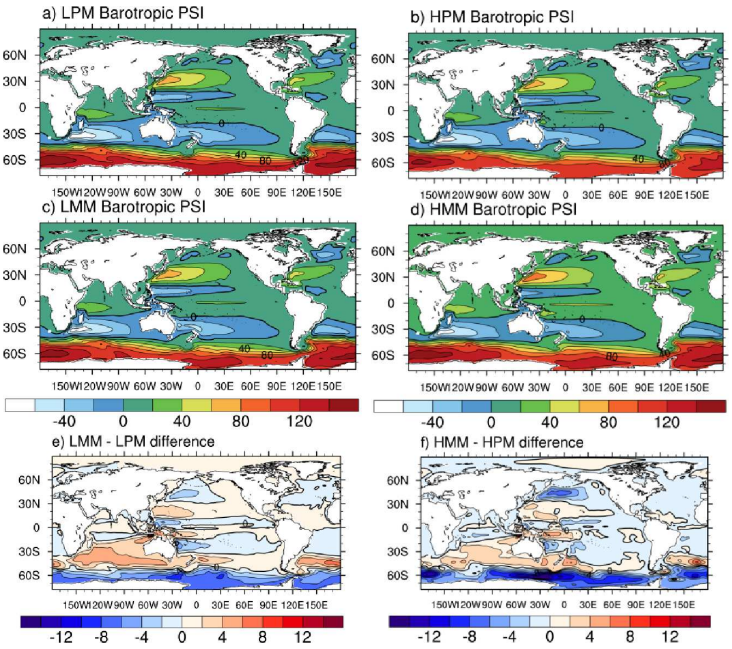

Figure S3.5: *Barotropic Stream function for wide Indonesian Passages experiments (a) LPM and (b) HPM, control experiments (c) LMM (d) HMM and responses (e) and (f) with respect to LMM and HMM due to narrowing Indonesian Passages (Unit: Sv).*

Chapter 4

Expanding Greenland Ice Sheet Enhances Sensitivity of Plio-Pleistocene Climate to Obliquity Forcing

This chapter is a reprint of paper "Expanding Greenland Ice Sheet Enhances Sensitivity of Plio-Pleistocene Climate to Obliquity Forcing in the Kiel Climate Model" published in Geophysical Research Letters

Citation: Song, Z., Latif, M., Park. W. (2017). Expanding Greenland Ice Sheet Enhances Sensitivity of Plio-Pleistocene Climate to Obliquity Forcing in the Kiel Climate Model. Geophysical Research Letters, 44. doi:10.1002/2017GL074835.

Abstract

Proxy data suggest that the onset of Northern Hemisphere glaciation during the Plio-Pleistocene from 3.2 to 2.5 Ma before present resulted in enhanced climate variability at the obliquity (41 kyr) frequency. Here, we investigate the influence of the expanding Greenland ice sheet (GrIS) on the mean climate and obliquity-related variability in a series of climate model simulations. These suggest that an expanding GrIS weakens the Atlantic Meridional Overturning Circulation (AMOC) by ∼1 *Sverdrup*, mainly due to reduced heat loss in the Greenland-Iceland-Norwegian Sea. Moreover, the growing GrIS amplifies the Hadley circulation response to obliquity forcing driving variations in freshwater export from the tropical Atlantic and in turn variations of the AMOC. The stronger AMOC response to obliquity forcing, by about a factor of 2, results in a stronger global-mean near-surface temperature response. We conclude that the AMOC response to obliquity forcing is important to understand the enhanced climate variability at the obliquity frequency during the Plio-Pleistocene transition.

4.1 Introduction

The transition from the Pliocene to Pleistocene around 3.2 to 2.5 Million years before present (Ma B.P.) was characterized by the onset of Northern Hemisphere glaciation (NHG) and an increase of climate variability at the obliquity frequency (41 kyrs) (e.g., *Lisiecki and Raymo*, 2005; *Lisiecki and Raymo*, 2007; *Rohling et al.*, 2014; *Martínez-Botí et al.*, 2015). Marine sedimentary records of ice rafted debris (e.g., *Bailey et al.*, 2013) and temperature proxies records from recovered around the globe indicate a global cooling trend during that time (e.g., *Herbert et al.*, 2010; *Lawrence et al.*, 2009; *Lawrence et al.*, 2010; *Naafs et al.*, 2010), which was particularly pronounced between 3.0 and 2.5 Ma B.P. (*Mudelsee and Raymo*, 2005)(Figures 1.2a and 1.2c). The cooling trend was accompanied by increased variability in North Atlantic sea surface temperature (SST) and global mean benthic foraminiferal δ^{18}O; a proxy for ice volume and deep-sea temperature (*Lisiecki and Raymo*, 2005, the LR04 stack), in the 41 kyr band (Figures 1.2b and 1.2d analyzed with ARAND) (*Howell*, 2001). *Lawrence et al.* (2009) found that North Atlantic SST began to lead δ^{18}O significantly coincident with the strong cooling trend at Ocean Drilling Program (ODP) site 982. The progressively stronger level of variability in the obliquity band in a number of proxies suggests a link between the growth and persistence of the Greenland ice sheet (GrIS) and the strengthening climate response to obliquity forcing.

The Atlantic Meridional Overturning Circulation (AMOC) transports large amounts of salt and heat poleward and also exerts a strong control on the stratification and distribution of water masses in the deep ocean (*Kuhlbrodt et al.*, 2007). Thus, the AMOC has a profound influence on the Earth's climate and its variability. The tilt of Earth's rotational axis, known as obliquity, controls the distribution of top-of-atmosphere (TOA) incoming solar radiation with respect to its seasonal and meridional contrast but not global-mean insolation. Low obliquity weakens the seasonal insolation contrast between the summer and winter hemispheres and strengthens the meridional insolation gradient within the summer hemisphere and vice versa (Figures S4.1a and S4.1b calculated after *Bretagnon and Francou*, 1988; *Mantsis et al.*, 2014). Hence, inter-hemispheric insolation at low obliquity is associated with weak cross-equatorial Hadley circulation and reduced heat transport from the summer hemisphere to the winter hemisphere and vice versa (*Mantsis et al.*, 2014). Obliquity can affect the AMOC by freshwater forcing and early studies suggested that changes in the AMOC were likely driven by changes in ice volume. For instance, *Imbrie et al.* (1992) found that North Atlantic benthic δ^{13}C records reflecting deep water mass changes, slightly lagged ice volume at the obliquity frequency. Comparing with SST proxy records from the North and tropical Atlantic revealed the link between the benthic δ^{13}C and northward heat transport and hence, overturning rate variation (*Lisiecki et al.*, 2008).

The GrIS is the largest body of ice and freshwater reservoir in the Northern Hemisphere equivalent to 7 m global sea level rise (*Gregory et al.*, 2004). Its average elevation is 1829 m above sea level with a maximum height of 3278 m (calculated with the data set of *Bamber et al.*, 2001). Freshwater input from GrIS melting can substantially weaken the AMOC in anthropogenic climate change simulations (e.g. *Mikolajewicz et al.*, 2007). The topographic relief of the GrIS and high surface albedo generates a cold and high pressure center influencing the downstream Northern Hemisphere mid-latitude westerly flow and northeasterly trade winds, thus affecting the North Atlantic Oscillation (NAO), storm activity in the North Atlantic sector, and Intertropical Convergence Zone (ITCZ) (*Dethloff*, 2004; *Chiang and Bitz*, 2005; *Davini et al.*,

2015).

Here, we investigate the climatic impact of the expanding GrIS during the Plio-Pleistocene transition. This includes, among others, the mean response of the AMOC and its sensitivity to obliquity forcing. We show how the expanding GrIS may affect the global climate variability through the AMOC and associated atmospheric circulation changes. The paper is organized as follows: section 4.2 describes the climate model, the experimental setup and methods for heat and moisture transport calculation. The influence of the buildup of the GrIS on the AMOC and its obliquity-forced variability are addressed in section 4.3. A summary and discussion of the main results are given in section 4.4.

4.2 Model and experimental design

The Kiel Climate Model (KCM) (*Park et al.*, 2009), a fully coupled atmosphere-ocean-sea ice general circulation model (AOGCM), is used to perform long-term (at least 1,900 model years) climate simulations. The atmosphere model is ECHAM5 (*Roeckner et al.*, 2006) which is integrated with T31 (3.75° x 3.75°) horizontal resolution and 19 vertical levels up to 10 hPa. The ocean-sea ice component is NEMO (*Madec*, 2008) on a 2° Mercator mesh, with 31 vertical levels. The meridional resolution increases towards lower latitudes, with 0.5° in the equatorial region. The two components are coupled with the OASIS3 coupler (*Valcke*, 2006). No form of flux correction or anomaly coupling is employed.

We perform a series of simulations (Table 4.1). A control integration of the KCM, hereafter named **Modern**, is 2,700 years long and initialized with the Levitus climatology of temperature and salinity. The control integration employs the modern GrIS. In the mid Piacenzian (3,264 to 3,025 Ma B.P.) run, hereafter named **Plio**, only the configuration of GrIS is implemented. A snapshot of the mean topography and ice sheet mask of the GrIS is taken from the latest Pliocene Research, Interpretation and Synoptic Mapping (PRISM4) reconstruction data set (*Dowsett et al.*, 2016, and references therein). The mean GrIS elevation in **Plio** is 850 m, which is 781 m lower than that in **Modern** (1,631 m, Fig. 4.1a). The area of the GrIS in **Plio** shrinks to 50% of that in **Modern** (Fig. 4.1b). Soils, lakes, vegetation and topography outside of Greenland ice sheet regimes in **Plio** are all set to modern. Different from the Ei^{400} simulation in PlioMIP Phase 2 (*Haywood et al.*, 2016), which investigates both the impact of Greenland and Antarctic ice sheets, **Plio** is to assess the orographic impact of GrIS on the mean state.

Four senstitivity experiments with differing obliquity are carried out to investigate the impact of the GrIS on climate variability. The first two experiments adopt the modern GrIS boundary conditions with idealized low (22.34°, $\mathbf{Modern}_{Low}$) and high (24.05°, $\mathbf{Modern}_{High}$) obliquity extremes as present during the Pliocene-Pleistocene transition based on the calculation by *Laskar et al.* (2004) (Fig. S4.2). The other two experiments are identical but employ the **Plio** GrIS boundary conditions and idealized low (22.34°, $\mathbf{Plio}_{Low}$) and high obliquity (24.05°, $\mathbf{Plio}_{High}$). The modern value for longitude of perihelion (282.7°) and eccentricity (0.0167) is computed after *Berger and Loutre* (1991). The CO_2-concentration in **Plio** simulations is fixed at 405 ppm following the Pliocene Model Intercomparison Project (PlioMIP) protocol (*Haywood et al.*, 2011). Apart from **Modern**, all runs are integrated for 1,900 years, with the monthly-mean output of the last 600 years taken for analysis. Initialization is as follows;

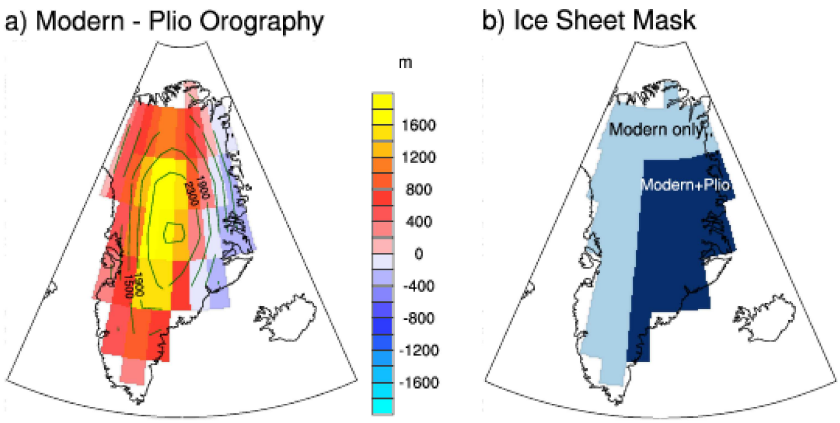

Figure 4.1: *The orography and ice sheet mask of GrIS and their representation in the KCM. (a) Difference (**Modern** minus **Plio**) of orography (shading, unit: m) and orography for **Modern** (contours, interval: 400m). (b) Dark blue shaded areas represent ice sheet regimes in both **Modern** and **Plio**, light blue areas represent ice sheet regimes only in **Modern**. The configuration in **Plio** is a snapshot of mid-Piacenzian conditions taken from PRISM4 (Dowsett et al., 2016).*

Modern$_{High}$, **Modern**$_{Low}$ and **Plio** start from conditions at year 1,000 of **Modern**. **Plio**$_{High}$ and **Plio**$_{Low}$ start from year 500 of **Plio**.

Experiment name	Greenland ice sheet	Obliquity (°)	Integration time (model years)
Modern	Modern	23.44	2700
Plio	Mid-Piacenzian	23.44	1900
Modern$_{Low}$	Modern	Low	1900
Modern$_{High}$	Modern	High	1900
Plio$_{Low}$	Mid-Piacenzian	Low	1900
Plio$_{High}$	Mid-Piacenzian	High	1900

Table 4.1: *Overview of the model simulations analyzed in this paper. **Modern** and **Plio** of the experiments are based on Modern and mid-Piacenzian (PRISM4) Greenland Ice sheet condition (Dowsett et al., 2016), respectively. Subscripts Low and High represent low (22.34°) and high (24.05°) obliquity, respectively.*

4.3 Results

4.3.1 Mean state

We first investigate the impact of GrIS expansion on the mean state by discussing long-term annual-mean and winter-mean (December-February (DJF)) changes of selected variables. By and large the response is in agreement with previous model results (*Davini et al.*, 2015). The elevated **Modern** GrIS cools (**Modern** versus **Plio**) the annual-mean T_{2m} (2m-air-temperature) by almost 6 K averaged over Greenland (Fig. 4.2a contours). DJF and JJA (June-August) average temperature over Greenland decreases by 6.3 K and 4.9 K, respectively (not shown). With the KCM assuming a lapse rate of 6.5 K/1,000 m due to elevated topography, the elevation-induced near-surface cooling is 5 K, while the imposed change in albedo would only account

for 0.9 K as a residual. The interhemispheric temperature gradient, defined as the difference of averaged T_{2m} between the Northern (0° - 90°N) and Southern Hemisphere (0° - 90°S), declines from 1.05 K in **Plio** to 0.77 K in **Modern**. This value is smaller than that calculated from observations and the CMIP3 multi-model mean of 1.24 K and 1.13 K, respectively (*Kang et al.*, 2015). On the other hand, the intrahemispheric temperature gradient in the KCM, defined as the difference of averaged T_{2m} between the tropics (5°S - 5°N) and northern high latitudes (60°N - 90°N), increases from 7.9 K in **Plio** to 8.2 K in **Modern**. The change in interhemispheric and intrahemispheric temperature gradient does arise not only from cooling over Greenland but also from a weak cooling over the North Atlantic (Fig. 4.2a). The expansion of the GrIS leads to surface cooling of the North Atlantic which amounts to 0.15 K averaged over 40°N - 60°N (Fig. 4.2a shading). The western part of the GIN (Greenland-Iceland-Norwegian) Sea cools, but the eastern part and the Barents Sea warms. The simulated Barents Sea inflow, defined as the gradient of the barotropic streamfunction between Svalbard and the northern tip of Norway, increases by 2.2 *Sverdrups* (*Sv*) (1 $Sv = 10^6$ m^3/s) from **Plio** to **Modern** (Fig. S4.3). This presumably is related to weakened easterly winds (Fig. 4.2d) and the subsequent retreat of sea ice (Fig. S4.4), especially in DJF. Surface warming is largest in the Barents Sea through the positive ocean-sea ice-atmosphere feedback in this region (*Semenov et al.*, 2009). Surface temperature responses in the tropics and subtropics are small but statistically significant at the 99% confidence level according to a Student's t-test (Fig. 4.2a hatching), indicating Atlantic wide influences.

The expansion of the GrIS reduces the annual-mean precipitation over Greenland (Fig. 4.2b), mainly by reduced specific humidity caused by the higher elevation and weaker atmospheric upward motion (not shown). The expanding GrIS induces a seasonal southward shift of the Intertropical Convergence Zone (ITCZ, Fig. S4.5 calculated after *Hu et al.*, 2007) over the tropical Atlantic (Fig. 4.2b), due to the asymmetric SST response with cold SST anomalies north and warm SST anomalies south of the mean position of the ITCZ (Fig. 4.1a). The positive wind-evaporation-SST feedback has been suggested to enhance the ITCZ response (*Chiang and Bitz*, 2005), but in the KCM there is no significant change in the tropical Atlantic surface heat flux (Fig. 4.2d).

In the KCM, the AMOC strength is mainly determined by deep convection at two sites: one is south of Greenland (48°N-60°N, 24°W–45°W; the lower green box in Fig. 4.2e) and the other in the GIN Sea (66°N-78°N, 6°W-12°E; the upper green box in Fig. 4.2e). The DJF-mean near-surface winds transport cold air from North America and the Arctic to the Irminger Sea and the GIN Sea where the ocean loses heat to the atmosphere in boreal winter (DJF, Fig. 4.2c shows the fields for **Modern**). The elevated GrIS in **Modern** drives a cold- and high-pressure center over Greenland, which weakens the near surface winds over the two deep convection sites. The oceanic heat loss to the atmosphere is reduced by 11.4 W/m^2 (7%) and 35.5 W/m^2 (21.4%) over the convection sites south of Greenland and in the GIN Sea, respectively (Fig. 4.2d). The DJF-mean mixed layer depth displays a dipole response pattern shoaling on average by 86 m south of Greenland but only 6 m in the GIN Sea (Fig. 4.2e, more details can be seen in Fig. S4.6e). Consistently, the AMOC weakens in the annual mean (Fig. 4.2f). The AMOC index, defined as the maximum overturning stream function at 30°N, reduces from a multi-century mean of 14.1 in **Plio** to 13.2 *Sv* in **Modern** (the standard deviation of interannual variability remains unchanged at $\sigma = 0.70$ *Sv*, Fig. S4.7). Sea ice also expanded in **Modern** due to the slightly weaker AMOC, which suggests expansion of sea ice conincident with the NHG (*Knies et al.*, 2014).

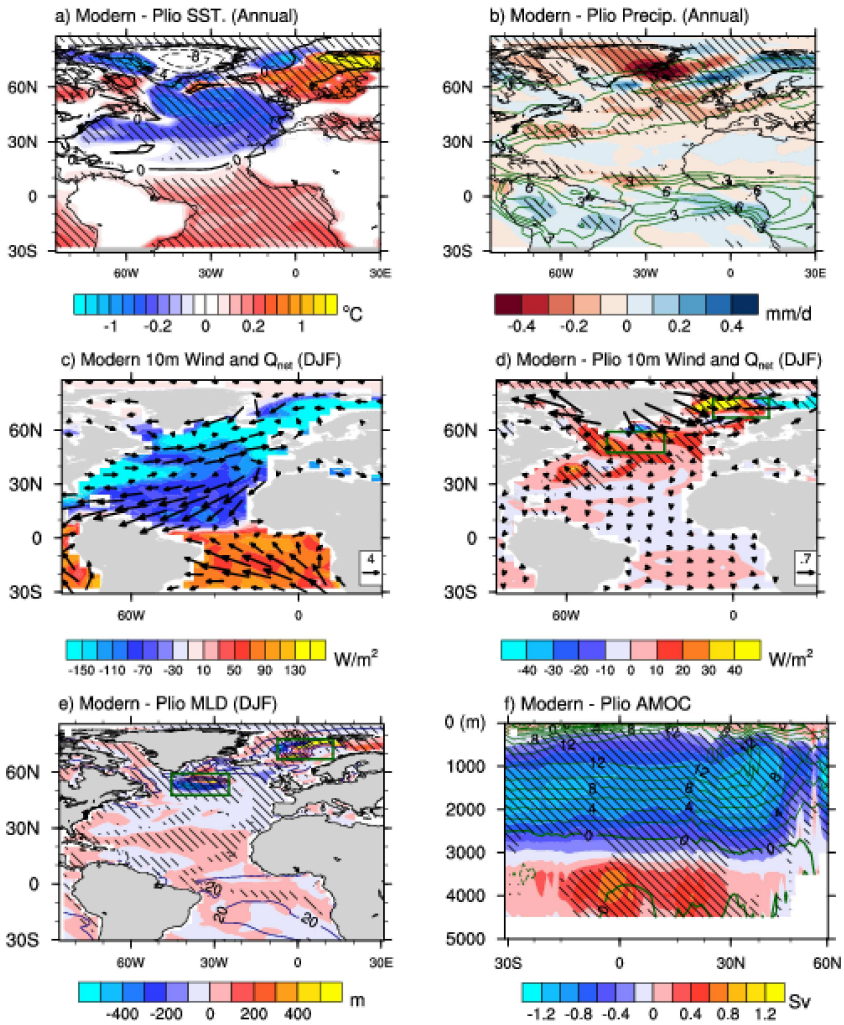

Figure 4.2: *(a) Differences (**Modern** minus **Plio**) of annual mean sea surface temperature (shading, unit: K) and T_{2m} (contours, interval: 2 K), (b) annual mean precipitation (contours, interval: 1.5 mm/day) and the difference (**Modern** minus **Plio**, shading, unit: mm/day), (c) climatological DJF mean 10-m wind vector (arrows, unit vector is 4 m/s) and net surface heat flux (shading, unit: W/m^2) for **Modern**, (d) differences (**Modern** minus **Plio**) of DJF mean 10-m wind (arrows, unit vector is 0.7 m/s) and net surface heat flux (shading, unit: W/m^2), (e) climatological DJF mean mixed layer depth (contours, interval: 400 m) and the difference (**Modern** minus **Plio**, shading, unit: m), (f) climatological mean Atlantic meridional overturning circulation (contours, interval: 2 Sv) and the difference (**Modern** minus **Plio**, shading, unit: Sv). Positive difference for the surface heat flux in (d) stands for reduced oceanic heat loss to the atmosphere and vice versa. The green boxes in (d) and (e) indicate the Irminger Sea and GIN (Greenland-Iceland-Norwegian) Sea, which are the two main convection regions in the KCM. Hatching indicates the differences are significant at the 99% confidence level using Student's t-test.*

4.3.2 Response to obliquity forcing

The beginning of the "41 ka world," revealed by reconstructed SST and $\delta^{18}O$ (Fig. 1.2), occurred around 2.7 Ma B.P. along with the onset of NHG including the expansion of the GrIS (Figures 1.2b and 1.2d; also see Fig.1 in *Ravelo et al.*, 2004). Obliquity variability does not impact the

annual-mean global insolation but affects the seasonal and meridional distribution of shortwave radiation at the top of the atmosphere (TOA). When the obliquity changes from high to low, insolation increases throughout the year at lower latitudes and generally increases (decreases) in winter (summer) at high latitudes (*Mantsis et al.*, 2011). However, the increased insolation in winter does not compensate for the reduced insolation in summer. The annual-mean insolation increase near the equator is about 2 W/m^2 and the annual-mean insolation decrease near the poles is about 12 W/m^2 (Fig. S4.8). Obliquity-forced insolation changes directly influence the surface temperature and its meridional gradient, and subsequently the zonally averaged atmospheric circulation. Here, we define the response of a selected variable to obliquity forcing as the difference between the annual-mean of that variable at low and high obliquity conditions. The zonal-mean surface temperature response is in good agreement with that in *Mantsis et al.* (2011) (Figures S4.9a and S4.9b). The expanded GrIS in **Modern** slightly enhances the T_{2m} response by about 0.03 K in the Northern Hemisphere mid-latitudes (not shown). However, due to the cold high pressure center in the North Atlantic sector, the background intrahemispheric meridional temperature gradient intensifies by 0.3 K, while the interhemispheric temperature gradient weakens by 0.28 K. The impact of the expanded GrIS on the thermal gradient is comparable to that of lower obliquity, which intensifies the near-surface zonal wind and zonal-mean atmospheric circulation response. Consistent with *Mantsis et al.* (2014), the simulated atmospheric response to decreased obliquity is an increase in the Northern Hemisphere mid latitude westerlies and tropical easterlies, which is linked to enhanced meridional insolation and pressure gradients (not shown).

The atmospheric meridional overturning streamfunction response to obliquity forcing (low minus high) depicts both an enhanced Hadley cell and Ferrel cell (Figures S4.9c and S4.9d). The ascending and descending branches of the Hadley circulation are associated with the ITCZ and subtropical dry regions, respectively (Figures S4.9c and S4.9d contours). The expansion of the GrIS in **Modern** amplifies the Hadley circulation response in both its ascending and descending branches south of the equator (Figures S4.9c and S4.9d shading). The intensified response of the descending branch is statistically significant at 99% level (Figures S4.9c and S4.9d hatching). As shown in Figures 4.3a and 4.3b, the response of the freshwater balance, defined as precipitation minus evaporation plus river runoff (P-E+R), is much stronger south of the equator in **Modern** relative to **Plio**, which is consistent with the Hadley circulation response (Fig. S4.9c,d). The net freshwater flux response integrated from 20°S to 20°N over the Atlantic amounts to -2.1 Sv and -1.4 Sv in **Modern** and **Plio**, respectively. We note that the P-E+R is dependent on the selection of the domain. We tested different domains, as a result of the expanded GrIS, and the response is always stronger in **Modern**, ranging from 0.1 Sv to 0.7 Sv.

Several model studies addressed the impact of freshwater export anomalies in the tropical Atlantic on the AMOC (e.g. *Latif et al.*, 2000; *Vellinga et al.*, 2004). All these studies suggest that the corresponding salinity anomalies propagate northward into the deep convection sites where they can influence the formation of North Atlantic Deep Water (NADW) and thus the AMOC. Some studies (e.g., *Peterson et al.*, 2000; *Latif*, 2001; *Schmittner et al.*, 2000) highlight the potential importance of atmospheric water vapor transport over the American continent for AMOC stability and climate variability. We calculate the Atlantic moisture export from our simulations by vertically integrating (from the surface to 200 hPa) the product of the zonal wind and specific humidity ($Q = \int_{200hPa}^{Surf} \bar{u}\bar{q}\frac{dp}{g}$, after *Lohmann* (2003) and *Lélé et al.* (2015)). Its response to obliquity forcing integrated from 20°S to 20°N (Figures 4.3c and 4.3d) amounts

to 0.1 and 0.07 Sv for **Modern** and **Plio**, respectively. The increased freshwater export due to the expanded GrIS in **Modern** eventually enhances the obliquity-forced response of AMOC by about a factor of 2 (1.1 Sv for **Modern** as opposed to 0.6 Sv for **Plio**, Figures 4.3e and 4.3f). We do not expect a perfect response-magnitude match of the tropical Atlantic freshwater export and AMOC strength due to the differences in contributions from sea ice and surface heat flux as well as the selection of the integration domain.

Heat transport changes associated with the AMOC modulate the Northern Hemisphere T_{2m} response to obliquity forcing. For example, 7 out of 12 models participating in the Coupled Model Intercomparison Project Phase 5 (CMIP5; *Taylor et al.*, 2012) produce a significant positive linear regression between AMOC strength and T_{2m} (Fig. S4.10), and only two models exhibit a significant negative regression. The enhanced AMOC response intensifies the North Atlantic (0°-60°N, 80°-20°W) T_{2m} response from 0.24 K in **Plio** to 0.36 K in **Modern**, the Northern Hemisphere T_{2m} response (defined as the difference between the multi-century (600 years) annual mean of T_{2m} at low- and high- obliquity conditions) from 0.31 K in **Plio** to 0.40 K in **Modern**, and the global-mean T_{2m} response from 0.16 K in **Plio** to 0.28 K in **Modern**.

4.4 Summary and discussion

We have investigated by means of a set of experiments with the KCM the impact of GrIS expansion on the mean surface climate and AMOC. Specially, the influence of the GrIS on the climate response to obliquity forcing (41 kyr) has been investigated to understand the strengthening obliquity signal during the Plio-Pleistocene transition. We find that the expanded GrIS weakens near-surface westerly winds south of Greenland and near-surface easterly winds over the GIN Sea, which damps deep oceanic convection in these regions by reducing heat loss to the atmosphere. Accordingly, AMOC strength weakens by about 1 Sv and induces cooling of 0.15 K in the North Atlantic averaged over the region 40°N-60°N. Sea-ice fraction increases following the cooling, which further reduces the air-sea heat exchange. Therefore, the expanding GrIS affects the AMOC through a positive ocean-atmosphere-sea ice feedback. Our result is consistent with the results from PlioMIP (*Zhang et al.*, 2013b), which show small changes in the AMOC between mid-Piacenzian and modern times. The orographic impact of the GrIS on the AMOC is within the range of the internal variability (2σ) but is statistically significant. The SST cooling following the buildup of the GrIS is rather weak compared to the SST change estimated from North Atlantic Sites ODP 982 (Fig. 1.2a) and Deep Sea Drilling Project (DSDP) 607 of about 3 K (*Lawrence et al.*, 2010). This suggests the importance of additional drivers during the Plio-Pleistocene transition such as the closure and opening of Bering and Canadian Archipelago Straits, and the emergence of the modern West and East Antarctic Ice Sheet (*Brierley and Fedorov*, 2016; *Otto-Bliesner et al.*, 2017; *Hill et al.*, 2017). The opening of both Bering and the Canadian Archipelago Straits is linked to a 1.3 K SST cooling in the North Atlantic (*Otto-Bliesner et al.*, 2017), while the glaciation over West and East Antarctic supports a deep ocean cooling of 2.0 K reconstructed at Site DSDP 607 (*Hill et al.*, 2017). The model-data discrepancy in this study would likely be smaller if these changes in land surface and land sea distribution were included in simulations.

We also investigated the role that the expanded GrIS could have played in enhancing the climate response to obliquity forcing (41 kyr). In general, when the obliquity moves from high to low, the Northern Hemisphere intrahemispheric meridional insolation gradient strengthens,

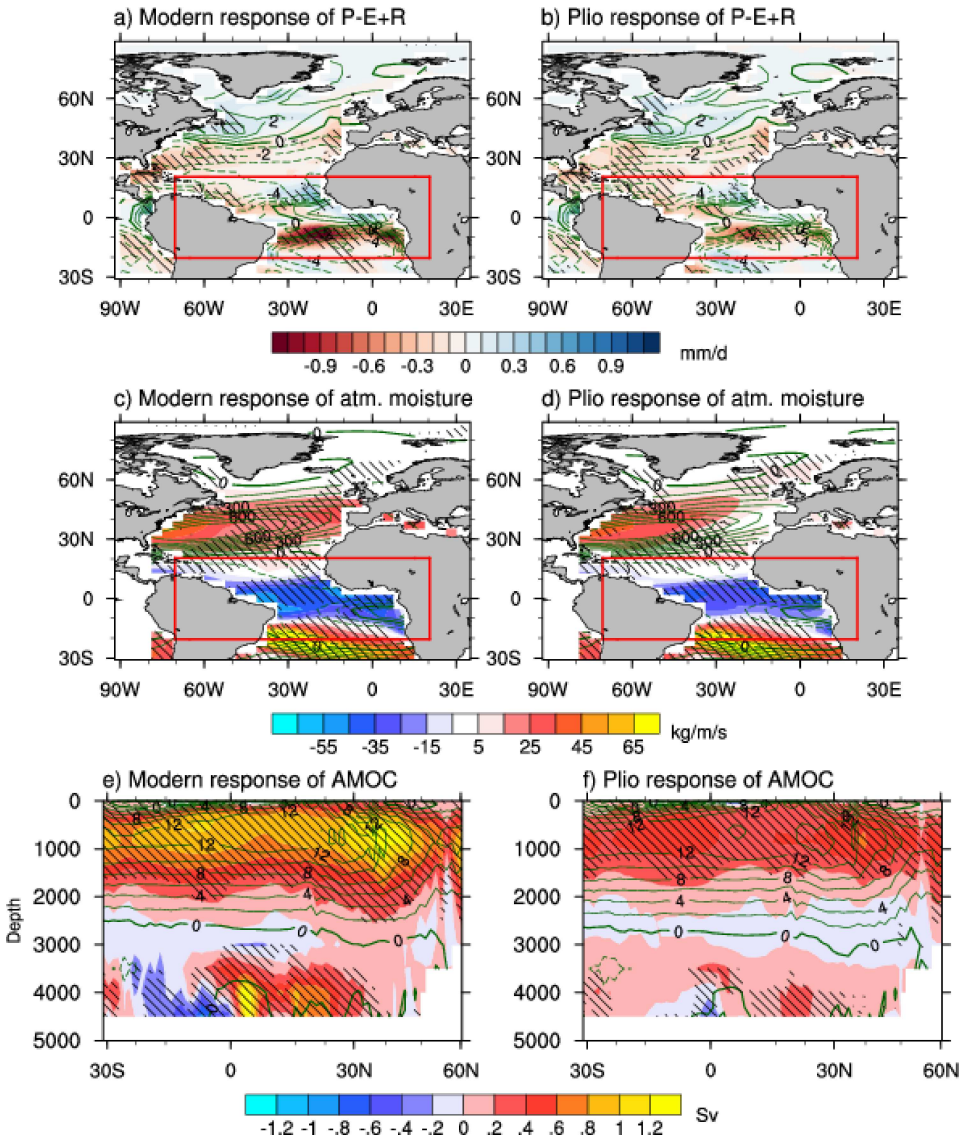

Figure 4.3: *(a, b) Responses of precipitation - evaporation + river runoff (P-E+R) balance (shade; mm/day) to obliquity variation (Low minus High) for* ***Modern*** *(a) and* ***Plio*** *(b). Green contours show climatological mean P-E+R balance (contour interval: 1 mm/day) for* ***Modern*** *(a) and* ***Plio*** *(b). Negative (dashed contour) P-E+R balance indicates the ocean exports fresh water and vice versa. (c, d) Responses of vertically integrated (from the surface to 200 hPa) water vapor transport (shade; $kg \cdot m^{-1} \cdot s^{-1}$) for* ***Modern*** *(c) and* ***Plio*** *(d). Green contours show climatological mean atmospheric moisture transport (contour interval: 100 $kg{\cdot}m^{-1}{\cdot}s^{-1}$) for* ***Modern*** *(c) and* ***Plio*** *(d). Negative (dashed contour) atmospheric moisture transport indicates the water vapor is transported from the Atlantic to the Pacific. (e, f) Responses of AMOC (shade; Sv) for* ***Modern*** *(e) and* ***Plio*** *(f). Green contours show climatological mean AMOC (contour interval: 2 Sv) for* ***Modern*** *(e) and* ***Plio*** *(f). Hatching indicates the differences are significant at the 99% confidnce level using Student's t-test.*

while the interhemispheric meridional insolation gradient weakens (*Mantsis et al.*, 2014). An expanding GrIS leads to similar influences in the KCM because of the influence of elevation and albedo: the intrahemispheric temperature gradient strengthens by 0.3 K and the interhemi-

spheric temperature gradient weakens by 0.28 K. The response of the zonal-mean atmospheric circulation to obliquity forcing intensifies with the expanded GrIS. In turn, the obliquity-forced variation of the AMOC strengthens by about a factor of two, which is due to enhanced net freshwater export from the tropical Atlantic, especially south of the equator, subsequently leading to enhanced surface air temperature variability.

The key mechanism driving the enhanced climate variability in our simulations can be summarized as Northern Hemisphere extratropical cooling initiated by the expanding GrIS, which drives stronger responses of freshwater flux to obliquity forcing in the Atlantic ITCZ region (*Chiang and Bitz*, 2005; *Broccoli et al.*, 2006). The involvement of the ITCZ and tropical freshwater flux can be a crucial element, as previously found in the KCM in response to idealized solar forcing (*Park and Latif*, 2012). Our results support the connection between NHG and enhanced climate variability at the obliquity frequency, providing support to the notion that the sensitivity of Earth's climate to change in radiative forcing depends on the background climate (*Caballero and Huber*, 2013). However, the simulated response of surface temperature to obliquity forcing is much weaker compared to that inferred from proxy data. We note that the climate sensitivity depends on both slow "Earth system" feedbacks, which are related to the boundary conditions and fast feedbacks that are related to internal processes linked to, for example, water vapor content or sea ice. Our simulations only consider the orographic impact of the GrIS, one of the slow climate feedbacks. However, the simulations lack a carbon cycle feedback that likely leads to the underestimation of the climate response, as suggested by *Martínez-Botí et al.* (2015). Further, the climate sensitivity is also strongly influenced by the positive ice-albedo feedback. As the ice sheet mask is fixed in the KCM, the ice-albedo feedback is not included either. The uncertainty of the GrIS configuration during the mid-Piacenzian (*Dolan et al.*, 2015) also constrains our results . The influence of the ice sheets over North America and Europe (*Bintanja and van de Wal*, 2008) is not accounted for in our experiments with the KCM. Additionally, the opening of Arctic oceanic gateways and ice sheets over West and East Antarctic is not considered and may further weaken the interhemispheric temperature gradient (*Brierley and Fedorov*, 2016; *Otto-Bliesner et al.*, 2017; *Hill et al.*, 2017). *Knies et al.* (2014) suggested the gradual emergence of modern Arctic sea ice, which may also provide a freshwater forcing on the AMOC. We do not claim that our findings fully explain the increased climate variability at the obliquity frequency during the Plio-Pleistocene transition interpreted from the geologic record, but suggest that topographic changes of the Greenland ice sheet were a contributor. Our results suggest that slow feedbacks related to changing boundary conditions may also be important in amplifying obliquity frequency climate variability.

Acknowledgments

The suggestions of the two anonymous referees greatly improved an earlier version of the manuscript. This study was supported by the Excellence Cluster "The Future Ocean" at Kiel University sponsored by the German Science Foundation (DFG) and the PalMod project (01LP1503D) sponsored by the German Ministry of Education and Research (BMBF). We thank Edmund Hathorne for his helpful comments and Gerrit Lohmann and Xu Zhang for their assistance with the subgrid-scale orography parameterization for Greenland in the PRISM4 data set. The simulations with the Kiel Climate Model (KCM) were conducted at the Computing Center of Kiel University. The KCM results presented in this study are available at Pangaea (https://doi.pangaea.de/10.1594/PANGAEA.877918). Requests for other data should be directed to wpark@geomar.de. Zhaoyang Song is a Ph.D. student, sponsored by the China

Scholarship Council (CSC).

Supplemental figures

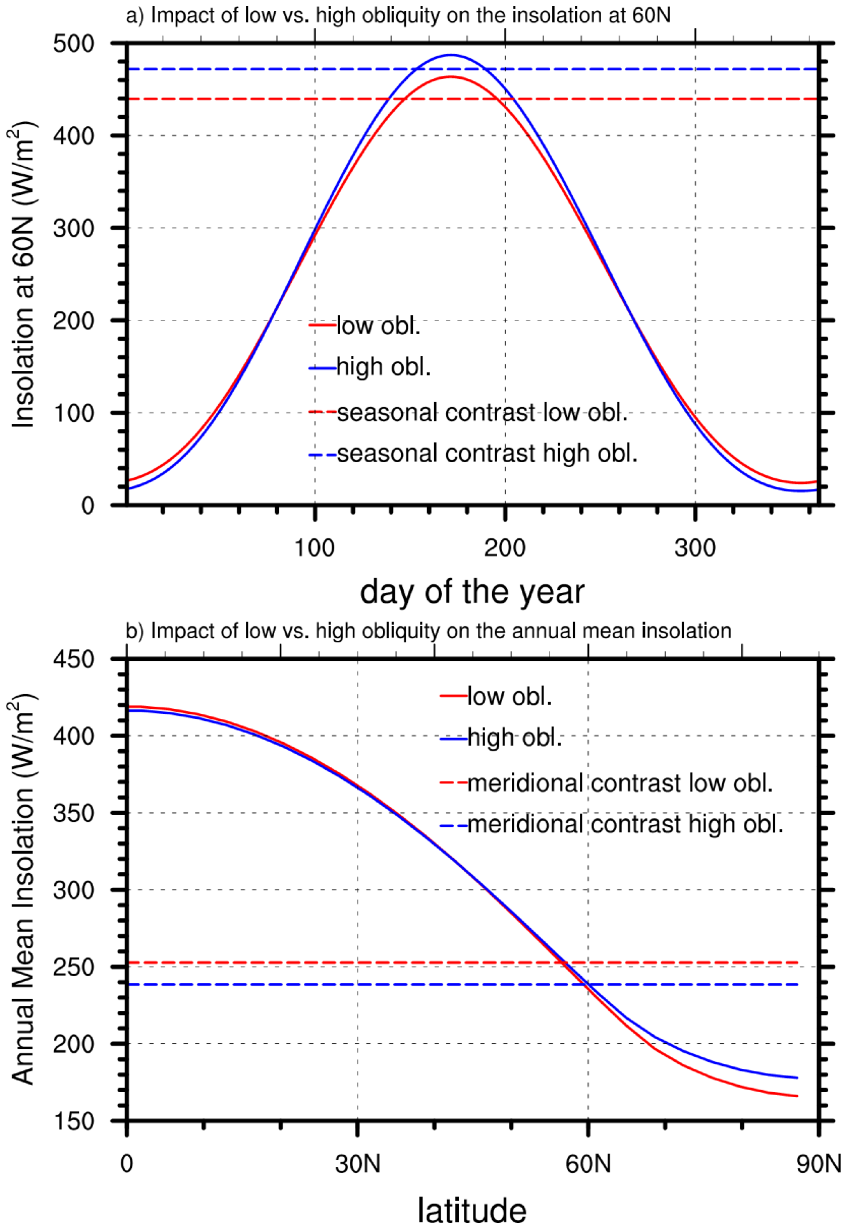

Figure S4.1: *Impact of low and high obliquity on the insolation distribution. (a) Impact on the insolation at 60°N during the calendar year, and on the seasonal insolation contrast (defined as the difference between the maximum and minimum of annual insolation). (b) Impact on the annual-mean Northern Hemisphere insolation as function of the latitude, and on the meridional insolation contrast (defined as the difference between the maximum and minimum of meridional insolation). The low and high obliquity is 22.34° and 24.05° , respectively. The insolation is calculated after the VSOP87 solutions (Bretagnon and Francou, 1988) that are used in the KCM.*

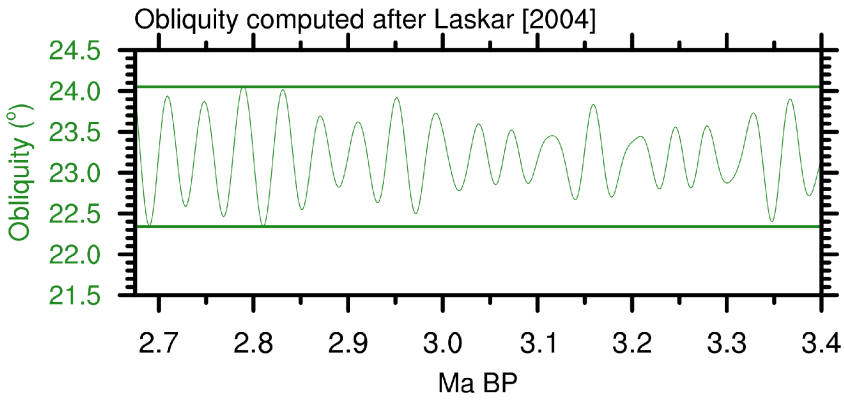

Figure S4.2: *Obliquity for Plio-Pleistocene computed after Laskar et al. (2004). The temporal resolution is 1,000 years. The two horizontal lines indicate the minimum (22.34°) and maximum (24.05°).*

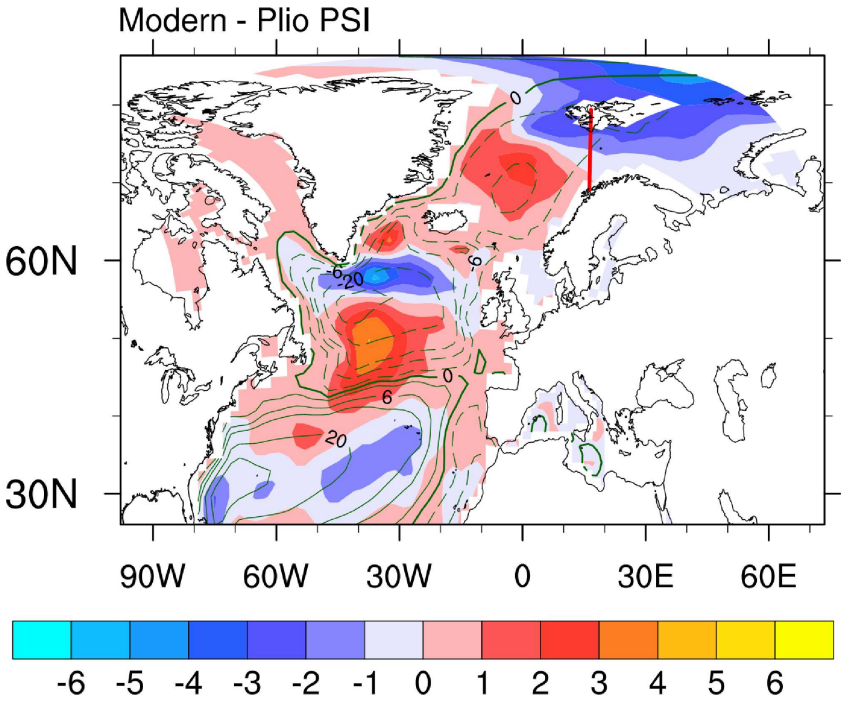

Figure S4.3: *Differences (**Modern** minus **Plio**) of the barotropic stream function (shading, unit: Sv), and the stream function climatology for **Modern** (contours, contour levels: [-30, -20, -10, -6, -2, 0, 2, 6, 10, 20, 30]). Solid contours and positive anomalies (red) indicate clockwise circulation. The red line represents the transection from Svalbard to Norway.*

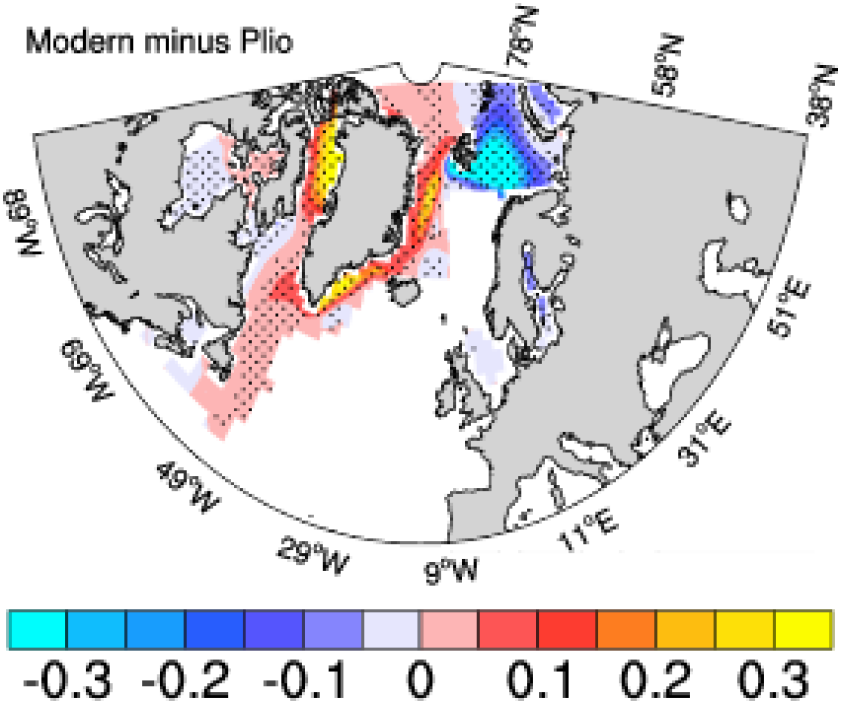

Figure S4.4: *Differences (**Modern** minus **Plio**) of annual mean sea ice fraction (from 0 to 1). Stippling indicates the differences are significant at the 99% confidence level using Student's t-test.*

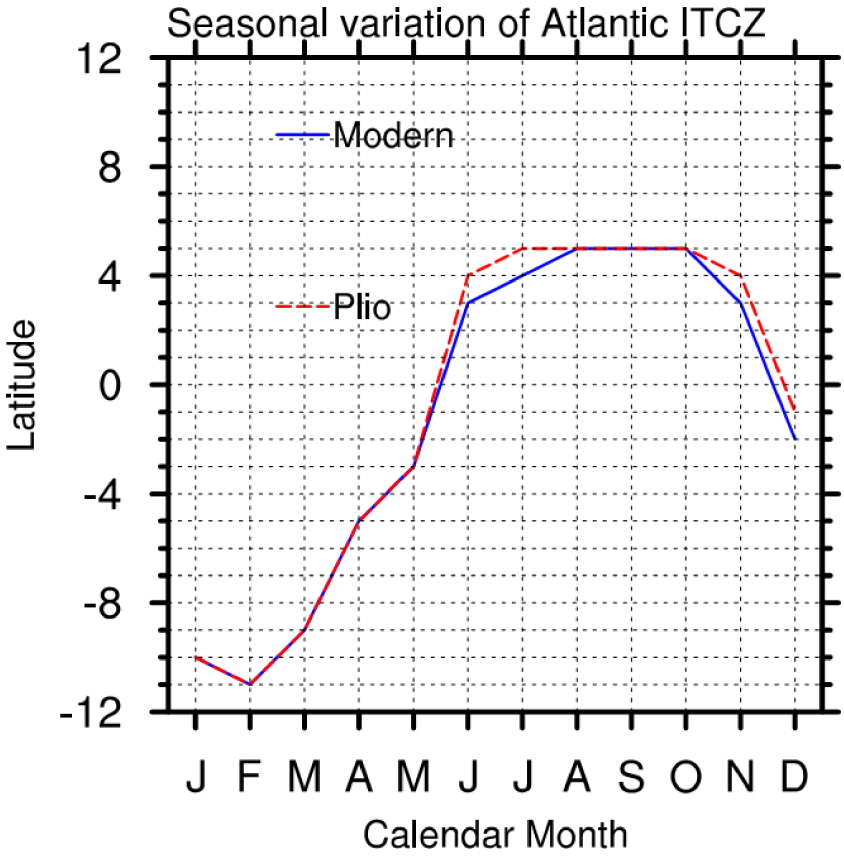

Figure S4.5: *Seasonal variation of the Atlantic ITCZ. ITCZ location is defined as the latitude of maximum precipitation averaged from 45°W – 0°, following Hu et al. (2007).*

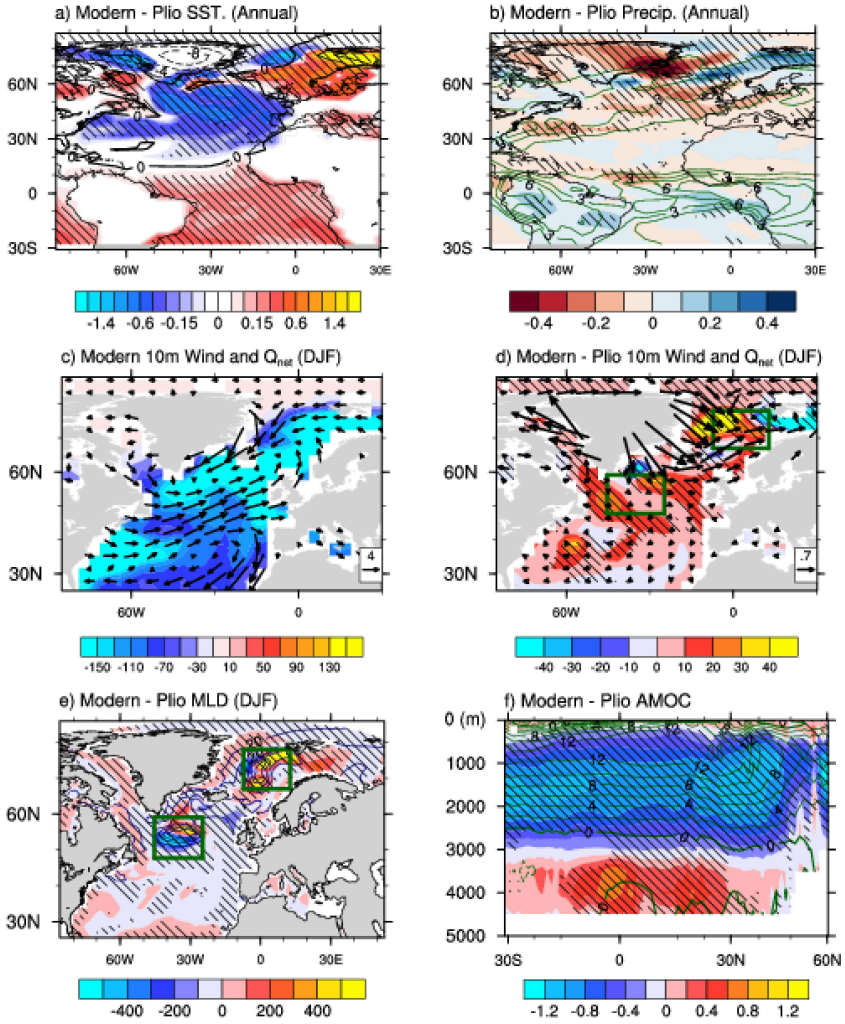

Figure S4.6: *(a) Differences (**Modern** minus **Plio**) of annual mean sea surface temperature (shading, unit: K) and T_{2m} (contours, interval: 2 K), (b) annual mean precipitation (contours, interval: 1.5 mm/day) and the difference (**Modern** minus **Plio**, shading, unit: mm/day), (c) climatological DJF mean 10-m wind vector (arrows, unit vector is 4 m/s) and net surface heat flux (shading, unit: W/m^2) for **Modern**, (d) differences (**Modern** minus **Plio**) of DJF mean 10-m wind (arrows, unit vector is 0.7 m/s) and net surface heat flux (shading, unit: W/m^2), (e) climatological DJF mean mixed layer depth (contours, interval: 400 m) and the difference (**Modern** minus **Plio**, shading, unit: m), (f) climatological mean Atlantic meridional overturning circulation (contours, interval: 2 Sv) and the difference (**Modern** minus **Plio**, shading, unit: Sv). Positive difference for the surface heat flux in (d) stands for reduced oceanic heat loss to the atmosphere and vice versa. The green boxes in (d) and (e) indicate the Irminger Sea and GIN (Greenland-Iceland-Norwegian) Sea, which are the two main convection regions in the KCM. Hatching indicates the differences are significant at the 99% confidence level using Student's t-test.*

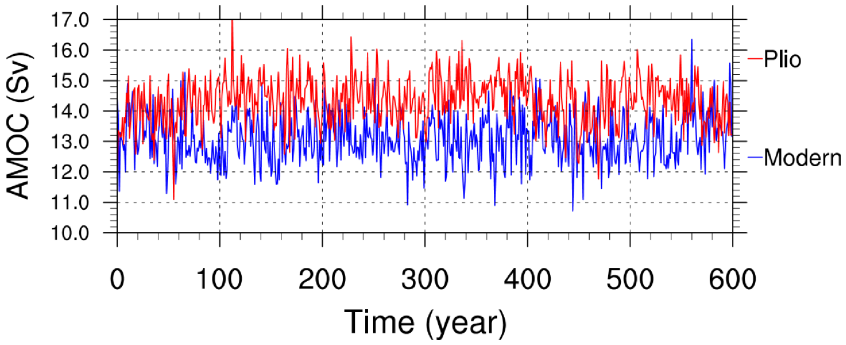

Figure S4.7: *Time series of AMOC indices for* ***Modern*** *and* ***Plio****. The AMOC index is defined as the maximum streamfunction at 30°N.*

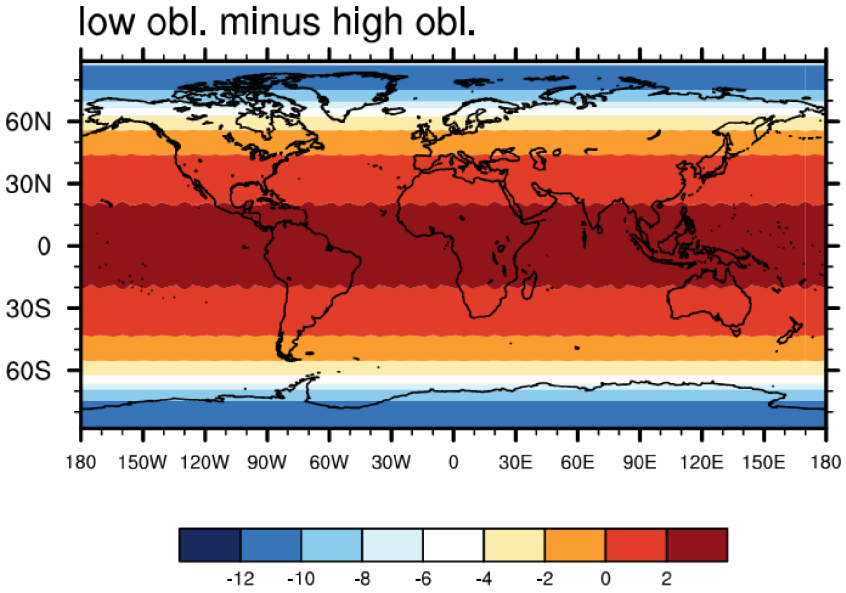

Figure S4.8: *Difference (low obliquity minus high obliquity) in annual-mean solar radiation (Unit: W/m^2) at the top of the atmosphere.*

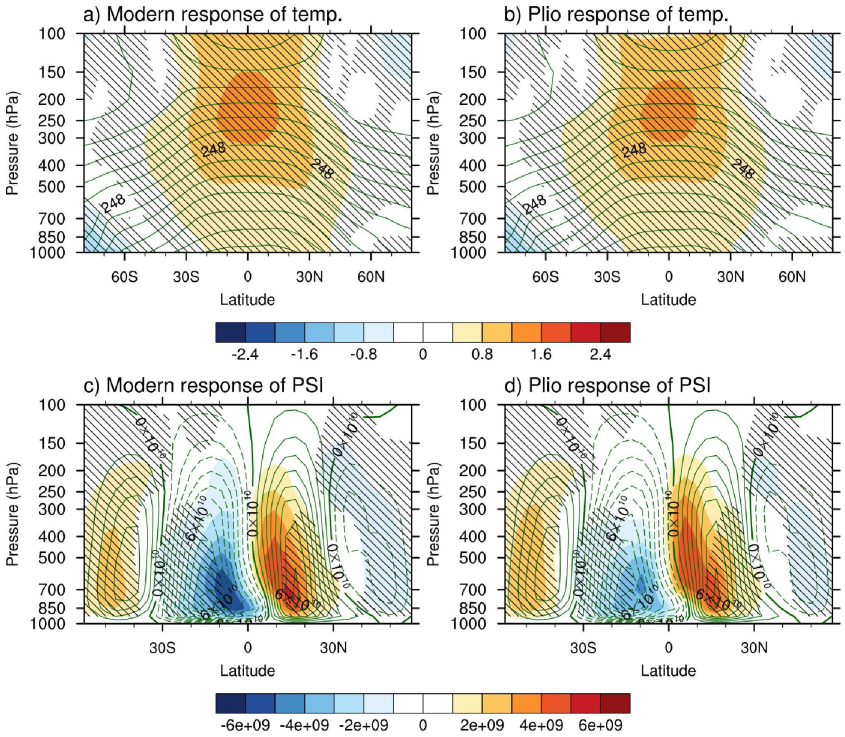

Figure S4.9: *(a, b) Responses of zonal mean temperature (shade; K) to obliquity variation (Low minus High) for* ***Modern*** *(a) and* ***Plio*** *(b). Green contours show climatological mean zonal mean temperature (contour interval: 4 K) for* ***Modern*** *(a) and* ***Plio*** *(b). (c, d) Responses of meridional streamfunction (shade; kg/s) for* ***Modern*** *(c) and* ***Plio*** *(d). Green contours show climatological mean meridional streamfunction (contour interval: 10^{10} kg/s) for* ***Modern*** *(c) and* ***Plio*** *(d). Dashed contours indicate anti-clockwise circulation, while solid contours indicate clockwise circulation. Hatching indicates the differences are significant at the 99% confidence level using Student's t-test.*

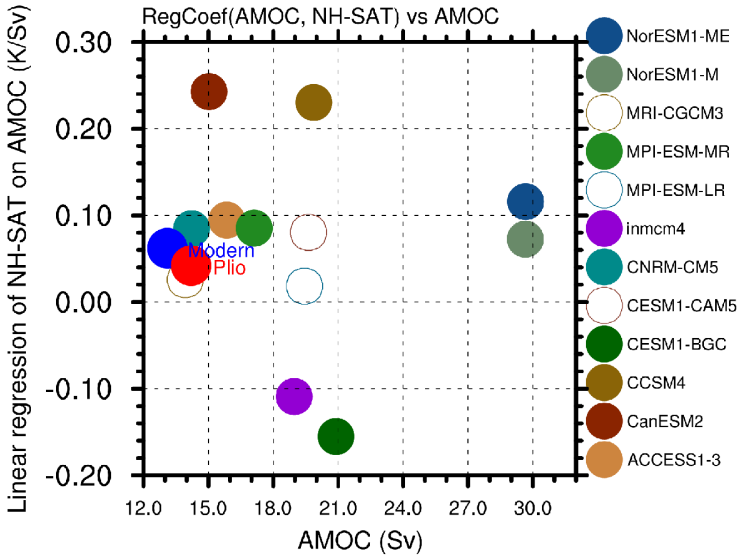

Figure S4.10: *Linear regression coefficients (Unit: K/Sv, 1 Sv = 10^6 m^3/s) of averaged Northern Hemisphere (0° - 90°N) T_{2m} (2m-air-temperature) on annual mean Atlantic Meridional Overturning Circulation (AMOC) index (defined as the maximum barotropic streamfunction at 30°N) as function of AMOC index for the Coupled Model Intercomparison Project Phase 5 (CMIP5) models. Prior to linear regression, AMOC and averaged Northern Hemisphere T_{2m} are smoothed with a 11-year running mean. Positive coefficients indicate that warmer Northern Hemisphere T_{2m} is related to stronger AMOC. The simulations are the CMIP5 historical runs analyzed from the year 1850 to 1949 (Taylor et al., 2012). The regression coefficients for* ***Modern*** *and* ***Plio*** *are computed using 600-year monthly mean output. Solid dots indicate that the regression coefficients are significant at the 95% confidence level.*

Chapter 5

Conclusions

This thesis addresses the impacts of changes in atmospheric CO_2-concentration, oceanic seaways and Greenland ice sheet (GrIS) on the Pliocene climate and its evolution towards the present-day condition. The majority of the present work is based on three sets of model sensitivity experiments with the Kiel Climate Model (KCM), which differ in the geometry of the Indonesian Passages, the Panama Seaway, the orography and ice sheet mask of GrIS and atmospheric CO_2-concentration. Additionally, multiple geological reconstructions have been used to verify the model results and enhance our understanding of the Pliocene climate.

In this context, model sensitivity of large-scale climate features to CO_2 and seaway changes were quantitatively examined in chapter 2, by comparison with 95 globally distributed sea surface temperature (SST) reconstructions for the mid-Pliocene (3.264–3.025 Ma BP). In addition, the responses of the East Asian summer monsoon (EASM) was investigated with model simulations and validated by multiple paleogeochemical records during the Pliocene. Further, special attention was given to the tropical Pacific mean-state and annual cycle responses, and responses in the El Niño/Southern Oscillation (ENSO), which plays a crucial role in determining the causes and characteristics of paleoclimate evolution. Additionally, within the recharge oscillator framework, a Bjerknes stability analysis was conducted to quantitatively assess changes in ocean-atmosphere feedbacks and ENSO dynamics in the KCM. In chapter 4, the impact of GrIS on the sensitivity of Plio-Pleistocene climate to obliquity forcing was investigated. To this end, a set of six sensitivity experiments with differing GrIS and obliquity forcing were analyzed.

5.1 Summary

Here, we summarize the results and conclusions by revisiting the questions posed in the introduction.

1. What are the model sensitivities to seaway and CO_2 changes with respect to the large-scale features and East Asian summer monsoons during the Pliocene?

With regard to this question, a set of four sensitivity experiments is conducted to investigate the individual impact of declining CO_2, the restriction of the Indonesian Passages and the final closure of the Panama Seaway on the mean climate and EASM. For the global mean SST, the model is more sensitive to declining CO_2 than to the seaway changes. The model

sensitivity to lower CO_2 is within the range as suggested by the proxies. As for the regional scale comparison, the simulated SST response to CO_2 agrees reasonably well with proxies in the Southern Hemisphere and the Tropics. However, the KCM substantially underestimates the magnitude of SST response in the North Atlantic and Arctic. Neither of the seaways changes improves the model-proxy discrepancy in the northern high latitudes, due to the rather weak response of meridional oceanic and atmospheric heat and moisture transport associated with the meridional circulation. The impacts of the seaway changes are largely confined within the Tropics. Consistent with precious study, the glaciation over Greenland is controlled by the declining CO_2, while the restriction of two seaways slightly slows down the glaciation.

The intensity of EASM significantly strengthens in response to lower CO_2, however, the precipitation averaged over the monsoon region decreases. A water vapor budget analysis suggests that the precipitation response is largely attributed to the reductions in spatially averaged specific humidity. The restriction of two seaways slightly weakens the intensity of EASM, yet the spatially averaged precipitation response is rather weak, albeit significant according to a Student's t-test. The reasons are twofold. First, the specific humidity reduces barely in response to seaway changes. Second, reduced precipitation over east China is largely compensated by the increased precipitation over the west Pacific. Therefore, the precipitation response averaged over the monsoon region is quite weak.

2. What are the influences of seaway and CO_2 changes during the Pliocene on tropical pacific climate with respect to mean sate, annual cycle, ENSO, and their Interactions?

Related to this question, a set of eight sensitivity simulations with the KCM was conducted. Special attention was paid to closing a deep Panama Seaway and to narrowing the Indonesian Passages. Closing the Panama Seaway in the KCM strongly modifies the tropical Pacific climatology. We observe shoaling of the thermocline across the tropical Pacific and strengthening of the southerly wind stress in the east, where the latter is forced by an enhanced meridional SST gradient. A slightly decreased zonal equatorial SST gradient and zonal wind stress, indicating ocean-atmosphere coupling, is also simulated in the eastern equatorial Pacific. The strongly enhanced southerly wind stress simulated in response to the closing of the Panama Seaway is the most important factor strengthening the annual cycle. The changes in the Indonesian Passages have less impact. Narrowing the Indonesian Passages deepens the thermocline depth and strengthens the southerly wind stress slightly. The annual cycle slightly enhances along with the southerly wind stress.

The simulated ENSO is robust across all sensitivity experiments. ENSO amplitude decreases in response to closing the Panama Seaway and increases in response to narrowing the Indonesian Passages. Lower atmospheric CO_2 reduces ENSO amplitude. The dominant ENSO period does not significantly change in the experiments.

The Bjerknes stability analysis is applied to assess responses in ocean-atmosphere feedbacks and ENSO dynamics. The Bjerknes index, which sums three positive and two negative feedbacks, illustrates relatively small changes across the experiments albeit large diversity in the individual positive and negative feedbacks, which is consistent with the small but statistically significant changes in ENSO amplitude and modest changes in ENSO period. An increase of the Bjerknes index is accompanied by larger ENSO amplitude and vice versa. In all experiments, dynamical damping and thermocline feedback are the dominant negative and positive feedbacks, respectively. We also find that weakening of positive feedbacks is largely compen-

sated by reduced dynamical damping and vice versa. As a result, ENSO behavior is relatively stable across the set of experiments.

3. How does the expansion of Greenland ice sheet enhance sensitivity of Pliocene-Pleistocene climate to obliquity forcing?

To this end, we have investigated the impact of GrIS expansion on the mean surface climate and AMOC with the KCM. Furthermore, the influence of the GrIS on the amplifying Plio-Pleistocene climate response to obliquity forcing (41 ka) has been investigated. The expanded GrIS weakens simulated 10 m easterly winds over the GIN Sea, and 10 m westerly winds south of Greenland to a lesser extent, which damps oceanic convection in these regions by reducing heat loss to the atmosphere. Accordingly, AMOC strength slightly weakens and induces cooling in the North Atlantic (40°N-60°N). However, the simulated SST cooling due to the GrIS expansion is rather weak compared to the SST proxies, which suggests the insolvent of other important drivers during the Plio-Pleistocene transition.

We also find that the GrIS expansion could have enhanced the climate response to obliquity forcing (41 ka). When the obliquity moves from high to low, the Northern Hemisphere intra-hemispheric meridional insolation gradient strengthens while the interhemispheric meridional insolation gradient weakens. An expanded GrIS illustrates similar influences in the KCM due to the uplifted elevation, and enhanced albedo to a lesser extent. Therefore, the response of the zonal-mean atmospheric circulation to obliquity forcing intensifies with the expanded GrIS. In turn, the response of AMOC to obliquity forcing strengthens by about a factor of 2, which is due to enhanced net freshwater export from the tropical Atlantic, especially south of the equator, subsequently leading to enhanced surface air temperature response.

Our results support the connection between Northern Hemisphere Glaciaiton and enhanced climate variability to obliquity forcing. The extratropical cooling in the Northern Hemisphere initiated by the GrIS expansion drives the changes in the sensitive ITCZ region, and subsequently the global mean surface climate response to obliquity forcing. However, the simulated response of surface temperature to obliquity forcing is much weaker compared to that inferred from proxy data. Although the primary driver for glacial-interglacial cycle is orbitally forced changes in insolation, the atmospheric CO_2-concentration is crucial for the full magnitude of temperature variation. Therefore, the lack of a carbon cycle and an interactive ice sheet are attributed to such underestimation of the climate response.

5.2 Outlook

This thesis presents three sets of sensitivity experiments as well as palaeoenvironmental reconstructions to investigate the responses of mean surface climate, ENSO variability and climate response to external insolation forcing (obliquity). However, quantitative model-data discrepancies still exist, which opens new perspectives for studies on (a) the strengths, weaknesses and limitations of climate models, (b) uncertainties in boundary conditions employed in climate models and (c) uncertainties and interpretations of proxy data.

We showed in chapter 2 that large model-data discrepancies exist in the North Atlantic and Arctic with respect to SST. Study (*Huber and Caballero*, 2011) has shown that climate models underestimate the strength of polar amplification by 30% to 50% for simulating warm

period. Water vapor and cloud feedbacks have been suggested to be important for amplifying northern high-latitudes climate change (*Abbot and Tziperman*, 2008; *Graversen and Wang*, 2009). Other missing or unresolved processes, such as positive vegetation-sea ice feedback (*Bhatt et al.*, 2010), cloud albedo (*Burls and Fedorov*, 2014), atmospheric chemistry-climate feedback (*Unger and Yue*, 2014) and ocean eddies (*Viebahn et al.*, 2016) may also be relevant. We have shown in chapter 4 that GrIS expansion enhances climate response to obliquity forcing during the Plio-Pleistocene transition. However, the simulated response is much weaker compared to the proxies. Although the changes in insolation are the primary driver for glacial-interglacial cycles, studies (*Lisiecki*, 2010; *Huybers*, 2011) show that atmospheric CO_2 concentration plays an important role in explaining the magnitude of temperature response. Therefore, further research with interactive carbon cycle may provide further insight into gradually enhanced climate variability to obliquity forcing during the Plio-Pleistocene transition. The large cold bias of the KCM in the North Atlantic may be another source for the rather weak climate response to seaway changes. As shown by *Park et al.* (2016), improved simulation of the mean circulation in the North Atlantic significantly enhances the mean climate and decadal variability. By improving the simulation of the mean circulation in the North Atlantic sector, climate responses to seaway changes can be more realistically investigated.

The land-ocean configuration for the Pliocene remains highly uncertain. The Pliocene Model Intercomparison Project (PlioMIP) provides reconstructed land-ocean boundary condition with an open Bering Strait in earlier version (*Dowsett et al.*, 2012), but closing recently (*Haywood et al.*, 2016). This closed Bering Strait has been suggested to reduce the model-data discrepancies in the northern high-latitudes (*Otto-Bliesner et al.*, 2017). Additionally, *Hill* (2015) investigates the impacts of changes in Greenland-Scotland Ridge and Barents Sea on the AMOC and North Atlantic climate. These changes may not strongly affect the global mean SST, but may influence the North Atlantic and Arctic. Moreover, the aforementioned changes in boundary condition may alter the earth system sensitivity and enhance our understanding of the question addressed in chapter 4.

Improved interpretation for proxies may contribute to reduced model-data disagreement. In the northern high-latitudes, large uncertainties among different types of proxy data may be attributed to warming and seasonally ice-free conditions. A proxy-proxy comparison over the Benguela upwelling region suggests that the Mg/Ca and alkenone SST proxies are strongly skewed toward cold and warm seasons, respectively (*Leduc et al.*, 2014). A successful application for the KCM is by *Schneider et al.* (2010), which suggests the alkenone-based SST agrees wellwith summer SSTs. Model results can be applied to improve the interpretation of proxy date in future work. Moreover, orbitally forced changes in seasonal, latitudinal and annual mean distribution of insolation may be significant and different from one time-interval to another. Therefore, the selection of time interval and improved interpretation for different proxies is crucial for model-data comparison in future work.

Last but not least, non-linear interactions among oceanic seaways and other boundary conditions should be considered. In chapter 3, we treat the changes in Indonesian Passages and the Panama Seaway individually and combined, yet there is not much non-linearity between these two. However, *Hill* (2015) found the non-linear interactions among the Greenland-Scotland Ridge, landmass in the Barents Sea and North America river routines, which nearly compensates for each other's influences on the AMOC and mean surface climate in the North Atlantic. *Otto-Bliesner et al.* (2017) suggests the non-linear interaction between the closing Bering and

closing Canadian Archipelago Straits on enhancing the AMOC. In future study, it is important to careful evaluate the possible non-linear interactions among a number of boundary conditions in climate evolution.

Author Contributions

The author contributions to the main chapters 2, 3 and 4 are the following:
Zhaoyang Song designed the experiments in chapter 4, performed all analysis, produced all figures and wrote the manuscripts.
Mojib Latif contributed with ideas and discussions on the analysis, and comments on the manuscripts.
Wonsun Park also contributed to chapters 3 and 4 with ideas, experimental setup and discussions on the analysis, and comments on the manuscript.
Uta Krebs-Kanzow co-designed the experiments in chapters 2 and 3, and contributed discussions to chapter 3.
Birgit Schneider contributed discussions to chapter 3.

List of Figures

List of Tables

Bibliography

Abbot, D. S., and E. Tziperman (2008), A high-latitude convective cloud feedback and equable climates, *Quarterly Journal of the Royal Meteorological Society*, *134*(630), 165–185, doi:10.1002/qj.211.

Alexander, M. A., I. Bladé, M. Newman, J. R. Lanzante, N. C. Lau, and J. D. Scott (2002), The atmospheric bridge: The influence of ENSO teleconnections on air-sea interaction over the global oceans, *Journal of Climate*, *15*(16), 2205–2231, doi:10.1175/1520-0442(2002)015<2205:TABTIO>2.0.CO;2.

An, S.-I., and J. Choi (2013), Inverse relationship between the equatorial eastern pacific annual-cycle and enso amplitudes in a coupled general circulation model, *Climate dynamics*, *40*(3-4), 663–675, doi:10.1007/s00382-012-1403-3.

An, Z., J. E. Kutzbach, W. L. Prell, and S. C. Porter (2001), Evolution of Asian monsoons and phased uplift of the Himalaya-Tibetan plateau since Late Miocene times., *Nature*, *411*(6833), 62–66, doi:10.1038/35075035.

Anderson, D. L. T., J. P. McCreary, D. L. T. Anderson, and J. P. McCreary (1985), Slowly Propagating Disturbances in a Coupled Ocean-Atmosphere Model, *Journal of the Atmospheric Sciences*, *42*(6), 615–630, doi:10.1175/1520-0469(1985)042<0615:SPDIAC>2.0.CO;2.

Bailey, I., G. M. Hole, G. L. Foster, P. A. Wilson, C. D. Storey, C. N. Trueman, and M. E. Raymo (2013), An alternative suggestion for the Pliocene onset of major northern hemisphere glaciation based on the geochemical provenance of North Atlantic Ocean ice-rafted debris, *Quaternary Science Reviews*, *75*, 181–194, doi:10.1016/j.quascirev.2013.06.004.

Bamber, J. L., R. L. Layberry, and S. P. Gogineni (2001), A new ice thickness and bed data set for the Greenland ice sheet: 1. Measurement, data reduction, and errors, *Journal of Geophysical Research: Atmospheres*, *106*(D24), 33,773–33,780, doi:10.1029/2001JD900054.

Bartoli, G., B. Hönisch, and R. E. Zeebe (2011), Atmospheric CO2 decline during the Pliocene intensification of Northern Hemisphere glaciations, *Paleoceanography*, *26*(4), doi:10.1029/2010PA002055.

Bellenger, H., E. Guilyardi, J. Leloup, M. Lengaigne, and J. Vialard (2014), ENSO representation in climate models: from CMIP3 to CMIP5, *Climate Dynamics*, *42*(7-8), 1999–2018, doi:10.1007/s00382-013-1783-z.

Berger, A. (1988), The peak at 3-7 days 3 . Extensive swampg (at the origin of coal the " Little Ice Age ," which began radiation, *Geophysique*, *26*(4), 624–657, doi:10.1029/RG026i004p00624.

Berger, A., and M. Loutre (1991), Insolation values for the climate of the last 10 million years, *Quaternary Science Reviews*, *10*(4), 297–317, doi:10.1016/0277-3791(91)90033-Q.

Bhatt, U. S., et al. (2010), Circumpolar Arctic Tundra Vegetation Change Is Linked to Sea Ice Decline, *Earth Interactions*, *14*(8), 1–20, doi:10.1175/2010EI315.1.

Bindoff, N. L., et al. (2007), Observations: oceanic climate change and sea level.

Bintanja, R., and R. S. W. van de Wal (2008), North American ice-sheet dynamics and the onset of 100,000-year glacial cycles, *Nature*, *454*(7206), 869–872, doi:10.1038/nature07158.

Bjerknes, J. (1969), Atmospheric Teleconnections From The Equatorial Pacific, *Monthly Weather Review*, *97*(3), 163–172, doi:10.1175/1520-0493(1969)097<0163:ATFTEP>2.3.CO;2.

Black, R. X. (1998), The Maintenance of Extratropical Intraseasonal Transient Eddy Activity in the GEOS-1 Assimilated Dataset, *Journal of the Atmospheric Sciences*, *55*(20), 3159–3175, doi:10.1175/1520-0469(1998)055<3159:TMOEIT>2.0.CO;2.

Bretagnon, P., and G. Francou (1988), Astronomy and astrophysics., *Astronomy and Astrophysics (ISSN 0004-6361), vol. 202, no. 1-2, Aug. 1988, p. 309-315.*, *202*, 309–315.

Brierley, C. M. (2015), Interannual climate variability seen in the Pliocene Model Intercomparison Project, *Clim. Past*, *11*, 605–618, doi:10.5194/cp-11-605-2015.

Brierley, C. M., and A. V. Fedorov (2016), Comparing the impacts of Miocene-Pliocene changes in inter-ocean gateways on climate: Central American Seaway, Bering Strait, and Indonesia, *Earth and Planetary Science Letters*, *444*, 116–130, doi:10.1016/j.epsl.2016.03.010.

Brierley, C. M., A. V. Fedorov, Z. Liu, T. D. Herbert, K. T. Lawrence, and J. P. LaRiviere (2009), Greatly expanded tropical warm pool and weakened hadley circulation in the early pliocene, *Science*, *323*(5922), 1714–1718.

Brigham-Grette, J., et al. (2013), Pliocene Warmth, Polar Amplification, and Stepped Pleistocene Cooling Recorded in NE Arctic Russia, *Science*, *340*(6139).

Broccoli, A. J., K. A. Dahl, and R. J. Stouffer (2006), Response of the ITCZ to Northern Hemisphere cooling, *Geophysical Research Letters*, *33*(1), n/a–n/a, doi:10.1029/2005GL024546.

Burls, N. J., and A. V. Fedorov (2014), Simulating Pliocene warmth and a permanent El Ni{ñ}o-like state: The role of cloud albedo, *Paleoceanography*, *29*(10), 893–910, doi:10.1002/2014PA002644.

Caballero, R., and M. Huber (2013), State-dependent climate sensitivity in past warm climates and its implications for future climate projections., *Proceedings of the National Academy of Sciences of the United States of America*, *110*(35), 14,162–7, doi:10.1073/pnas.1303365110.

Cai, M., X. Fang, F. Wu, Y. Miao, and E. Appel (2012), Pliocene–pleistocene stepwise drying of central asia: evidence from paleomagnetism and sporopollen record of the deep borehole sg-3 in the western qaidam basin, ne tibetan plateau, *Global and Planetary Change*, *94*, 72–81.

Cane, M. A. (1998), A Role for the Tropical Pacific, *Science*, *282*(5386).

Cane, M. A., and P. Molnar (2001), Closing of the Indonesian seaway as a precursor to east African aridification around 3 million years ago, *Nature*, *411*(6834), 157–162, doi:10.1038/35075500.

Chang, P., B. Wang, T. Li, and L. Ji (1994), Interactions between the seasonal cycle and the Southern Oscillation - Frequency entrainment and chaos in a coupled ocean-atmosphere model, *Geophysical Research Letters*, *21*(25), 2817–2820, doi:10.1029/94GL02759.

Chiang, J. C. H., and C. M. Bitz (2005), Influence of high latitude ice cover on the marine Intertropical Convergence Zone, *Climate Dynamics*, *25*(5), 477–496, doi:10.1007/s00382-005-0040-5.

Cobb, K. M., C. D. Charles, H. Cheng, and R. L. Edwards (2003), El Niño/Southern Oscillation and tropical Pacific climate during the last millennium, *Nature*, *424*(6946), 271–276, doi:10.1038/nature01779.

Collins, M., et al. (2010), The impact of global warming on the tropical Pacific Ocean and El Niño, *Nature Geoscience*, *3*(6), 391–397, doi:10.1038/ngeo868.

Davies, A., A. E. S. Kemp, G. P. Weedon, J. A. Barron, D. H., J. T., L. L., and R. G.J. (2012), El Nino-Southern Oscillation variability from the Late Cretaceous Marca Shale of California, *Geology*, *40*(1), 15–18, doi:10.1130/G32329.1.

Davini, P., J. von Hardenberg, L. Filippi, and A. Provenzale (2015), Impact of Greenland orography on the Atlantic Meridional Overturning Circulation, *Geophysical Research Letters*, *42*(3), 871–879, doi:10.1002/2014GL062668.

DeMenocal, P. B. (2004), African climate change and faunal evolution during the Pliocene-Pleistocene, *Earth and Planetary Science Letters*, *220*(1-2), 3–24, doi:10.1016/S0012-821X(04)00003-2.

Dethloff, K. (2004), The impact of Greenland's deglaciation on the Arctic circulation, *Geophysical Research Letters*, *31*(19), L19,201, doi:10.1029/2004GL020714.

DiNezio, P. N., et al. (2012), Mean Climate Controls on the Simulated Response of ENSO to Increasing Greenhouse Gases, *Journal of Climate*, *25*(21), 7399–7420, doi:10.1175/JCLI-D-11-00494.1.

Ding, Z., S. Yang, J. Sun, and T. Liu (2001), Iron geochemistry of loess and red clay deposits in the chinese loess plateau and implications for long-term asian monsoon evolution in the last 7.0 ma, *Earth and Planetary Science Letters*, *185*(1), 99–109.

Dolan, A. M., et al. (2015), Using results from the PlioMIP ensemble to investigate the Greenland Ice Sheet during the mid-Pliocene Warm Period, *Climate of the Past*, *11*(3), 403–424, doi:10.5194/cp-11-403-2015.

Dowsett, H. (2007), The prism palaeoclimate reconstruction and pliocene sea-surface temperature, *Deep-time perspectives on climate change: marrying the signal from computer models and biological proxies*, pp. 459–480.

Dowsett, H., and R. Poore (1991), Pliocene sea surface temperatures of the north atlantic ocean at 3.0 Ma, *Quaternary Science Reviews*, *10*(2-3), 189–204, doi:10.1016/0277-3791(91)90018-P.

Dowsett, H., et al. (2010), The PRISM3D paleoenvironmental reconstruction, *Stratigraphy*, *7*(2-3), 123–139.

Dowsett, H., et al. (2016), The PRISM4 (mid-Piacenzian) paleoenvironmental reconstruction, *Climate of the Past*, *12*(7), 1519–1538, doi:10.5194/cp-12-1519-2016.

Dowsett, H. J., and T. M. Cronin (1990), High eustatic sea level during the middle Pliocene:Evidence from the southeastern U.S. Atlantic Coastal Plain, *Geology*, *18*(5), 435, doi:10.1130/0091-7613(1990)018<0435:HESLDT>2.3.CO;2.

Dowsett, H. J., et al. (2012), Assessing confidence in Pliocene sea surface temperatures to evaluate predictive models, *Nature Climate Change*, *2*(5), 365–371, doi:10.1038/nclimate1455.

Duan, J., Z. Chen, and L. Wu (2017), Projected changes of the low-latitude north-western pacific wind-driven circulation under global warming, *Geophysical Research Letters*, *44*(10), 4976–4984, doi:10.1002/2017GL073355, 2017GL073355.

Dupont, L. M. (2006), Late Pliocene vegetation and climate in Namibia (southern Africa) derived from palynology of ODP Site 1082, *Geochemistry, Geophysics, Geosystems*, *7*(5), n/a–n/a, doi:10.1029/2005GC001208.

Dupont, L. M., B. Donner, L. Vidal, E. M. Pérez, and G. Wefer (2005), Linking desert evolution and coastal upwelling: Pliocene climate change in Namibia, *Geology*, *33*(6), 461–464, doi:10.1130/G21401.1.

Easterling, D. R., G. a. Meehl, C. Parmesan, S. a. Changnon, T. R. Karl, and L. O. Mearns (2000), Climate extremes: observations, modeling, and impacts., *Science (New York, N.Y.)*, *289*(5487), 2068–2074, doi:10.1126/science.289.5487.2068.

Farris, D. W., et al. (2011), Fracturing of the Panamanian Isthmus during initial collision with South America, *Geology*, *39*(11), 1007–1010, doi:10.1130/G32237.1.

Fedorov, A., P. Dekens, M. McCarthy, A. Ravelo, M. Barreiro, R. Pacanowski, S. Philander, et al. (2006), The pliocene paradox (mechanisms for a permanent el niño), *Science*, *312*(5779), 1485–1489.

Fedorov, A. V., C. M. Brierley, and K. Emanuel (2010), Tropical cyclones and permanent El Niño in the early Pliocene epoch, *Nature*, *463*(7284), 1066–1070, doi:10.1038/nature08831.

Fedorov, A. V., C. M. Brierley, K. T. Lawrence, Z. Liu, P. S. Dekens, and A. C. Ravelo (2013), Patterns and mechanisms of early Pliocene warmth, *Nature*, *496*(7443), 43–49, doi:10.1038/nature12003.

Folland, C. K., T. N. Palmer, and D. E. Parker (1986), Sahel rainfall and worldwide sea temperatures, 1901-85, *Nature*, *320*(6063), 602–607, doi:10.1038/320602a0.

Galeotti, S., A. von der Heydt, M. Huber, D. Bice, H. Dijkstra, T. Jilbert, L. Lanci, and G.-J. Reichart (2010), Evidence for active El Niño Southern Oscillation variability in the Late Miocene greenhouse climate, *Geology*, *38*(5).

Ge, J., et al. (2013), Major changes in East Asian climate in the mid-Pliocene: Triggered by the uplift of the Tibetan Plateau or global cooling?, *Journal of Asian Earth Sciences*, *69*, 48–59, doi:10.1016/j.jseaes.2012.10.009.

Graham, F. S., J. N. Brown, C. Langlais, S. J. Marsland, A. T. Wittenberg, and N. J. Holbrook (2014), Effectiveness of the Bjerknes stability index in representing ocean dynamics, *Climate Dynamics*, *43*(9-10), 2399–2414, doi:10.1007/s00382-014-2062-3.

Graversen, R. G., and M. Wang (2009), Polar amplification in a coupled climate model with locked albedo, *Climate Dynamics*, *33*(5), 629–643, doi:10.1007/s00382-009-0535-6.

Gregory, J. M., P. Huybrechts, and S. C. B. Raper (2004), Climatology: Threatened loss of the Greenland ice-sheet, *Nature*, *428*(6983), 616–616, doi:10.1038/428616a.

Haug, G. H., and R. Tiedemann (1998), Effect of the formation of the Isthmus of Panama on Atlantic Ocean thermohaline circulation, *Nature*, *393*(6686), 673–676, doi:10.1038/31447.

Haug, G. H., D. M. Sigman, R. Tiedemann, T. F. Pedersen, and M. Sarnthein (1999), Onset of permanent stratification in the subarctic Pacific Ocean, *Nature*, *401*(6755), 779–782, doi:10.1038/44550.

Haug, G. H., R. Tiedemann, R. Zahn, and A. C. Ravelo (2001), Role of Panama uplift on oceanic freshwater balance, *Geology*, *29*(3), 207, doi:10.1130/0091-7613(2001)029<0207:ROPUOO>2.0.CO;2.

Haywood, A. M., P. J. Valdes, and V. L. Peck (2007), A permanent El Niño-like state during the Pliocene?, *Paleoceanography*, *22*(1), n/a–n/a, doi:10.1029/2006PA001323.

Haywood, A. M., H. J. Dowsett, M. M. Robinson, D. K. Stoll, A. M. Dolan, D. J. Lunt, B. Otto-Bliesner, and M. A. Chandler (2011), Pliocene Model Intercomparison Project (PlioMIP): experimental design and boundary conditions (Experiment 2), *Geoscientific Model Development*, *4*(3), 571–577, doi:10.5194/gmd-4-571-2011.

Haywood, A. M., et al. (2013), On the identification of a Pliocene time slice for data-model comparison., *Philosophical transactions. Series A, Mathematical, physical, and engineering sciences*, *371*(2001), 20120,515, doi:10.1098/rsta.2012.0515.

Haywood, A. M., H. J. Dowsett, and A. M. Dolan (2016), Integrating geological archives and climate models for the mid-Pliocene warm period, *Nature Communications*, *7*(May 2015), 10,646, doi:10.1038/ncomms10646.

Herbert, T. D., L. C. Peterson, K. T. Lawrence, and Z. Liu (2010), Tropical Ocean Temperatures Over the Past 3.5 Million Years, *Science*, *328*(5985).

Hill, D. J. (2015), The non-analogue nature of Pliocene temperature gradients, *Earth and Planetary Science Letters*, *425*, 232–241, doi:10.1016/j.epsl.2015.05.044.

Hill, D. J., K. P. Bolton, and A. M. Haywood (2017), Modelled ocean changes at the plio-pleistocene transition driven by antarctic ice advance, *Nature Communications*, *8*, 14,376.

Howell, P. (2001), ARAND time series and spectral analysis package for the Macintosh, Brown University. IGBP PAGES/World Data Center for Paleoclimatology Data Contribution Series #2001-044. NOAA/NGDC Paleoclimatology Program, Boulder, Colorado, USA., *Tech. rep.*

Hu, Y., D. Li, and J. Liu (2007), Abrupt seasonal variation of the ITCZ and the Hadley circulation, *Geophysical Research Letters*, *34*(18), L18,814, doi:10.1029/2007GL030950.

Huang, P. (2015), Seasonal Changes in Tropical SST and the Surface Energy Budget under Global Warming Projected by CMIP5 Models, *Journal of Climate*, *28*(16), 6503–6515, doi: 10.1175/JCLI-D-15-0055.1.

Huang, P., S.-P. Xie, K. Hu, G. Huang, and R. Huang (2013), Patterns of the seasonal response of tropical rainfall to global warming, *Nature Geoscience*, *6*(5), 357–361, doi: 10.1038/ngeo1792.

Huber, M., and R. Caballero (2003), Eocene El Niño: Evidence for Robust Tropical Dynamics in the "Hothouse", *Science*, *299*(5608).

Huber, M., and R. Caballero (2011), The early Eocene equable climate problem revisited, *Clim. Past*, *7*, 603–633, doi:10.5194/cp-7-603-2011.

Huybers, P. (2011), Combined obliquity and precession pacing of late pleistocene deglaciations, *Nature*, *480*(7376), 229.

Imbrie, J., et al. (1992), On the Structure and Origin of Major Glaciation Cycles 1. Linear Responses to Milankovitch Forcing, *Paleoceanography*, *7*(6), 701–738, doi:10.1029/92PA02253.

Jiang, H., and Z. Ding (2008), A 20 ma pollen record of east-asian summer monsoon evolution from guyuan, ningxia, china, *Palaeogeography, Palaeoclimatology, Palaeoecology*, *265*(1), 30–38.

Jin, F.-F., J. Neelin, and M. Ghil (1996), El Niño/Southern Oscillation and the annual cycle: subharmonic frequency-locking and aperiodicity, *Physica D: Nonlinear Phenomena*, *98*(2-4), 442–465, doi:10.1016/0167-2789(96)00111-X.

Jin, F.-F., S. T. Kim, and L. Bejarano (2006), A coupled-stability index for ENSO, *Geophysical Research Letters*, *33*(23), L23,708, doi:10.1029/2006GL027221.

Jochum, M., B. Fox-Kemper, P. H. Molnar, and C. Shields (2009), Differences in the Indonesian seaway in a coupled climate model and their relevance to Pliocene climate and El Niño, *Paleoceanography*, *24*(1), n/a–n/a, doi:10.1029/2008PA001678.

Kang, S. M., R. Seager, D. M. W. Frierson, and X. Liu (2015), Croll revisited: Why is the northern hemisphere warmer than the southern hemisphere?, *Climate Dynamics*, *44*(5-6), 1457–1472, doi:10.1007/s00382-014-2147-z.

Karas, C., D. Nürnberg, A. K. Gupta, R. Tiedemann, K. Mohan, and T. Bickert (2009), Mid-Pliocene climate change amplified by a switch in Indonesian subsurface throughflow, *Nature Geoscience*, *2*(6), 434–438, doi:10.1038/ngeo520.

Karas, C., D. Nürnberg, A. Bahr, J. Groeneveld, J. O. Herrle, R. Tiedemann, and P. B. DeMenocal (2017), Pliocene oceanic seaways and global climate, *Scientific Reports*, *7*(November 2016), 39,842, doi:10.1038/srep39842.

Kim, S. T., and F.-F. Jin (2011a), An ENSO stability analysis. Part I: results from a hybrid coupled model, *Climate Dynamics*, *36*(7-8), 1593–1607, doi:10.1007/s00382-010-0796-0.

Kim, S. T., and F.-F. Jin (2011b), An ENSO stability analysis. Part II: results from the twentieth and twenty-first century simulations of the CMIP3 models, *Climate Dynamics*, *36*(7-8), 1609–1627, doi:10.1007/s00382-010-0872-5.

Knies, J., P. Cabedo-Sanz, S. T. Belt, S. Baranwal, S. Fietz, and A. Rosell-Melé (2014), The emergence of modern sea ice cover in the Arctic Ocean, *Nature communications*, *5*, 5608, doi:10.1038/ncomms6608.

Krebs, U., W. Park, and B. Schneider (2011), Pliocene aridification of Australia caused by tectonically induced weakening of the Indonesian throughflow, *Palaeogeography, Palaeoclimatology, Palaeoecology*, *309*(1-2), 111–117, doi:10.1016/j.palaeo.2011.06.002.

Kuhlbrodt, T., A. Griesel, M. Montoya, A. Levermann, M. Hofmann, and S. Rahmstorf (2007), On the driving processes of the Atlantic meridional overturning circulation, *Reviews of Geophysics*, *45*(2), doi:10.1029/2004RG000166.

Laskar, J., P. Robutel, F. Joutel, M. Gastineau, A. C. M. Correia, and B. Levrard (2004), A long-term numerical solution for the insolation quantities of the Earth, *Astronomy & Astrophysics*, *428*(1), 261–285, doi:10.1051/0004-6361:20041335.

Latif, M. (2001), Tropical Pacific/Atlantic Ocean interactions at multi-decadal time scales, *Geophysical Research Letters*, *28*(3), 539–542, doi:10.1029/2000GL011837.

Latif, M., and N. S. Keenlyside (2009), El niño/southern oscillation response to global warming, *Proceedings of the National Academy of Sciences*, *106*(49), 20,578–20,583.

Latif, M., E. Roeckner, U. Mikolajewicz, R. Voss, M. Latif, E. Roeckner, U. Mikolajewicz, and R. Voss (2000), Tropical stabilization of the thermohaline circulation in a greenhouse warming simulation, *Journal of Climate*, *13*(11), 1809–1813, doi:10.1175/1520-0442(2000)013<1809:L>2.0.CO;2.

Latif, M., et al. (2004), Reconstructing, Monitoring, and Predicting Multidecadal-Scale Changes in the North Atlantic Thermohaline Circulation with Sea Surface Temperature, *Journal of Climate*, *17*(7), 1605–1614, doi:10.1175/1520-0442(2004)017<1605:RMAPMC>2.0.CO;2.

Latif, M., V. A. Semenov, and W. Park (2015), Super El Niños in response to global warming in a climate model, *Climatic Change*, *132*(4), 489–500, doi:10.1007/s10584-015-1439-6.

Lawrence, K., S. Sosdian, H. White, and Y. Rosenthal (2010), North Atlantic climate evolution through the Plio-Pleistocene climate transitions, *Earth and Planetary Science Letters*, *300*(3-4), 329–342, doi:10.1016/j.epsl.2010.10.013.

Lawrence, K. T., T. D. Herbert, C. M. Brown, M. E. Raymo, and A. M. Haywood (2009), High-amplitude variations in north atlantic sea surface temperature during the early pliocene warm period, *Paleoceanography*, *24*(2), 1–15, doi:10.1029/2008PA001669.

Leduc, G., D. Garbe-Schönberg, M. Regenberg, C. Contoux, J. Etourneau, and R. Schneider (2014), The late Pliocene Benguela upwelling status revisited by means of multiple temperature proxies, *Geochemistry, Geophysics, Geosystems*, *15*(2), 475–491, doi:10.1002/2013GC004940.

Lélé, M. I., L. M. Leslie, P. J. Lamb, M. I. Lélé, L. M. Leslie, and P. J. Lamb (2015), Analysis of Low-Level Atmospheric Moisture Transport Associated with the West African Monsoon, *Journal of Climate*, *28*(11), 4414–4430, doi:10.1175/JCLI-D-14-00746.1.

Li, J., Z. Wu, Z. Jiang, and J. He (2010), Can global warming strengthen the East Asian summer monsoon?, *Journal of Climate*, *23*(24), 6696–6705, doi:10.1175/2010JCLI3434.1.

Li, T., S. G. H. Philander, T. Li, and S. G. H. Philander (1996), On the Annual Cycle of the Eastern Equatorial Pacific, doi:10.1175/1520-0442(1996)009<2986:OTACOT>2.0.CO;2.

Lisiecki, L. E. (2010), Links between eccentricity forcing and the 100,000-year glacial cycle, *Nature geoscience*, *3*(5), 349.

Lisiecki, L. E., and M. E. Raymo (2005), A Pliocene-Pleistocene stack of 57 globally distributed benthic δ^{18} O records, *Paleoceanography*, *20*(1), n/a–n/a, doi:10.1029/2004PA001071.

Lisiecki, L. E., and M. E. Raymo (2007), Plio-Pleistocene climate evolution: trends and transitions in glacial cycle dynamics, *Quaternary Science Reviews*, *26*(1-2), 56–69, doi: 10.1016/j.quascirev.2006.09.005.

Lisiecki, L. E., M. E. Raymo, and W. B. Curry (2008), Atlantic overturning responses to Late Pleistocene climate forcings, *Nature*, *456*(7218), 85–88, doi:10.1038/nature07425.

Liu, Z. (1996), Modeling Equatorial Annual Cycle with a Linear Coupled Model, *Journal of Climate*, *9*(10), 2376–2385, doi:10.1175/1520-0442(1996)009<2376:MEACWA>2.0.CO;2.

Liu, Z. (2002), A Simple Model Study of ENSO Suppression by External Periodic Forcing, *Journal of Climate*, *15*(9), 1088–1098, doi:10.1175/1520-0442(2002)015<1088:ASMSOE>2.0.CO;2.

Liu, Z., and S. Xie (1994), Equatorward Propagation of Coupled Air-Sea Disturbances with Application to the Annual Cycle of the Eastern Tropical Pacific, *Journal of the Atmospheric Sciences*, *51*(24), 3807–3822, doi:10.1175/1520-0469(1994)051<3807:EPOCAD>2.0.CO;2.

Lohmann, G. (2003), Atmospheric and oceanic freshwater transport during weak Atlantic overturning circulation, *Tellus A*, *55*(5), 438–449, doi:10.1034/j.1600-0870.2003.00028.x.

Lübbecke, J. F., M. J. McPhaden, J. F. Lübbecke, and M. J. McPhaden (2013), A Comparative Stability Analysis of Atlantic and Pacific Niño Modes, *Journal of Climate*, *26*(16), 5965–5980, doi:10.1175/JCLI-D-12-00758.1.

Lübbecke, J. F., M. J. McPhaden, J. F. Lübbecke, and M. J. McPhaden (2014), Assessing the Twenty-First-Century Shift in ENSO Variability in Terms of the Bjerknes Stability Index*, *Journal of Climate*, *27*(7), 2577–2587, doi:10.1175/JCLI-D-13-00438.1.

Lunt, D. J., G. L. Foster, A. M. Haywood, and E. J. Stone (2008), Late Pliocene Greenland glaciation controlled by a decline in atmospheric CO2 levels, *Nature*, *454*(7208), 1102–5, doi:10.1038/nature07223.

Ma, Y., F. Wu, X. Fang, J. Li, Z. An, and W. Wang (2005), Pollen record from red clay sequence in the central loess plateau between 8.10 and 2.60 ma, *Chinese Science Bulletin*, *50*(19), 2234–2243.

Madec, G. (2008), NEMO ocean engine: Notes du Pole de Mod{é}lisation 27, *Institut Pierre-Simon Laplace (IPSL), France*.

Maier-Reimer, E., U. Mikolajewicz, and T. Crowley (1990), Ocean General Circulation Model Sensitivity Experiment with an open Central American Isthmus, *Paleoceanography*, *5*(3), 349–366, doi:10.1029/PA005i003p00349.

Mantsis, D. F., A. C. Clement, A. J. Broccoli, and M. P. Erb (2011), Climate feedbacks in response to changes in obliquity, *Journal of Climate*, *24*(11), 2830–2845.

Mantsis, D. F., et al. (2014), The Response of Large-Scale Circulation to Obliquity-Induced Changes in Meridional Heating Gradients, *Journal of Climate*, *27*(14), 5504–5516, doi:10.1175/JCLI-D-13-00526.1.

Manucharyan, G. E., A. V. Fedorov, G. E. Manucharyan, and A. V. Fedorov (2014), Robust ENSO across a Wide Range of Climates, *Journal of Climate*, *27*(15), 5836–5850, doi:10.1175/JCLI-D-13-00759.1.

Martínez-Botí, M. A., G. L. Foster, T. B. Chalk, E. J. Rohling, P. F. Sexton, D. J. Lunt, R. D. Pancost, M. P. S. Badger, and D. N. Schmidt (2015), Plio-Pleistocene climate sensitivity evaluated using high-resolution CO2 records, *Nature*, *518*(7537), 49–54, doi:10.1038/nature14145.

Matsuno, T. (1966), Quasi-Geostrophic Motions in the Equatorial Area, *Journal of the Meteorological Society of Japan. Ser. II*, *44*(1), 25–43.

McGregor, S., A. Timmermann, M. H. England, O. Elison Timm, and A. T. Wittenberg (2013), Inferred changes in El Niño/Southern Oscillation variance over the past six centuries, *Climate of the Past*, *9*(5), 2269–2284, doi:10.5194/cp-9-2269-2013.

Mechoso, C., et al. (1995), The Seasonal Cycle over the Tropical Pacific in Coupled Ocean Atmosphere General Circulation Models, *Monthly Weather Review*, *123*(9), 2825–2838, doi:10.1175/1520-0493(1995)123<2825:TSCOTT>2.0.CO;2.

Mignot, J., and C. Frankignoul (2005), The variability of the Atlantic meridional overturning circulation, the North Atlantic Oscillation, and the El Ninõ-Southern Oscillation in the Bergen climate model, *Journal of climate*, *18*, 2361–2375, doi:10.1175/JCLI3405.1.

Mikolajewicz, U., M. Vizcaíno, J. Jungclaus, and G. Schurgers (2007), Effect of ice sheet interactions in anthropogenic climate change simulations, *Geophysical Research Letters*, *34*(18), L18,706, doi:10.1029/2007GL031173.

Molnar, P., and T. W. Cronin (2015), Growth of the Maritime Continent and its possible contribution to recurring Ice Ages, *Paleoceanography*, *30*(3), 196–225, doi:10.1002/2014PA002752.

Montes, C., et al. (2015), Middle Miocene closure of the Central American Seaway, *Science*, *348*(6231), 226–229, doi:10.1126/science.aaa2815.

Mudelsee, M., and M. E. Raymo (2005), Slow dynamics of the Northern Hemisphere glaciation, *Paleoceanography*, *20*(4), n/a–n/a, doi:10.1029/2005PA001153.

Naafs, B. D. A., R. Stein, J. Hefter, N. Khélifi, S. De Schepper, and G. H. Haug (2010), Late Pliocene changes in the North Atlantic Current, *Earth and Planetary Science Letters*, *298*(3), 434–442, doi:10.1016/j.epsl.2010.08.023.

Nie, J., T. Stevens, Y. Song, J. W. King, R. Zhang, S. Ji, L. Gong, and D. Cares (2014), Pacific freshening drives Pliocene cooling and Asian monsoon intensification, *Sci Rep*, *4*, 5474, doi:10.1038/srep05474.

Otto-Bliesner, B. L., et al. (2017), Amplified North Atlantic warming in the late Pliocene by changes in Arctic gateways, *Geophysical Research Letters*, *44*(2), 957–964, doi:10.1002/2016GL071805.

Pagani, M., Z. Liu, J. LaRiviere, and A. C. Ravelo (2010), High Earth-system climate sensitivity determined from Pliocene carbon dioxide concentrations, *Nature Geoscience*, *3*(1), 27–30, doi:10.1038/ngeo724.

Park, T., W. Park, and M. Latif (2016), Correcting north atlantic sea surface salinity biases in the kiel climate model: influences on ocean circulation and atlantic multidecadal variability, *Climate dynamics*, *47*(7-8), 2543–2560, doi:10.1007/s00382-016-2982-1.

Park, W., and M. Latif (2012), Atlantic Meridional Overturning Circulation response to idealized external forcing, *Climate Dynamics*, *39*(7-8), 1709–1726, doi:10.1007/s00382-011-1212-0.

Park, W., et al. (2009), Tropical Pacific Climate and Its Response to Global Warming in the Kiel Climate Model, *Journal of Climate*, *22*(1), 71–92, doi:10.1175/2008JCLI2261.1.

Peterson, L. C., G. H. Haug, K. A. Hughen, and U. Röhl (2000), Rapid Changes in the Hydrologic Cycle of the Tropical Atlantic During the Last Glacial, *Science*, *290*(5498).

Philander, S. G., and A. V. Fedorov (2003), Role of tropics in changing the response to Milankovich forcing some three million years ago, *Paleoceanography*, *18*(2), doi:10.1029/2002PA000837.

Pierrehumbert, R. T. (2000), Climate change and the tropical Pacific: the sleeping dragon wakes., *Proceedings of the National Academy of Sciences of the United States of America*, *97*(4), 1355–8.

Ravelo, A. C., D. H. Andreasen, M. Lyle, A. Olivarez Lyle, and M. W. Wara (2004), Regional climate shifts caused by gradual global cooling in the Pliocene epoch, *Nature*, *429*(6989), 263–267, doi:10.1038/nature02567.

Raymo, M. E., and M. Horowitz (1996), Organic carbon paleo-pCO2 and marine-ice core correlations and chronology, *Geophysical Research Letters*, *23*(4), 367–370, doi:10.1029/96GL00254.

Rind, D., and M. Chandler (1991), Increased ocean heat transports and warmer climate, *Journal of Geophysical Research*, *96*(D4), 7437, doi:10.1029/91JD00009.

Roeckner, E., et al. (2003), The atmospheric general circulation model ECHAM 5. PART I: Model description.

Roeckner, E., G. Bäuml, and I. Kirchner (2006), The atmospheric general circulation model ECHAM 5.

Rohling, E. J., G. L. Foster, K. M. Grant, G. Marino, A. P. Roberts, M. E. Tamisiea, and F. Williams (2014), Sea-level and deep-sea-temperature variability over the past 5.3 million years, *Nature*, *508*(7497), 477, doi:10.1038/nature13230.

Schmittner, A., C. Appenzeller, and T. F. Stocker (2000), Enhanced Atlantic freshwater export during El Niño, *Geophysical Research Letters*, *27*(8), 1163–1166, doi:10.1029/1999GL011048.

Schneider, B., G. Leduc, and W. Park (2010), Disentangling seasonal signals in holocene climate trends by satellite-model-proxy integration, *Paleoceanography*, *25*(4).

Scroxton, N., S. G. Bonham, R. E. M. Rickaby, S. H. F. Lawrence, M. Hermoso, and A. M. Haywood (2011), Persistent El Niño-Southern Oscillation variation during the Pliocene Epoch, *Paleoceanography*, *26*(2), n/a–n/a, doi:10.1029/2010PA002097.

Seki, O., G. L. Foster, D. N. Schmidt, A. Mackensen, K. Kawamura, and R. D. Pancost (2010), Alkenone and boron-based Pliocene pCO2 records, *Earth and Planetary Science Letters*, *292*(1), 201–211, doi:10.1016/j.epsl.2010.01.037.

Semenov, V. A., W. Park, and M. Latif (2009), Barents Sea inflow shutdown: A new mechanism for rapid climate changes, *Geophysical Research Letters*, *36*(14), L14,709, doi:10.1029/2009GL038911.

Steph, S., R. Tiedemann, J. Groeneveld, A. Sturm, and D. Nürnberg (2006), Pliocene Changes in Tropical East Pacific Upper Ocean Stratification: Response to Tropical Gateways?, in *Proceedings of the Ocean Drilling Program, 202 Scientific Results*, Ocean Drilling Program, doi:10.2973/odp.proc.sr.202.211.2006.

Steph, S., et al. (2010), Early Pliocene increase in thermohaline overturning: A precondition for the development of the modern equatorial Pacific cold tongue, *Paleoceanography*, *25*(2), 1–17, doi:10.1029/2008PA001645.

Stewart, D. R., P. N. Pearson, P. W. Ditchfield, and J. M. Singano (2004), Miocene tropical indian ocean temperatures: evidence from three exceptionally preserved foraminiferal assemblages from tanzania, *Journal of African Earth Sciences*, *40*(3), 173–189.

Stocker, T. F., et al. (2013), Climate Change 2013 The Physical Science Basis Working Group I Contribution to the Fifth Assessment Report of the Intergovernmental Panel on Climate Change.

Taylor, K. E., R. J. Stouffer, G. A. Meehl, K. E. Taylor, R. J. Stouffer, and G. A. Meehl (2012), An Overview of CMIP5 and the Experiment Design, *Bulletin of the American Meteorological Society*, *93*(4), 485–498, doi:10.1175/BAMS-D-11-00094.1.

Timmermann, A., F.-F. Jin, and M. Collins (2004), Intensification of the annual cycle in the tropical Pacific due to greenhouse warming, *Geophysical Research Letters*, *31*(12), n/a–n/a, doi:10.1029/2004GL019442.

Timmermann, A., et al. (2007), The Influence of a Weakening of the Atlantic Meridional Overturning Circulation on ENSO, *Journal of Climate*, *20*(19), 4899–4919, doi:10.1175/JCLI4283.1.

Tripati, A. K., C. D. Roberts, and R. A. Eagle (2009), Coupling of CO2 and Ice Sheet Stability Over Major Climate Transitions of the Last 20 Million Years, *Science*, *326*(5958), 1394–1397, doi:10.1126/science.1178296.

Unger, N., and X. Yue (2014), Strong chemistry-climate feedbacks in the Pliocene, *Geophysical Research Letters*, *41*(2), 527–533, doi:10.1002/2013GL058773.

Valcke, S. (2006), PRISM An Infrastructure Project for Climate Research in Europe OASIS3 User Guide prism 2-5.

Valdes, P. (2011), Built for stability, *Nature Publishing Group*, *4*, doi:10.1038/ngeo1200.

Vecchi, G. A., B. J. Soden, G. A. Vecchi, and B. J. Soden (2007), Global Warming and the Weakening of the Tropical Circulation, *Journal of Climate*, *20*(17), 4316–4340, doi:10.1175/JCLI4258.1.

Vellinga, M., P. Wu, M. Vellinga, and P. Wu (2004), Low-Latitude Freshwater Influence on Centennial Variability of the Atlantic Thermohaline Circulation, *Journal of Climate*, *17*(23), 4498–4511, doi:10.1175/3219.1.

Viebahn, J. P., A. S. von der Heydt, D. Le Bars, and H. A. Dijkstra (2016), Effects of Drake Passage on a strongly eddying global ocean, *Paleoceanography*, *31*(5), 564–581, doi:10.1002/2015PA002888.

Wan, S., A. Li, P. D. Clift, and J.-B. W. Stuut (2007), Development of the east asian monsoon: mineralogical and sedimentologic records in the northern south china sea since 20 ma, *Palaeogeography, Palaeoclimatology, Palaeoecology*, *254*(3), 561–582.

Wang, L., H. Y. Lü, N. Q. Wu, J. Li, Y. P. Pei, G. B. Tong, and S. Z. Peng (2006), Palynological evidence for Late Miocene-Pliocene vegetation evolution recorded in the red clay sequence of the central Chinese Loess Plateau and implication for palaeoenvironmental change, *Palaeogeography, Palaeoclimatology, Palaeoecology*, *241*(1), 118–128, doi:10.1016/j.palaeo.2006.06.012.

Wang, Y.-L., C.-R. Wu, and S.-Y. Chao (2016), Warming and weakening trends of the kuroshio during 1993–2013, *Geophysical Research Letters*, *43*(17), 9200–9207.

Wara, M. W., A. C. Ravelo, and M. L. Delaney (2005), Permanent El Niño-like Conditions during the Pliocene Warm Period, *Source: Science, New Series*, *309*(5735), 758–761, doi:10.1126/science.1112596.

Watanabe, T., et al. (2011), Permanent el niño during the pliocene warm period not supported by coral evidence, *Nature*, *471*(7337), 209.

Wu, F., X. Fang, Y. Ma, M. Herrmann, V. Mosbrugger, Z. An, and Y. Miao (2007), Plio–quaternary stepwise drying of asia: Evidence from a 3-ma pollen record from the chinese loess plateau, *Earth and Planetary Science Letters*, *257*(1), 160–169.

Wu, F., X. Fang, M. Herrmann, V. Mosbrugger, and Y. Miao (2011), Extended drought in the interior of central asia since the pliocene reconstructed from sporopollen records, *Global and Planetary Change*, *76*(1), 16–21.

Xie, S.-P. (1994), On the Genesis of the Equatorial Annual Cycle, *Journal of Climate*, *7*(12), 2008–2013, doi:10.1175/1520-0442(1994)007<2008:OTGOTE>2.0.CO;2.

Xie, S.-P. (1996), Westward Propagation of Latitudinal Asymmetry in a Coupled Ocean-Atmosphere Model, *Journal of the Atmospheric Sciences*, *53*(22), 3236–3250, doi:10.1175/1520-0469(1996)053<3236:WPOLAI>2.0.CO;2.

Xie, S.-P., A. Kubokawa, and K. Hanawa (1989), Oscillations with Two Feedback Processes in a Coupled Ocean-Atmosphere Model, *Journal of Climate*, *2*(9), 946–964, doi:10.1175/1520-0442(1989)002<0946:OWTFPI>2.0.CO;2.

Yang, S., K. M. Lau, and K. M. Kim (2002), Variations of the East Asian jet stream and Asian-Pacific-American winter climate anomalies, *Journal of Climate*, *15*(1), 306–325, doi:10.1175/1520-0442(2002)015<0306:VOTEAJ>2.0.CO;2.

Yu, B., and F. W. Zwiers (2010), Changes in equatorial atmospheric zonal circulations in recent decades, *Geophysical Research Letters*, *37*(5), 1–5, doi:10.1029/2009GL042071.

Zachos, J., M. Pagani, L. Sloan, E. Thomas, and K. Billups (2001), Trends, rhythms, and aberrations in global climate 65 Ma to present, *Science*, *292*(5517).

Zebiak, S. E., and M. A. Cane (1987), A Model El Niño/Southern Oscillation, *Monthly Weather Review*, *115*(10), 2262–2278, doi:10.1175/1520-0493(1987)115<2262:AMENO>2.0.CO;2.

Zhang, R., T. L. Delworth, R. Zhang, and T. L. Delworth (2005), Simulated Tropical Response to a Substantial Weakening of the Atlantic Thermohaline Circulation, *Journal of Climate*, *18*(12), 1853–1860, doi:10.1175/JCLI3460.1.

Zhang, R., D. B. Jiang, X. D. Liu, and Z. P. Tian (2012a), Modeling the climate effects of different subregional uplifts within the Himalaya-Tibetan Plateau on Asian summer monsoon evolution, *Chinese Science Bulletin*, *57*(35), 4617–4626, doi:10.1007/s11434-012-5284-y.

Zhang, R., et al. (2013a), Mid-Pliocene East Asian monsoon climate simulated in the PlioMIP, *Climate of the Past*, *9*(5), 2085–2099, doi:10.5194/cp-9-2085-2013.

Zhang, X., et al. (2012b), Changes in equatorial Pacific thermocline depth in response to Panamanian seaway closure: Insights from a multi-model study, *Earth and Planetary Science Letters*, *317*, 76–84, doi:10.1016/j.epsl.2011.11.028.

Zhang, Y. G., et al. (2009), Mid-Pliocene Asian monsoon intensification and the onset of Northern Hemisphere glaciation, *Geology*, *37*(7), 599–602, doi:10.1130/G25670A.1.

Zhang, Z.-S. S., et al. (2013b), Mid-pliocene Atlantic Meridional Overturning Circulation not unlike modern, *Climate of the Past*, *9*(4), 1495–1504, doi:10.5194/cp-9-1495-2013.

Zubakov, and Borzenkova (1988), Pliocene paleoclimates past climates as possible analogues of mid twenty first century climate, *Palaeogeography Palaeoclimatology Palaeoecology*, *65*(1-2), 35–50.

Acknowledgments

First all of all, I would like to express my sincere appreciation to my supervisor, Prof. Dr. Mojib Latif, for his excellent academic support and guidance for my Ph.D. study. Over the years, I continuously received inspiring ideas and important suggestions from him. He showed me how important the critical thinking is in science, but also how to evaluate arguments and evidence, and how to present the scientific results into more logical and understandable ways. He is always easy-going, caring, patient and hilarious. And I shall always be grateful to him for approving me a three-month stay at home so I could accompany my mother in the final days of her life.

My sincere gratitude also goes to Dr. Wonsun Park for his extensive help on both science and life. He has been offering me support on programing skills, ideas and suggestions on research, revisions of manuscripts, and encouragement in my early days in Kiel and ever since. He has been passing on his academic and living experiences to me, and even listening to me in my hard times. I could not have accomplished this work without his help.

I also want to thank all the colleagues in the ME division. Special thanks to Dr. Guidi Zhou and Dr. Yanling Wu for their kindness and support, Dr. Tobias Bayr for the discussions and revisions on this thesis, Dr. Fritz Krueger and Dr. Annika Reintges for their help on work.

I also appreciate the financial support from the China Scholarship Council (CSC), and the Integrated School of Ocean Sciences (ISOS) at the Excellence Cluster "The Future Ocean" at Kiel University for the support during my PhD studies.

Last but not least, none of this would have been possible without the love, patience and support from my family. My mother had always believed in me and supported me until the end of her life. My beloved wife, Yuming, has always been there for me and encouraging me. Her love and caring helped me through the time of darkness, loneliness and depression. I also appreciate my parents-in-law for helping taking care of my daughter.

Declaration

I hereby declare that this work is my own work apart from my supervisors' guidance and acknowledged assistance. This thesis has not been submitted for the award of doctoral degree in any other examining body and was prepared according to the Rules of Good Scientific Practice of the German Research Foundation.

Kiel, Oct. 2017

(Zhaoyang Song)